

Probing electronic structures of graphene under magnetic field and electric field by Raman spectroscopy

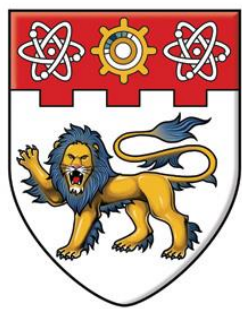
Shen, Xiaonan

2014

Shen, X. (2014). Probing electronic structures of graphene under magnetic field and electric field by Raman spectroscopy. Doctoral thesis, Nanyang Technological University, Singapore.

<https://hdl.handle.net/10356/62257>

<https://doi.org/10.32657/10356/62257>



NANYANG
TECHNOLOGICAL
UNIVERSITY

**PROBING ELECTRONIC STRUCTURES OF
GRAPHENE UNDER MAGNETIC FIELD AND
ELECTRIC FIELD BY RAMAN SPECTROSCOPY**

SHEN XIAONAN

SCHOOL OF PHYSICAL AND MATHEMATICAL SCIENCES

2014

**PROBING ELECTRONIC STRUCTURES OF
GRAPHENE UNDER MAGNETIC FIELD AND
ELECTRIC FIELD BY RAMAN SPECTROSCOPY**

SHEN XIAONAN

School of Physical and Mathematical Sciences

A thesis submitted to the Nanyang Technological University
in fulfillment of the requirement for the degree of
Doctor of Philosophy

2014

Acknowledgement

First of all, I would like to express my sincere gratitude to my supervisor, Nanyang Associate Professor Ting YU, for his unfailing guidance and support throughout my PhD study at Nanyang Technological University. His patience and rich knowledge motivate my enthusiasm and enrich my fundamental research abilities in the research field. His advisements to help on critical thinking and to solve problems smartly will be always remembered. Communication skills for effective discussion or collaboration with other researchers can be learned and improved with his insightful suggestions. Without his firm support, I cannot go through all kinds of experiments and fulfil those works present in this thesis.

I am appreciated that Professor Zexiang Shen shares his research facilities in the Raman Lab. I also give thanks to Nanyang Associate Professor Qihua Xiong for his support on the thermal evaporation and wire bonding.

I would like to give my warmest gratitude to all our group members: Dr. Haomin Wang, Dr. Cunxiao Cong, Dr. Caiyu Qiu, Dr. Jingzhi Shang, Dr. Mustafa Eginligil, Dr. Hailong Hu, Mr. Bingchen Cao, Ms. Namphung Peimyoo and Mr. Yanlong Wang *et al.* Their suggestions and fruitful discussions contribute to my improvement on both the experimental techniques and background knowledge.

Finally, I am so grateful to my family for their continuous encouragements and supports.

Table of content

Acknowledgement.....	I
Table of content	II
Summary	V
Publications	VIII
Nomenclature	X
Acronyms.....	XII
Citations to published works	XIV
Chapter 1 Introduction	1
1.1 Introduction to graphene	1
1.2 Electronic band structure of graphene	2
1.3 Raman spectrum of graphene.....	5
1.4 Disorders in graphene	8
1.5 Phonons in graphene tuned by electric field	10
1.6 Phonons in graphene under magnetic field	11
1.7 Recent studies on magneto-Raman scattering in graphene.....	13
1.8 Motivation and organization of the thesis	14
Chapter 2 Experimental techniques	17
2.1 Introduction.....	17
2.2 Mechanical exfoliation of graphene onto SiO ₂ /Si substrate.....	17

2.3 Raman spectroscopy	18
2.4 Fabrication of graphene based devices	19
2.5 Transport measurements.....	21
2.6 Magneto-Raman system	22
Chapter 3 Electron beam writing and metal deposition effects on graphene	25
3.1 Introduction and motivation.....	25
3.2 Experimental results.....	27
3.2.1 Experimental details	27
3.2.2 Lattice properties of graphene after e-beam irradiation.....	28
3.2.3 Metal deposition effects on electronic structures of graphene	36
3.3 Conclusions.....	44
Chapter 4 Magneto-Raman scattering of monolayer graphene on graphite	46
4.1 Introduction.....	46
4.2 Experimental results.....	50
4.2.1 Experimental details	50
4.2.2 High quality sample and triple splitting of G mode	52
4.2.3 Assignment of Raman active LL transitions under magnetic field	55
4.2.4 Two coupled mode fitting for the MPR	60
4.2.5 Two coupled mode fitting with magnetic field dependent LL width	68
4.2.6 Summary of rich Raman features of graphene under magnetic field	71

4.2.7 Magnetic field dependent behaviour of G_i mode	73
4.2.8 Newly proposed model for G_i mode behaviour	75
4.2.9 Simulation results based on the proposed model	78
4.2.10 Surface morphology of the graphene on graphite characterized by AFM....	82
4.3 Conclusions.....	84
Chapter 5 Electrical field tuning of magneto-phonon resonance in monolayer graphene	86
5.1 Introduction and motivation.....	86
5.2 Experimental results.....	88
5.2.1 Experimental details	88
5.2.2 Tunable doping levels in graphene transistor under electrical field	89
5.2.3 Fano Resonance in graphene under magnetic field and electric field	92
5.2.4 Tunable Raman G mode under magnetic field and electric field.....	95
5.2.5 Discussions for observed experimental results	96
5.2.6 MPR in as prepared supported and suspended graphene.....	100
5.3 Conclusions.....	105
Chapter 6 Conclusions and future work	106
6.1 Conclusions.....	106
6.2 Future work.....	108
References:	111

Summary

This thesis presents research in frontiers of Raman spectroscopy: the magneto-Raman scattering of monolayer graphene on graphite and electrical field tuning of magneto-phonon resonance (MPR) in graphene transistor.

Part 1. Understanding the electron beam (e--beam) irradiation and metal deposition effects on the lattice of graphene would be helpful for our research work on MPR in graphene transistor. Electron beam writing and metal evaporation are common techniques to fabricate graphene device. No clear consensus about the influence of electron beam irradiation on graphene has been reached yet and metal deposition effect on the lattice of graphene would be something new and interesting. We have carried out a detailed Raman study on the influence of medium energy electron irradiation on monolayer graphene. Raman D band can still be observed in monolayer graphene after lithography process because most of the accelerated electrons can penetrate the resist and interact with the graphene and substrate. We have investigated the effects of metallic contact deposition, such as the widely adopted titanium and gold on the lattice structure of graphene through Raman measurements. These findings could be valuable for further development of processes in the fabrication of graphene-based devices.

Part 2. Previously, the experimental observation of MPR had very different degrees of success in samples with different qualities, and many theoretical issues

remain unsettled. High quality monolayer graphene has been identified on the surface of graphite substrate and it shows a clear MPR which is induced by an intense mixing of the G phonon and the Dirac fermion magnetoexcitons. In the most pronounced MPR region at $\sim 4.65\text{T}$, three sub-modes (G_+ , G_- and G_i modes) of the G band are observed. These three special modes are attributed to: (i) the coupling between the G phonon and the magneto-optical transitions, which is responsible for G_+ and G_- and can be well described by the two coupled mode model and (ii) the magnetic field dependent oscillation of the G_i band is newly explained by the G band of graphite modified by the interaction with G_+ and G_- . Comparing to previous reports, we give a thorough experimental and theoretical discussion of MPR in graphene on graphite sample. Our experimental and theoretical findings must be helpful for the research communities to investigate new fundamental properties of graphene and other two-dimensional (2D) systems.

Part 3. The doping level or filling factor of graphene is expected to drastically affect the MPR behavior. To date, only a few related experimental works have been reported and more investigations on this subject are needed. We have conducted magneto-Raman measurements by sweeping relatively low magnetic fields in mechanically exfoliated monolayer graphene under different situations: (1) fabricated as field effect device and electrically tuned to fixed doping levels; (2) supported on SiO_2/Si substrate; (3) suspended. We have found that the MPR effect involving $LL_{-2,1}^{-1,2}$ transitions appears when the filling factor is near zero while it disappears when the sample is highly doped due to Pauli blocking. Suspended monolayer

graphene sample shows the clearest MPR oscillation among our studied samples, indicating the importance of sample quality. This work offers a way to study the MPR of materials through magneto-Raman with external electrical field.

Publications

1. **Shen, X.***; Qiu, C.*; Cao, B.; Cong, C.; Wang, H.; Yang, W.; Yu, T. Electrical Field Tuning of Magneto-Raman Scattering in Monolayer Graphene. Accepted for publication in **Nano Research** (DOI 10.1007/s12274-014-0594-9).
2. Qiu, C.* , **Shen, X.***, Cao, B., Cong, C., Saito, R., Yu, J., Dresselhaus, M. S., Yu, T. Strong magnetophonon resonance induced triple G-mode splitting in graphene on graphite probed by micromagneto Raman spectroscopy. **Phys. Rev. B** **2013**, **88**, 165407. (*These author contribute equally to this work)
3. **Shen, X.**, Wang, H., Yu, T. How do the electron beam writing and metal deposition affect the properties of graphene during device fabrication? **Nanoscale** **2013**, **5**, 3352-3358.
4. Shang, J., **Shen, X.**, Cong, C., Peimyoo, N., Cao, B., Eginligil, M., Yu, T. Observation of Excitonic Fine Structure in a 2D Transition-Metal Dichalcogenide Semiconductor. Accepted for publication in **ACS Nano** (DOI: 10.1021/nn5059908).
5. Cao, B.; **Shen, X.**; Shang, J.; Cong, C.; Yang, W.; Eginligil, M.; Yu, T. Low temperature photoresponse of monolayer tungsten disulphide. **APL Materials** **2014**, **2**, 116101
6. Peimyoo, N.; Yang, W.; Shang, J.; **Shen, X.**; Wang, Y.; Yu, T. Chemically Driven Tunable Light Emission of Charged and Neutral Excitons in Monolayer WS₂. **ACS Nano** **2014**, **8**, 11320-11329.
7. Jiang, J.; Zhu, J.; Ai, W.; Fan, Z.; **Shen, X.**; Zou, C.; Liu, J.; Zhang, H.; Yu, T. Evolution of disposable bamboo chopsticks into uniform carbon fibers: a smart strategy to fabricate sustainable anodes for Li-ion batteries. **Energy Environ. Sci.** **2014**, **7**, 2670-2679.

8. Zhengji, X., Tao, L., Dao-Hua, Z., Changchun, Y., Dongdong, L., Landobasa, Y. M. T., Fei, Q., Yueke, W., **Shen, X.**, Yu, T. Groove-structured metasurfaces for modulation of surface plasmon propagation. **Applied Physics Express** **2014**, **7**, **052001**.
9. Peimyoo, N., Shang, J., Cong, C., **Shen, X.**, Wu, X., Yeow, E. K. L., Yu, T. Nonblinking, Intense Two-Dimensional Light Emitter: Monolayer WS₂ Triangles. **ACS Nano** **2013**, **7**, **10985-10994**.
10. Zhou, H., Yu, F., Liu, Y., Zou, X., Cong, C., Qiu, C., Yu, T., Yan, Z., **Shen, X.**, Sun, L., Yakobson, B., Tour, J. Thickness-dependent patterning of MoS₂ sheets with well-oriented triangular pits by heating in air. **Nano Res.** **2013**, **6**, **703-711**.
11. Wang, J., Qin, F., Zhang, D. H., Li, D., Wang, Y., **Shen, X.**, Yu, T., Teng, J. Subwavelength superfocusing with a dipole-wave-reciprocal binary zone plate. **Appl. Phys. Lett.** **2013**, **102**, **061103-061104**.
12. Peimyoo, N.; Li, J.; Shang, J.; **Shen, X.**; Qiu, C.; Xie, L.; Huang, W.; Yu, T. Photocontrolled Molecular Structural Transition and Doping in Graphene. **ACS Nano** **2012**, **6**, **8878-8886**.

Nomenclature

B	magnetic field
C	capacitance per unit area
e	electron charge
E_F	Fermi energy
g	coupling strength
I	current
k	wavevector
L	length
l	mean free path
l_B	magnetic length
n	carrier density of electron
R	resistance
T	temperature
V	voltage
V_g	gate voltage
W	width
a	lattice constant
λ	wavelength
\hbar	Plank constant
γ	broadening parameter
t	hopping energy between neighbour atoms

τ	lifetime
ν	filling factor
v_F	Fermi velocity
ω	phonon energy
μ	carrier mobility
φ	work function

Acronyms

AC	alternating current
AFM	atomic force microscope
BLG	bilayer graphene
BWF	Breit-Wigner-Fano
BZ	Brillion zone
CCD	charge coupled device
CVD	chemical vapour deposition
DR	double resonance
EBL	electron beam lithography
FET	field effect transistor
FWHM	full width at half maximum
HOPG	highly oriented pyrolytic graphite
IPA	isopropyl alcohol
IQHE	integer quantum Hall effect
LL	Landau levels
MIBK	methyl isobutyl ketone
MPR	magneto phonon resonance
NP	neutral point
OM	optical microscope
PMMA	polymethylmethacrylate
RH	relative humidity
RPM	round per minute
SEM	scanning electron microscopy

SLG	single layer graphene
STS	scanning tunnelling spectroscopy
TEM	transmission electron microscopy
TLG	trilayer graphene
2D	two dimensional

Citations to published works

Majority of Chapter 3 appears as:

“**Shen, X.**; Wang, H.; Yu, T. How do the electron beam writing and metal deposition affect the properties of graphene during device fabrication? **Nanoscale** 2013, 5, 3352-3358.”

Majority of Chapter 4 appears as:

“Qiu, C.*; **Shen, X.***; Cao, B.; Cong, C.; Saito, R.; Yu, J.; Dresselhaus, M. S.; Yu, T. Strong magnetophonon resonance induced triple G-mode splitting in graphene on graphite probed by micromagneto Raman spectroscopy. **Phys. Rev. B** 2013, 88, 165407.”

Majority of Chapter 5 appears as:

“**Shen, X.***; Qiu, C.*; Cao, B.; Cong, C.; Wang, H.; Yang, W.; Yu, T. Electrical Field Tuning of Magneto-Raman Scattering in Monolayer Graphene.” Accepted for publication in **Nano Research** (DOI 10.1007/s12274-014-0594-9).

Chapter 1 Introduction

1.1 Introduction to graphene

Graphene is a two-dimensional material which is made of hexagonally arranged carbon atoms. It attracts much interest due to its fundamental physical properties and potential applications [1].

Graphene is found to be a semimetal material which has a zero band-gap between its conduction band and valence band around the six corners of the hexagonal Brillouin zone due to its unique crystal structure. Graphene shows many new fundamental properties like half-integer quantum hall effect, room temperature quantum hall effect and ballistic transport based on its special electronic structure [2-4]. There are still many interesting physical phenomena to be studied in graphene as it provides the two-dimensional playground. Graphene is also a wonderful material that possesses many excellent properties like good thermal conductivity, strong intrinsic strength and high transparency [5-7]. Potential applications for graphene are expected based on these properties. Pioneer works gave tries to make graphene into transparent electrodes, single molecule detector and high frequency transistors in recent years [8-12]. New applications of graphene are popular topics in the research field.

The Nobel Prize of Physics in 2010 was awarded to Professor Andre Geim and Professor Konstantin Novoselov for their ground-breaking study on graphene. The

award could be seen to acknowledge the promise of graphene to revolutionize the electronics industry and the potential applications based on its outstanding properties like light weight and strong intrinsic strength.

1.2 Electronic band structure of graphene

The electronic band structure of graphene could be derived from its crystal structure. Graphene is made up by hexagonal arranged carbon atoms as shown in Figure 1.1a. Each unit cell contains two carbon atoms. The lattice unit vectors can be written as:

$$\mathbf{a}_1 = \frac{a}{2}(3\hat{x} + \sqrt{3}\hat{y}), \quad \mathbf{a}_2 = \frac{a}{2}(3\hat{x} - \sqrt{3}\hat{y}) \quad (1.1)$$

Here, the nearest distance between carbon-carbon atoms is $a \approx 1.42 \text{ \AA}$.

The reciprocal lattice of the graphene is shown in Figure 1.1b and the unit vectors can be known as:

$$\mathbf{b}_1 = \frac{2\pi}{3a}(\hat{k}_x + \sqrt{3}\hat{k}_y), \quad \mathbf{b}_2 = \frac{2\pi}{3a}(\hat{k}_x - \sqrt{3}\hat{k}_y) \quad (1.2)$$

Highly symmetric points of the first Brillion zone (BZ) are also shown in Figure 1.1b. Γ point is the zone centre. K and K' points, which are not equivalent, are at the corners of the BZ. M point locates in the middle of K and K' points.

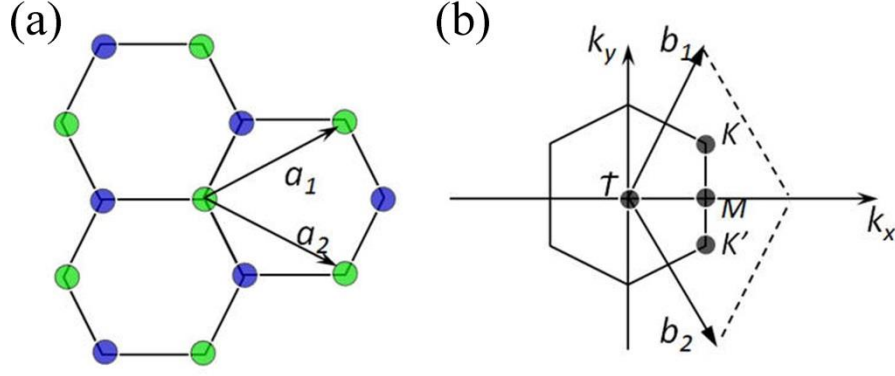


Figure 1.1 (a) Lattice structure of graphene. (a_1 and a_2 are the lattice unit vectors) (b) The reciprocal lattice of graphene (corresponding first Brillion zone). K and K' are Dirac points. Γ and M are another two high symmetry points (b_1 and b_2 are reciprocal lattice unit vectors).

Each carbon atom contains six electrons on its electron orbitals. Two of the electrons are on the 1s orbital and the other four are on 2s, 2p orbitals. Every carbon atom in graphene is connected to three nearest ones to form the bonds. The 2s, 2p_x, 2p_y orbitals hybridize to form the sp² hybrid orbitals (σ and σ^* bonds) when forming bonds. The 2p_z orbital forms π and π^* orbitals. Four valence electrons only occupy σ and π bands in electrical neutral graphene.

The electronic band structure of graphene can be theoretically calculated by tight-binding method. Considering that the electrons in graphene are able to hop from one carbon atom to the nearest and the next nearest ones, the Hamiltonian can be written as [13]:

$$H = -t \sum_{\langle i,j \rangle, \sigma} (a_{\sigma,i}^\dagger b_{\sigma,j} + \text{H.c.}) - t' \sum_{\langle\langle i,j \rangle\rangle, \sigma} (a_{\sigma,i}^\dagger a_{\sigma,j} + b_{\sigma,i}^\dagger b_{\sigma,j} + \text{H.c.}) \quad (1.3)$$

Here, t is the nearest-neighbour hopping energy and t' is the next nearest-neighbour hopping energy.

Derived from tight-binding method, the energy bands have the form [13]:

$$E_{\pm}(k) = \pm t \sqrt{3 + f(k)} - t'(k),$$

$$f(k) = 2 \cos(\sqrt{3}k_y a) + 4 \cos\left(\frac{\sqrt{3}}{2}k_y a\right) \cos\left(\frac{3}{2}k_x a\right) \quad (1.4)$$

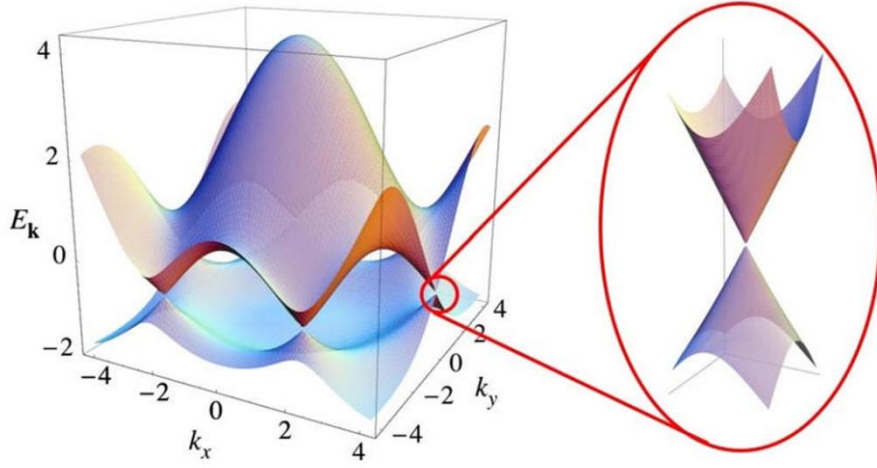


Figure 1.2 Band structure of graphene calculated by tight-binding approach using hopping energy $t=2.7\text{eV}$ and $t'=0.2t$. Right side shows the zoom in image of band dispersion around one of the Dirac points. (Adapted from Ref. [13]).

The calculated electronic band structure of graphene is shown in Figure 1.2. The electronic band structures around K and K' points show linear dispersion. It's experimentally demonstrated that the electrons and holes around the six corners of the BZ behave as massless Dirac fermions [14]. Thus, the K and K' points are also named as Dirac points.

1.3 Raman spectrum of graphene

Raman scattering is an inelastic scattering process of the incident laser light. It is first reported by India scientist Raman, who was awarded the Nobel Prize in Physics for his discovery in 1930.

Raman spectroscopy is proved to be a useful technique in graphene research field to study its physical properties. For example, Raman study can be used to determine the thickness of graphene layers [15, 16], to investigate the interaction of phonons and electrons [17, 18], and to detect defects in graphene [19-21].

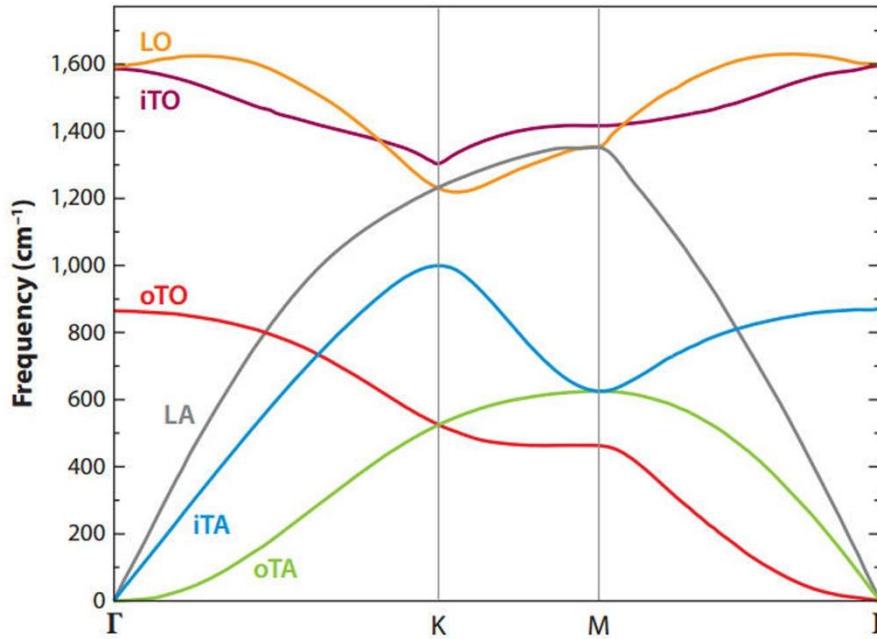


Figure 1.3 Phonon dispersion relationships in graphene. There are six phonon modes (LO, iTO, oTO, LA, iTA and oTA modes) in graphene. (Adapted from Ref. [22]).

Phonon dispersion curve in graphene is basic and essential to understand the Raman spectroscopy of graphene [21]. Based on the honeycomb crystal structure,

where the unit cell contains two carbon atoms, graphene has six phonon modes. Three of the modes are acoustic modes while the other three are optical modes. In-plane and out-of-plane phonon modes are classified by the vibration direction parallel or perpendicular to the crystal plane of graphene. Longitudinal or transverse phonon modes are distinguished by the vibration direction (parallel or perpendicular to the carbon-carbon direction). Therefore, the six modes (see Figure 1.3) can be assigned as LO, iTO, oTO, LA, iTA, oTA phonon modes [22].

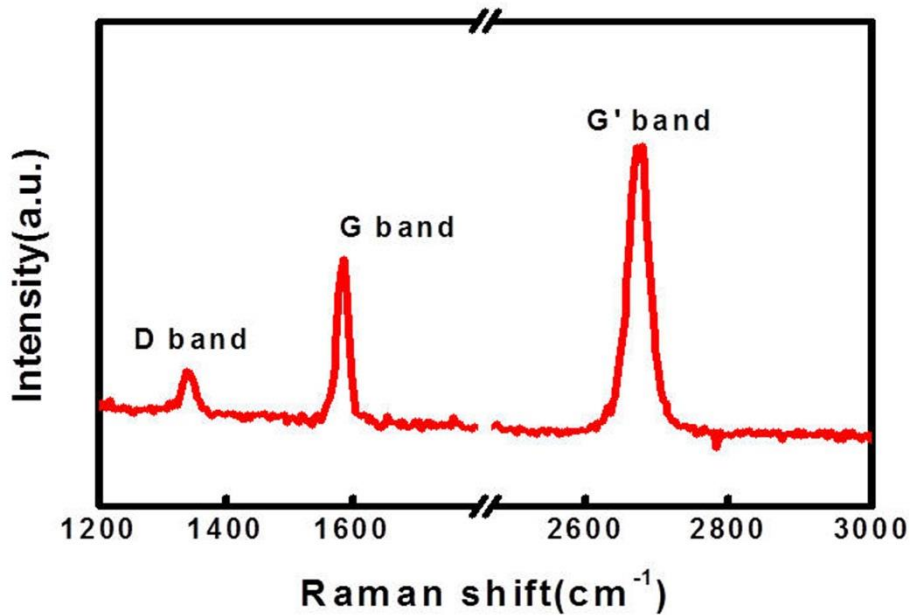


Figure 1.4 Typical Raman spectrum of monolayer graphene which shows obvious D band, excited by 2.33eV laser.

Raman spectrum of mechanically exfoliated monolayer graphene on SiO₂/Si substrate is shown in Figure 1.4 [23, 24]. Two fingerprint bands of graphene are G band which locates around 1580 cm⁻¹ and G' band locates around 2675 cm⁻¹. The

excitation energy for the used laser is 2.33 eV. D band, locating around 1340 cm^{-1} , will appear due to defects in graphene crystal structure [21].

The Raman scattering processes of G, D, and G' bands are shown in Figure 1.5. The G band is associated with the degenerated (iTO and LO) phonon modes around Γ point in the first Brillouin zone [21]. G band is a first order Raman scattering process which means only one phonon was involved in the scattering process. On the other hand, both D and G' band are second order Raman scattering process [15, 25]. As shown in Figure 1.5, scattering process of G' band starts from the electron around K point with wavevector k which absorbs a photon from the laser. Then, the excited electron is scattered to a position which is at K' point of the lattice structure by a phonon (with wavevector q). Later, the electron is scattered back and recombines with the hole at k state. This scattering process is called double resonance (DR) process because two real electronic states are involved. D band scattering process is also a DR process, in which one scattering process is due to defect while the other one is due to phonon [25].

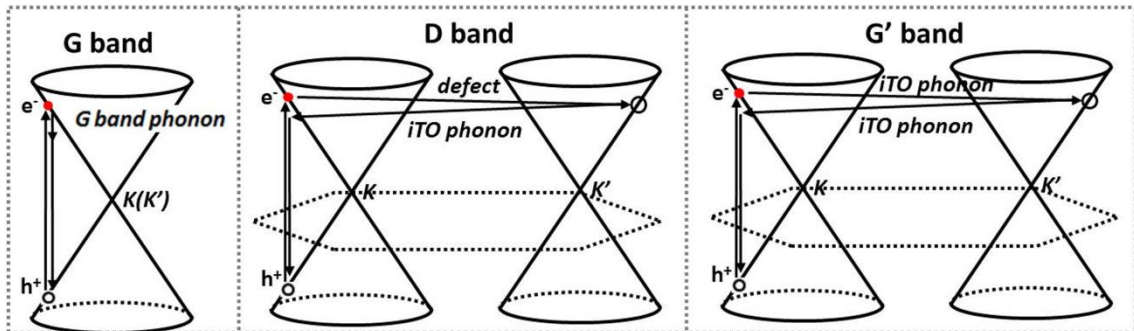


Figure 1.5 Schematics for Raman scattering processes of G, D and G' bands in monolayer graphene. (Adapted from Ref. [21]).

1.4 Disorders in graphene

It is important to understand the defect effects in graphene because those defects affect the sample quality and will affect the performances of graphene. Quality of the graphene sample limits its use in both research study and device applications.

Energetic bombardments onto the lattice of graphene can generate defect like vacancies [26]. Electron beam and hydrogen plasma are reported to be able to induce defects in graphene [27, 28]. Raman D peak in graphene is sensitive to the existence of defects in the lattice, thus, Raman spectrum can characterize the qualities of graphene samples. As can be seen in Figure 1.6b, the Raman D peak can be observed when the graphene device is exposed to hydrogen plasma. Intensity of Raman D peak increases when the exposure time increases. However, conductance of the graphene device decreases when the exposure time increases. It means that the defect scattering in the graphene device affects the mobility of the carriers in the sample. Interestingly, it is found that the intervalley scattering which is responsible for the D peak can set a limit on the mobility in graphene [28]. Thus, it is possible to estimate the mobility of graphene based on the Raman spectrum when the intervalley scattering dominates the transport properties of graphene.

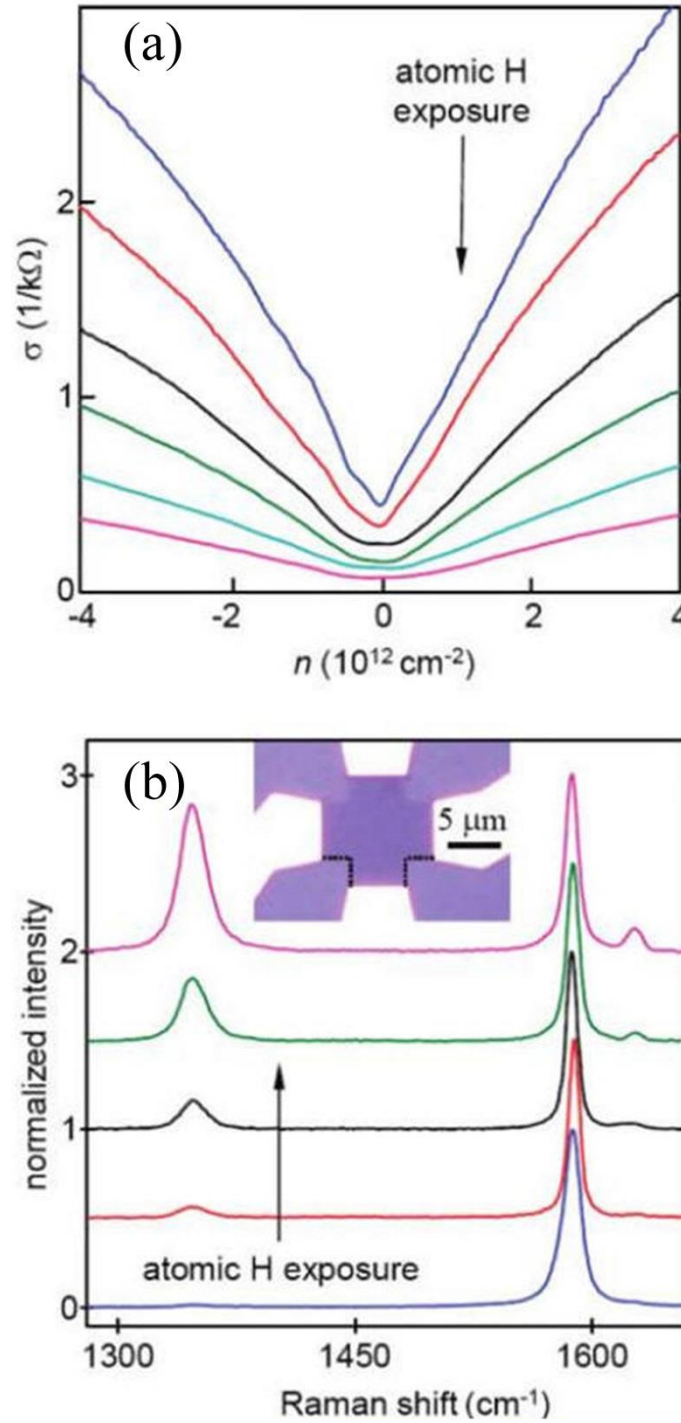


Figure 1.6 (a) Conductance curves of graphene device under various hydrogen exposures. (b) Raman spectrum of graphene device under different amounts of hydrogen exposure. Curve in the same colour means the same hydrogen exposure. Inset is the optical image of the graphene device. (Adapted from Ref. [28]).

1.5 Phonons in graphene tuned by electric field

Typically, doping can affect the properties of samples by changing the electron phonon coupling in the sample. The charge neutral point in graphene is commonly at positive back gate voltages indicating the p -type doping of the sample when in atmosphere. This p -type doping can be reduced when the sample is put into a high vacuum environment.

Interestingly, the doping effect tuned by electric field in graphene can be monitored by Raman spectroscopy. This enables Raman spectroscopy to investigate the doping situation in graphene. The electrical tunable electron-phonon coupling effect in graphene has been experimentally demonstrated [17, 18]. As shown in Figure 1.7a, G band width changes with Fermi energy. The G band width shows a maximum at the charge neutral point due to the large phonon decay. When the sample is highly doped, the high Fermi level blocks the decaying of phonon into electron-hole pair. Similarly, the energy of the G phonon shows a minimum at charge neutral point. The energy of G phonon decreases when the interaction of the phonon and electron hole pairs increase. When the doping level is high enough (Figure 1.7f), the interaction between phonon and electron hole pairs will be blocked. Ion gel which has a large capacitance is demonstrated to be a proper material to tune the electron-phonon coupling in graphene. Trends of G band width and frequency as a function of doping level were found to be similar as the back gate method through this top gate method [17]. Thus, the charge neutral point of one graphene sample can be monitored by Raman spectra.

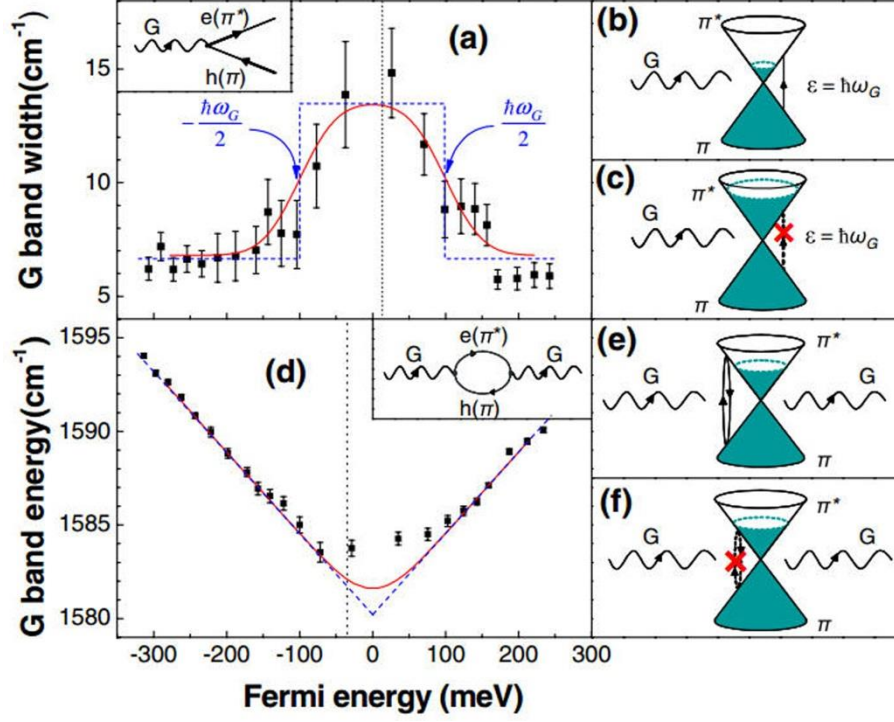


Figure 1.7 G band width and energy as a function of Fermi level of the graphene shown in (a) and (d), insets are Feynman diagrams for the electron phonon coupling. (b) broadening of G phonon due to decay into electron hole pairs (c) decay of G phonon forbidden due to high Fermi level of the graphene. (e) G phonon energy renormalization (forbidden) due to interaction with electron hole pairs. (f) G phonon energy renormalization forbidden due to high Fermi level of the graphene. (Adapted from Ref. [18]).

1.6 Phonons in graphene under magnetic field

Landau levels (LLs) will appear when the graphene is under a magnetic field which is perpendicular to its lattice plane. Magneto-phonon resonance is an effect which

occurs when the phonon energy of the material equals to the separation between Landau levels. The physical nature of this MPR can be understood that the possibility of phonon-electron interaction will sharply increase when MPR occurs [29]. Thus, the energy and lifetime of the specific phonon could be dramatically affected when MPR happens. MPR was predicted and experimentally observed in early 1960s by Firsov *et al.* [29]. Many experiments were carried out on MPR effect of semiconductors since its discovery [30-32].

Phonons in graphene would be affected through MPR effect. MPR in graphene is theoretically predicted to occur when the LL transition energy equals to G band phonon energy [33, 34]. Electronic excitation is often used to describe the transition between LLs [35]. According to the selection rule, only electronic excitations $(n+1)^- \rightarrow n$ or $n^- \rightarrow n+1$ can have strong MPR because that these excitations have the same symmetry as that of the G band phonon (E_2 symmetry) [33-35]. Coupled modes should be observed and would have anti-crossing dispersion [34]. As shown in Figure 1.8b, without MPR, the G phonon energy is stable and indicated by the horizontal dashed line. The LL transitions can be Raman active and their energy evolves with magnetic field. Without MPR, the energies of LL transitions as a function of magnetic field are shown in dashed line which crosses the horizontal dashed line. However, due to the MPR, the coupled Raman modes will show anti-crossing behaviour as indicated by the solid lines.

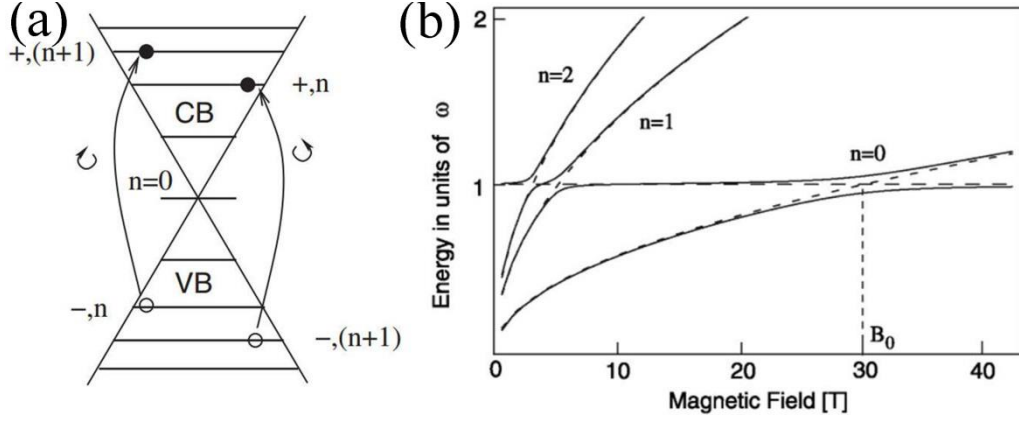


Figure 1.8 (a) Inter-band electronic transitions which can couple to G band phonon have two different circular polarizations. (b) Calculated coupled modes dispersion of G band phonon and electronic excitations with the evolution of magnetic field. Energy(ω) is in units of the G band phonon energy. (Adapted from Ref. [34]).

1.7 Recent studies on magneto-Raman scattering in graphene

MPR in both epitaxial grown graphene and graphene on graphite surface have been experimentally observed recently [36, 37]. MPR effect was experimentally observed on epitaxial grown multilayer graphene on SiC substrate by Faugeras *et al.* in the year 2009 [36]. Then more obvious anti-crossing dispersion of the two coupled modes of G band phonon and electronic excitation was observed by Yan jun *et al.* [37]. It was suspected that only some selected areas on graphite have pronounced MPR effect [37]. Furthermore, subsequent experimental results support that these selected areas are special areas which are called graphene on graphite (decoupled monolayer graphene on the graphite surface, also found by scanning tunnelling microscope) [38-40].

Notably, electronic excitations (Figure 1.9a) which are Raman active can be clearly observed [35, 38, 39, 41]. Polarized Raman has been used to explore the origin of these Raman active electronic excitations (Figure 1.9b) [38, 39]. Typical bulk graphite which does not have graphene on its surface is also measured by Raman spectroscopy in high magnetic field [39, 41].

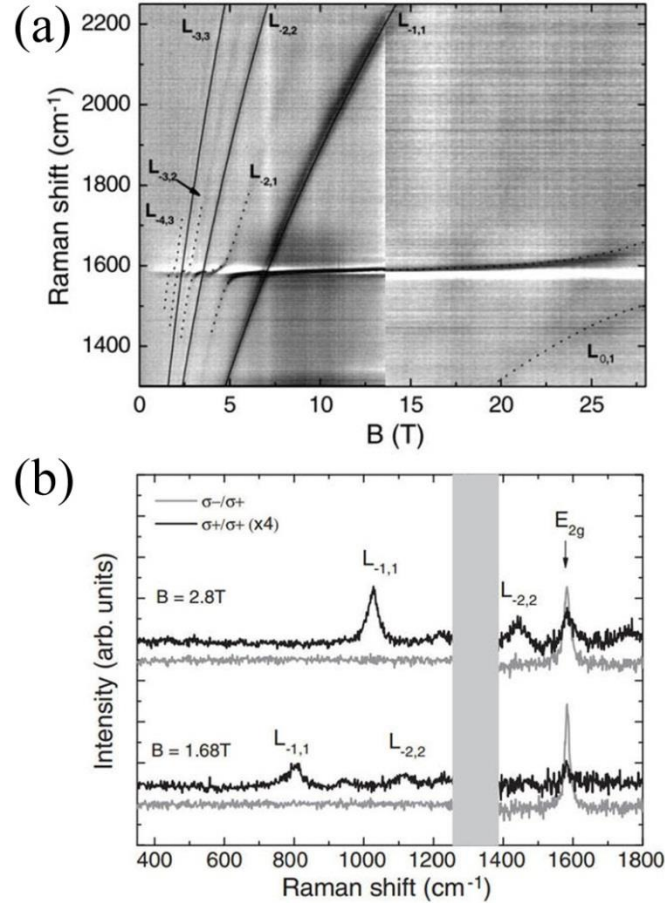


Figure 1.9 (a) Raman shift intensity of the graphene on graphite as a function of magnetic field. (b) Polarized Raman to examine the Raman active electronic excitations. (Adapted from Ref. [38]).

1.8 Motivation and organization of the thesis

Though magneto-phonon resonance in graphene has been demonstrated, unsettled questions need more detailed experimental results for deeper understandings of this

phenomenon. Knowledge about the electron beam irradiation and metal deposition effects on graphene during device fabrication are helpful for our study on MPR in graphene transistor, however, very few works reported on this topic and it needs further investigation. Raman spectroscopy and electronic transport measurements are powerful techniques to investigate the electronic structures of graphene. A custom designed magneto-Raman system which is also capable to probe the in-situ transport properties of the graphene has been developed to study magneto-Raman scattering in graphene related system. Therefore, this thesis focuses on the electronic structure of graphene under magnetic field and electric field probed by Raman spectroscopy.

The thesis is organized as follows:

Chapter 1 introduces the basic electron-phonon interaction in graphene and reviews the current status on magneto-phonon resonance in graphene.

Chapter 2 shows the experimental techniques to prepare the graphene device and the custom designed magneto-Raman system.

Chapter 3 mainly studies the electron beam irradiation and metal deposition effects on graphene during device fabrication.

Chapter 4 focuses on the magneto-phonon resonance in “graphene on graphite”. Mechanism for the triple splitting of the G mode is discussed. G_i mode behaviour is interpreted with a newly proposed model.

Chapter 5 reports the magneto-Raman scattering in monolayer graphene transistor.

Electrical field tuning is experimentally demonstrated to switch on/off the magneto-phonon coupling.

Chapter 6 includes the summary for these works from chapter 3 to chapter 5 and proposes future works based on the results presented in this thesis.

Chapter 2 Experimental techniques

2.1 Introduction

First of all, graphene samples are prepared by mechanical exfoliation method. Optical microscope and Raman spectroscopy can be utilized to examine the thickness of graphene based samples. Electron beam lithography and evaporation techniques can be adopted for graphene based device fabrication. Transport measurements characterize the electrical properties of samples. A custom designed Magneto-Raman system can measure Raman spectroscopy of samples at low temperature with a high magnetic field.

2.2 Mechanical exfoliation of graphene onto SiO₂/Si substrate.

Mechanical exfoliation and chemical vapour deposition (CVD) are widely used methods for researchers to prepare graphene samples [1, 9]. Exfoliated graphene samples are relatively used more often for fundamental physics study because they often show better properties compared to CVD grown samples. CVD grown samples have grain boundaries which are common to be observed [42].

Due to the weak interaction forces between layers of bulk graphite, it is possible to get a monolayer graphene by mechanical exfoliation method. Typical monolayer graphene sample is peeled off onto a SiO₂/Si substrate (see Figure 2.1). Optical contrast is a quick way to roughly identify the thickness of graphene [16]. Thickness

of the oxide plays a role to make the graphene visible. According to the calculation based on Fresnel theory, thickness values of oxide at 90 nm and 280 nm are most proper for the visibility of graphene on SiO_2/Si substrate under white light [43].

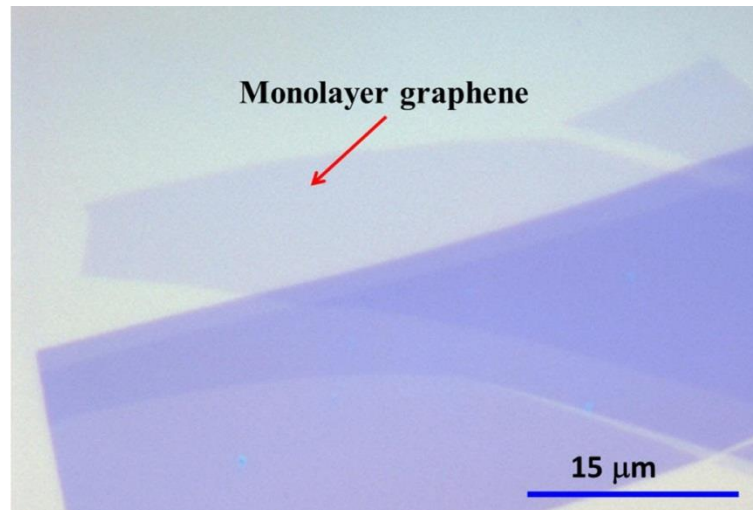


Figure 2.1: Optical image of one exfoliated sample which contains monolayer and multilayer graphene. Monolayer graphene region is indicated by the red arrow.

2.3 Raman spectroscopy

Raman scattering is an inelastic scattering process of light. Inelastic scattering process means that the incident light and scattered light have an energy difference. The Raman shift is commonly used to express the energy difference. Raman shifts observed by the Raman spectroscopy technique reflect the phonon modes of materials. It can be a technique for the identification of materials because the existence of their special Raman peaks. Currently, commercial Raman system often contains components like laser sources, charge-coupled device (CCD) detector, and

spectrometers and so on. The final laser spot hits onto the samples can be about 1 μm [16].

Raman spectroscopy is a powerful technique to examine the thickness of graphene-based samples. It is a convenient and non-destructive way to confirm the monolayer graphene sample. G' peak in the Raman spectroscopy of monolayer graphene can be fitted into only one Lorentz peak [15]. And the value of the G' peak width is typically about 30 cm^{-1} for monolayer graphene. Shapes of the G' peak of multilayer graphene will be different from that of the monolayer.

2.4 Fabrication of graphene based devices

Monolayer graphene based field effect transistor (FET) is fabricated for research study in this thesis. The purpose for us to fabricate the device is to tune the doping levels of graphene by an electrical gate. With a simple two electrode configuration device, we can characterize the electrical properties of the devices. Conductivity and mobility of the sample can be extracted from the transport measurements. Here, processes to fabricate the graphene-based devices would be introduced.

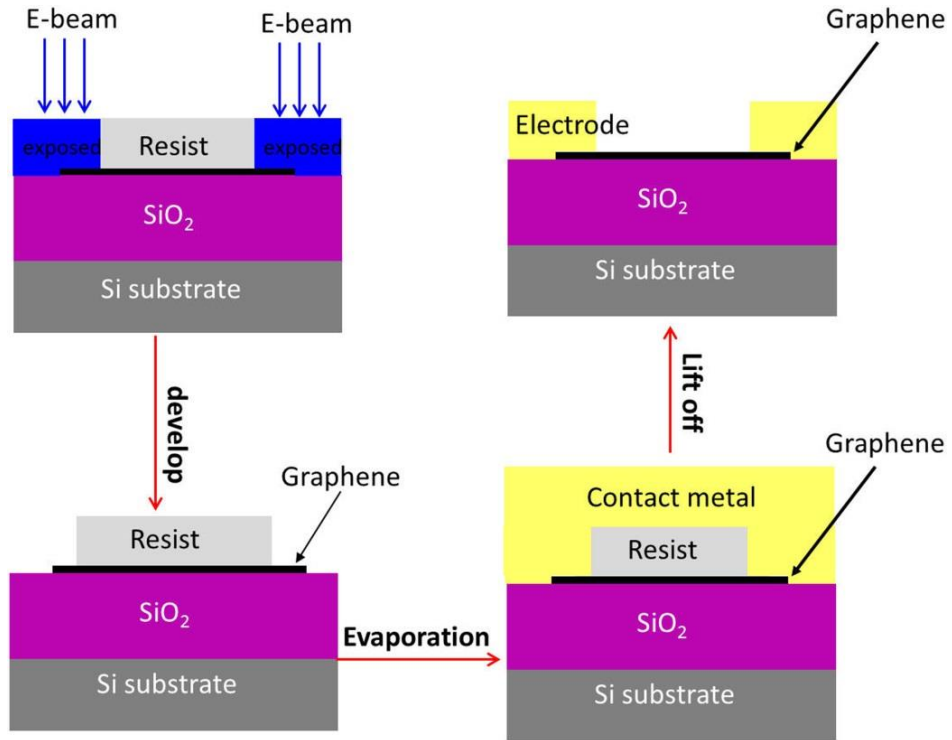


Figure 2.2: Schematic for the processes to fabricate graphene based devices.

First of all, resist is spin-coated onto the graphene sample. Polymethylmethacrylate (PMMA, Micro Chem) is used as the resist and the spin speed for coating is 4000 round per minute (RPM). Sample with resist is then baked on the hotplate for 1 minute at 180 centigrade degrees. Electron beam lithography (EBL) is followed to expose certain region of the resist [23]. Electron beam lithography is a maskless lithography technique which normally can have high resolution. The size of the exposed region can be as narrow as 1 μm . The resist in exposed region is soluble in a particular solvent. This process to remove the exposed resist is named “develop”. Solution used for develop is methyl isobutyl ketone: isopropyl alcohol (MIBK: IPA) solution with a volume ratio at 1:3. Optical image of graphene after develop process can be found in Figure 2.3b. After develop, contact metals like Ti and Au are

evaporated onto the sample. Typical thicknesses of contact metals can be 5 nm for Ti and 60 nm for gold. After deposition, the sample with metals can be immersed into acetone solution. This step is named “lift off”. The residual resist with metals mounted can be taken away after “lift off”. As illustrated in Figure 2.2, a graphene field effect transistor can be ready for measurements after “lift off” process.

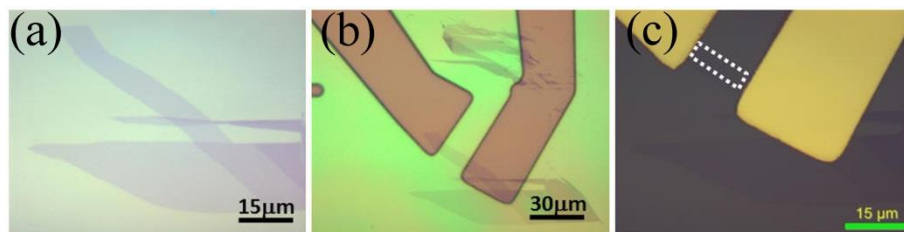


Figure 2.3 Optical images of the pristine graphene sample (a), with resist after develop (b), graphene device (c). Dashed dots in (c) indicate the region contains graphene between electrodes.

2.5 Transport measurements

A semiconductor characterization system (from Keithley, model 4200-SCS) provides us the ability for the transport measurements. Electrodes of graphene based FET transistor can be connected to the electrical meter by a probe station (see Figure 2.4a). For the graphene based devices, we can extract the conductivity, resistivity and carrier mobility of the sample through electrical characterization.

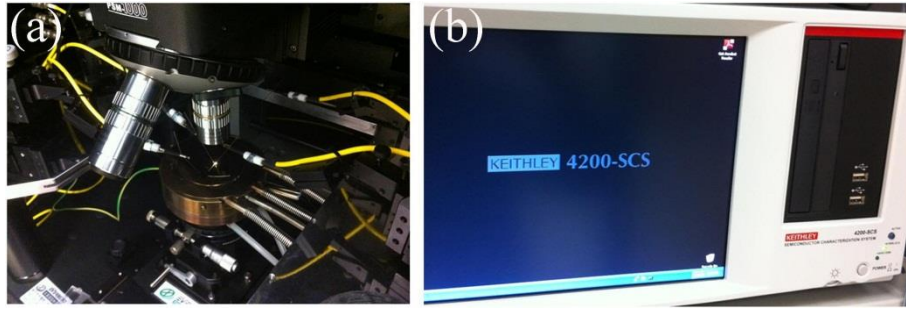


Figure 2.4 Optical pictures of the four-probe station (a) and Keithley 4200-SCS parameter analyzer (b).

2.6 Magneto-Raman system

A custom designed Magneto-Raman system is developed to study the interaction between Landau level transitions and phonons in graphene [44].

The main components of conventional Raman system are: excitation laser source, sample illumination and collection system, wavelength selector, detection and computer system. Based on commercial Witec confocal Raman system, our customdesigned system also includes a cryostat which can generate magnetic field up to 9 T. A schematic image of the system is shown in Figure 2.5. It is worth to mention that efforts would be spent during every experiment since the relative long optical path for the laser should be optimized.

Solid-state laser source (Nd:YAG, 532 nm wavelength) provides a maximum power of about 30 mW. Excitation and collection for the sample are accomplished by back scattering geometries. Sample stage which is made of non-magnetic materials consists of fine scan piezo actuator and coarse scan positioners. Grating

monochromator is applied as the wavelength selector. Thermoelectrically cooled CCD is used for signal collection. After optimizing the optical path for the excitation laser in the system, laser spot size which illuminates sample can be as small as around 1 μm . Superconductor magnet which can generate a magnetic field perpendicular to the sample is mounted inside the cryostat. Low temperature at about 4.2 K can be fulfilled by the liquid helium bath in the cryostat.

Electrical measurement can also be carried out with this system when the sample is connected to the Keithley parameter analyzer.

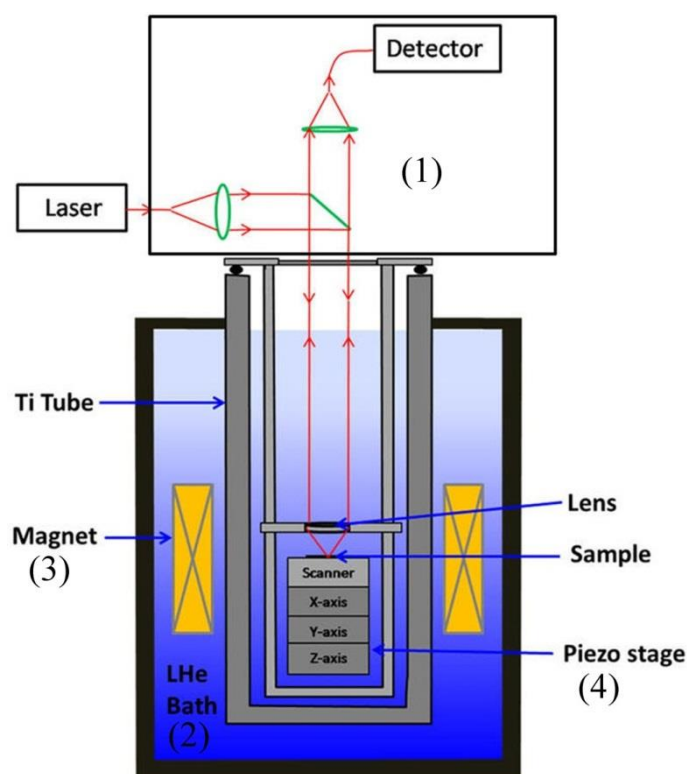


Figure 2.5 Schematic view of the magneto-Raman system. The system mainly contains four parts: (1) the Raman system; (2) the cryostat; (3) the superconducting magnet

can generate a magnetic field which is perpendicular to the graphene lattice; and (4) the piezo stage.

Characterization works for the system were also carried out. Commercial calibration grating sample (Anfatec-UMG02) was used to test our system. Scanning electron microscopy (SEM) image of the calibration sample is shown in Figure 2.6a. The chess pattern structure makes it suitable for the lateral calibration. Confocal Rayleigh mapping images at room temperature and low temperature are shown in Figure 2.6b and Figure 2.6c, respectively. From these test results, it is concluded that the spatial resolution can reach about $1\text{ }\mu\text{m}$ for the system.

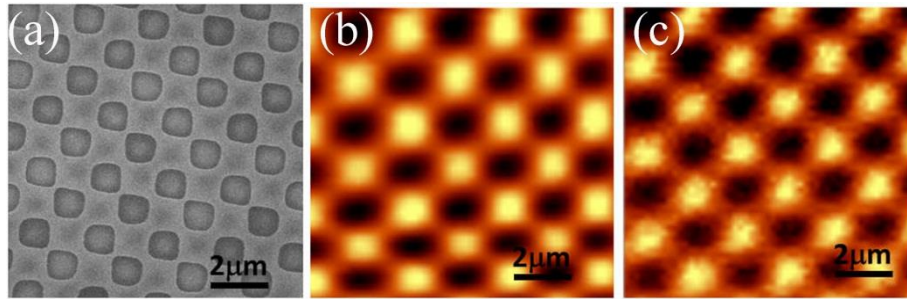


Figure 2.6 (a) SEM image of the sample. (b) Rayleigh mapping image of the calibration sample at room temperature ($\sim 300\text{ K}$). (c) Rayleigh mapping image of the calibration sample at low temperature ($\sim 5\text{ K}$).

Chapter 3 Electron beam writing and metal deposition effects on graphene

3.1 Introduction and motivation

Electron beam writing and metal deposition are commonly used processes during the fabrication of graphene based devices [45]. Both electrons and metal atoms are energetic and may have bombardment effect on graphene lattice during these processes. The lattice of the graphene could be changed after the bombardment since graphene itself is as thin as only one atomic layer. Physical properties of graphene, like the carrier transport and thermal conductivity, may significantly alternate after these changes.

No clear consensus about the influence of e-beam irradiation has been reached yet. The influence of energetic irradiation of electrons on graphene properties were investigated by many researchers in the community [27, 46-52]. Some interpretations propose that the irradiation of electron beam transformed graphene into small crystallite first and then into amorphous carbon [27, 47]. Some investigations emphasize that e-beam irradiation may convert graphene into graphane through reversible hydrogenation or make graphene partially hydrogenated with adsorbates such as H_2O [48, 51]. Some works mention that the e-beam generates mobile oxygen from the underlying layer of SiO_2 [49, 50]. The oxygen could possibly induce

oxidation effect on the graphene layer. What's more, in the real e-beam lithography process, graphene is coated with a thin layer of e-beam resist. Graphene is not exposed to the e-beam bombardment directly in this real case. Therefore, it is meaningful to make further investigations for the understanding of the e-beam irradiation phenomena in graphene systems during device fabrication process.

Metal deposition effect on the lattice of graphene is something new and interesting. Beside electron irradiation, metal atoms during the physical evaporation process are powerful and may damage graphene lattice more seriously than electrons during the lithography process. There are mainly two reasons. First of all, metal atoms may carry larger momentum because that they are much more massive than electrons. Secondly, metal atoms are directly evaporated onto the surface of graphene to form contacts. Metals (like Ti, Au) are commonly used for contact electrodes in graphene devices. It had been reported that graphene is quite sensitive to the deposition of metals. The metal deposition leads to the electronic doping and scattering in graphene [53, 54]. Although the doping effect of these metals on the electronic properties of graphene has been known, however, detailed study of lattice variation after metal deposition is still lacking and needs further investigation. The electron and metal-atom bombardment effects on graphene in actual device fabrication processing were discussed in this chapter, and these effects were mainly characterized by Raman spectroscopy.

3.2 Experimental results

3.2.1 Experimental details

Techniques including micro-Raman spectroscopy and atomic force microscopy were adopted to study the effects of e-beam irradiation on pristine exfoliated graphene in order to understand how the disorder is introduced in the material in detail. For the experimental setup, a commercial WITEC CRM200 Raman system was used to acquire Raman spectra. The solid state laser (wavelength at 532 nm, or energy at 2.33 eV) which is below 0.1 mW was adopted in order to avoid heat induced damage to the graphene samples. The numerical value is 0.95 for the objective lens that was used in the Raman measurements. The spot size can be about 500 nm in diameter in this system. Atomic force microscope (AFM, Veeco-NanoScope V system) characterized the surfaces of samples in tapping mode. AFM tips which possess tip radius smaller than 10 nm came from AppNano (ACT-30). No flatten or smooth process was applied to original AFM images. Electron beam irradiations were carried out in a dual beam (electrons and ions) system from Zeiss (AURIGA series). Dose of the irradiation of electrons can be controlled by the system equipped with an electron beam blanker. The accelerating voltage is fixed at 20 kV. The probing current is at a constant value of 20 pA. Electrical properties were measured by Keithley 4200-SCS parameter analyzer. Drain-source bias voltage was fixed at 0.1 V for the gate voltage (V_g) versus resistance(R) curve.

The graphene flakes were peeled-off from natural graphite by using scotch tape method and transferred onto a silicon substrate with a 300 nm SiO₂ capping layer. Typically, single-layer graphene (SLG) among the flakes are about 30-100 μm^2 in size. Locations of the graphene samples can be quickly examined by optical microscope and thickness of the samples can be identified by Raman spectroscopy [15, 16].

3.2.2 Lattice properties of graphene after e-beam irradiation

Figure 3.1a shows the optical image of one representative SLG sample on SiO₂/Si substrate. The AFM topographic image and Raman spectrum of the sample are shown in Figure 3.1b and 3.1c, respectively. Four regions (see in Figure 3.1d) with same size of 3x3 μm^2 are exposed with diverse electron dosages of 0.03, 0.3, 3 and 30 nC/ μm^2 , indicated by red, blue, green and purple dash line frames, respectively. Under optical microscope, two regions regarding to more severe irradiation (3 and 30 nC/ μm^2) could be clearly seen after electron beam irradiation. As shown in the AFM height image of Figure 3.1e, height values of these two regions appear to be about 1.8 nm and 3.4 nm, respectively. Raman spectra from the regions were taken and shown in Figure 3.1f to further investigate the e-beam irradiation effects. D peak which locates around 1350 cm^{-1} is a fingerprint of disorder in graphene based materials. Even under the smallest dosage value of 0.03 nC/ μm^2 , D peak still can be observed after e-beam irradiation. The intensity ratio of the D peak and G peak is increasing from 0.05, 0.86 to 2.75 with the dosage values increasing from 0.03, 0.3 to 3 nC/ μm^2 . It implies that more disorder was introduced into graphene lattice when the D peak intensity was

enhanced with the increase of electron dosage. D peak comes to be very broad and partially merge with G peak when the electron dosage was as large as $30 \text{ nC}/\mu\text{m}^2$, typically is a spectral feature of highly disordered or amorphous carbon. Results shown above clearly prove that additional layers of amorphous carbon are deposited on graphene.

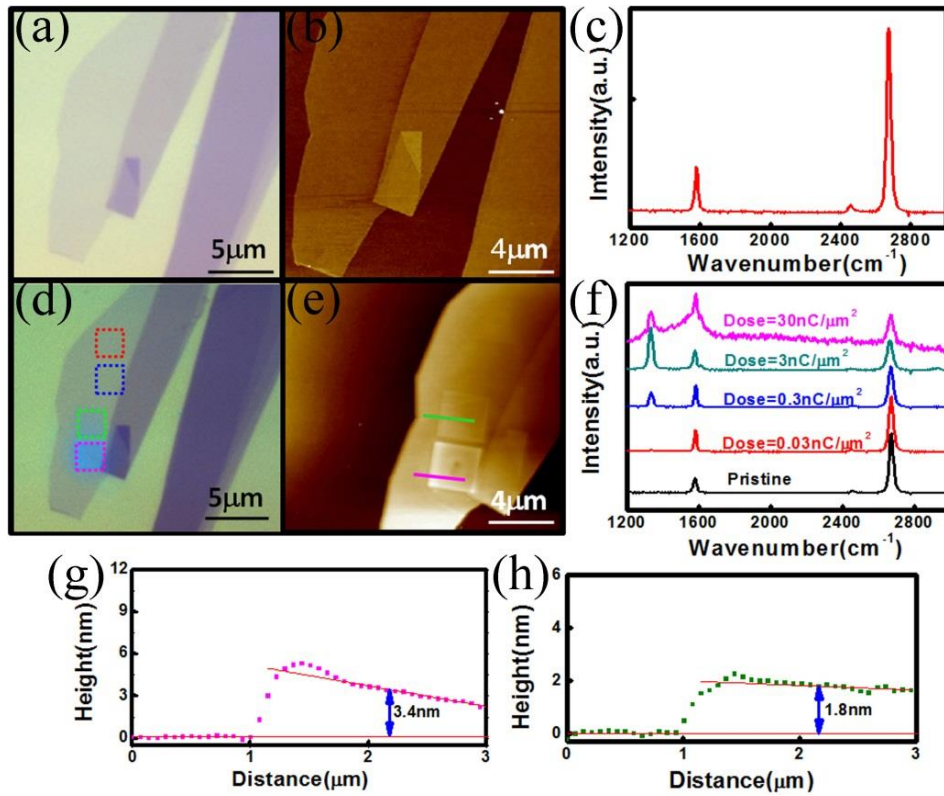


Figure 3.1 Electron beam irradiation effects on graphene. Optical (a) and AFM (b) topographic images of one as-exfoliated graphene sample on SiO_2/Si substrate. (c) Raman spectrum of the monolayer graphene. Optical (d) and AFM (e) topographic images of the same sample after e-beam irradiation. Four squares of $3 \times 3 \mu\text{m}^2$ are exposed to e-beam with dosages of 0.03, 0.3, 3, $30 \text{ nC}/\mu\text{m}^2$, respectively. f) The Raman spectra from the regions inside the four squares, and pristine graphene.

Raman intensities are normalized intensities. (g-h) height profiles for the two lines in (e), respectively.

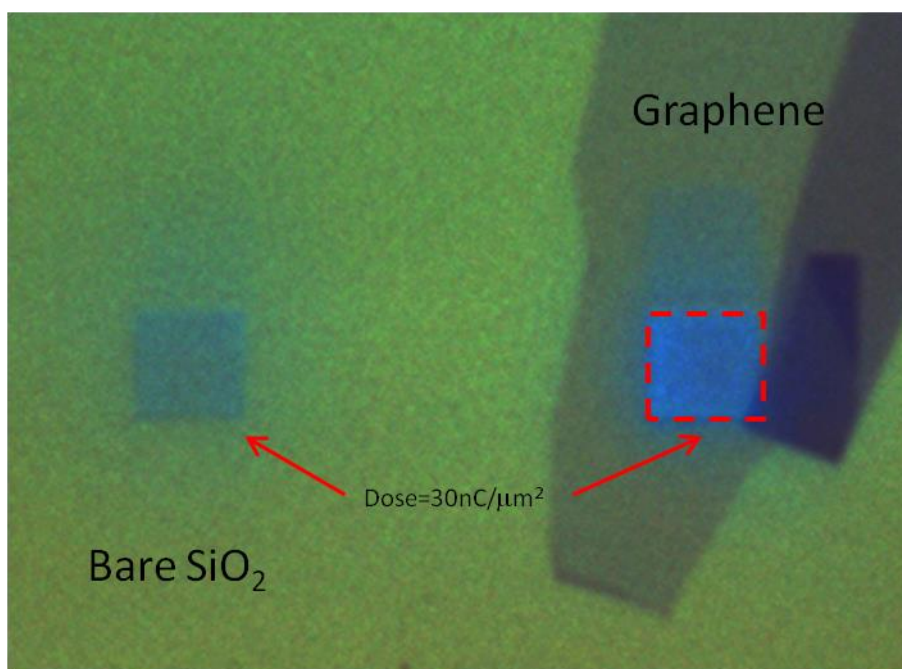


Figure 3.2 Optical image of the sample after electron beam irradiation

Figure 3.2 shows the optical image of the regions where irradiated with electron beam on the bare SiO₂/Si substrate. Similar to graphene surface, after electron beam irradiation, the region irradiated with 30 nC/μm² exhibits obvious contrast under optical microscope. Some authors claimed that e-beam bombards graphene flake into crystallite and then into amorphous carbon [27]. However, in our experiments, the amorphous carbon is mainly from the organic hydrocarbon vapor in vacuum chamber and deposited on graphene surface by electron induced deposition. In order to confirm our claim, the bare areas of 3 × 3 μm² size on SiO₂/Si substrate beside the graphene are

exposed to e-beam with the dosage of 0.03, 0.3, 3 and 30 nC/ μm^2 , respectively. Formation of the square is believed due to the electron induced deposition of organic hydrocarbon in vacuum chamber. Raman characterization was carried out on the squares, and the Raman spectra are shown in Figure 3.3. As shown in the Figure 3.3, Raman signals on square areas on bare SiO₂ are too weak to detect while the Raman signal of G, D, and G' band are detected on square area in graphene flake. Amorphous carbon normally may generate D-peak. However, in our case, the amorphous carbon on SiO₂ substrate does not exhibit any D peak in its Raman spectra (see Figure 3.3). It may attribute to the little amount of the amorphous carbon. Therefore, the D peak observed on square area in graphene sample should be due to the damaged lattice in graphene. The presence of sharp G peak indicates graphene are not completely transformed into amorphous carbon in spite of heavy damage.

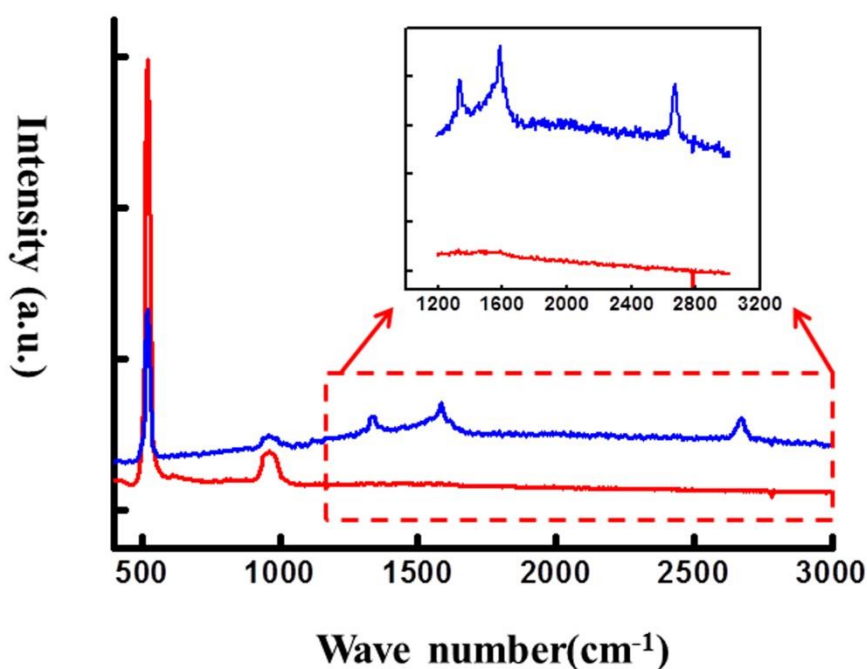


Figure 3.3 Raman spectra of amorphous carbon on substrate (red curve) and on graphene (green curve). No D peak observed in amorphous carbon itself. Inset image is the zoom in of the range from 1200 cm^{-1} to 3000 cm^{-1} .

E-beam irradiation effects can be three-fold. First, it could be that energetic electrons with high speed may break the bonds among the lattice structure in graphene. Defects like Stone-wales defects or reconstructed vacancies can be induced by powerful electrons in transmission electron microscopy (TEM). Carbon atoms in graphene can be knocked away [26, 55]. It is calculated that the minimum energies to introduce the Stone-wales defects and vacancies in graphene are about 5 eV and 8 eV, respectively [56]. Thus, some works believe that carbon atoms are knocked away or re-constructed in graphene [27, 47, 57, 58]. Secondly, disorder on the lattice system

could be induced by the amorphous carbon layer which was deposited on the surface of graphene. Not much attention was paid to this phenomenon in the previous works on e-beam effects. Electron beam induced deposition is a well-known phenomenon and has been studied in early times. Amorphous carbon films were deposited on the substrate surface in the vacuum chamber due to the interaction of electrons and organic contamination [59, 60]. Therefore, electron beam should induce foreign atoms onto graphene surface. Large amount of irradiation would introduce relative thick amorphous carbon film on graphene. When the dosage of electron beam reach to the value of $30 \text{ nC}/\mu\text{m}^2$, obvious deposited amorphous carbon thin film could be seen from the optical image (Figure 3.1d) and revealed in the Raman spectrum (Figure 3.1f). Similar to adsorbates that can make graphene to be partially hydrogenated, the amorphous carbon films should also introduce defects [48, 51, 61, 62]. Thirdly, different kinds of energetic ions (*e.g.* O^- , Si^- , Si^+ , Si^{2+} and Si^{3+}) can be generated from the SiO_2 substrate when the energy of irradiated electrons are higher than 100 eV [63]. The ions with high energy induced by the e-beam irradiation would impact with graphene and introduce defects into graphene lattice [64]. These three reasons mentioned above could contribute to the generation of defects in graphene sample at the same time.

Electron beam lithography is a technique which is broadly used for device preparation. In the real lithography process, graphene samples are not directly

exposed to the large amount of energetic electrons. Normally, one layer of e-beam resist (PMMA) is on top of graphene surface. Two layers of resist were spin coated in our work. One layer is 300 nm methyl methacrylate and the other layer is 150 nm PMMA. Then square regions ($3 \times 3 \mu\text{m}^2$) on graphene were exposed with electron dosage of $0.004 \text{ nC}/\mu\text{m}^2$. Thus, the effect of the e-beam lithography can be tested after development. Raman spectra were collected both before and after the lithography process.

Figure 3.4a presents optical images of the as-exfoliated SLG and the same sample after lithography and develop processes. Raman spectra are compared in Figure 3.4b to see the change. Raman D peak can be clearly observed after the lithography process in graphene. This means that defects in graphene still can be introduced by the e-beam even when the sample is covered with two layers of resist. No D peak can be detected on the regions without e-beam irradiation. The results are different from the ones shown in a previous work [65]. Experiments on bilayer graphene (BLG) were carried out for comparison. Optical images and Raman spectra can be found in Figure 3.4c and 3.4d, respectively. D peak is undetectable after the lithography process for the BLG. This indicates that BLG is relatively more robust to the e-beam irradiation compared to SLG. This can be possibly explained that BLG has a higher energy barrier for the defect formation than SLG [66].

Amorphous carbon on the surface of resist can be taken away after develop process. Therefore, the possibility for deposition of amorphous carbon onto graphene is

extremely low in this case. Though two layers of resist covers graphene, the electrons with high speed can pass through the resist and meet the surface of graphene [67, 68]. Interactions between energetic electrons and graphene sample are still there. The interactions would include collisions among the electrons, graphene lattice and ions which are generated from substrate. Defects would be possible due to these interactions. The frequency of the G' peak is red-shifted after e-beam irradiation. It implies that the concentration of electrons in graphene increased after e-beam exposition [17]. This allows the discrimination between electron and hole doping based on the shift of the G' peak.

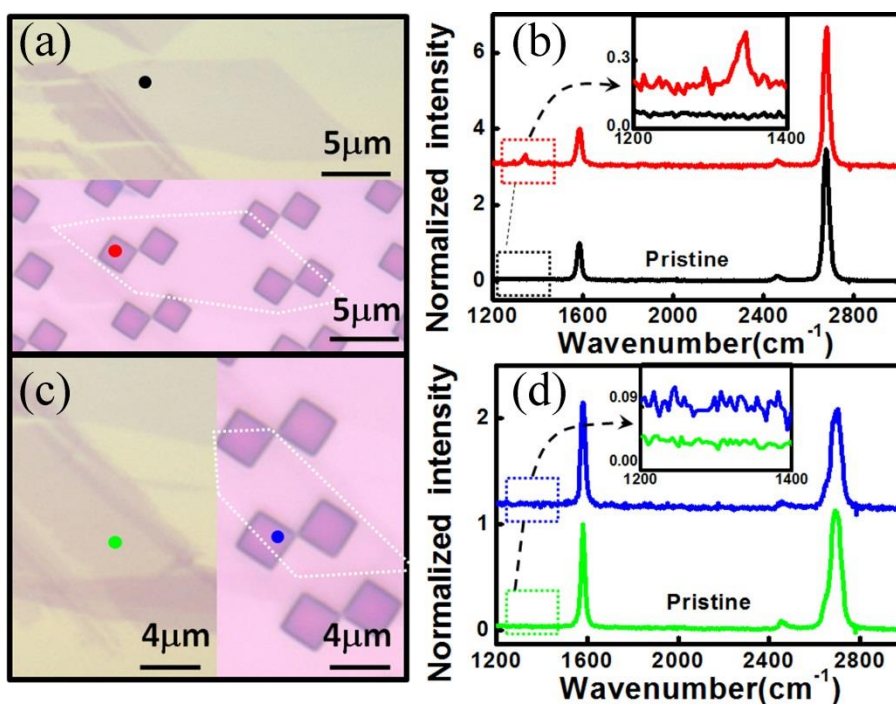


Figure 3.4 Electron beam lithography effect on monolayer and bilayer graphene samples. (a) Optical images of the as exfoliated graphene (up) and the same sample

coated with resist after develop process. The square regions were exposed to e-beam.

(b) Raman spectra of the SLG collected from the red and black spots in (a). The inset shows the details of D peak for clarity. (c) Optical images of the pristine BLG and BLG coated with resist after develop. The thickness of the resist and dosage of e-beam are the same as for SLG. (d) Raman spectra of BLG collected from the green and blue spots in (c). The inset shows the details of D peak for clarity.

3.2.3 Metal deposition effects on electronic structures of graphene

Metal evaporation is a necessary step for the contact formation to fabricate graphene based devices after EBL process. Gold (Au) film combined with a relative thin adhesion film like titanium (Ti) layer are widely employed in the fabrication process of graphene transistor. We investigated the effects of depositing these metals (titanium and gold) on the lattice structure of graphene. Electron beam evaporator is the system to deposit these metals onto the surface of graphene. The thickness of the coated metals films can be measured by a commercial crystal thickness sensor.

Figure 3.5a and Figure 3.5b are the optical images of the sample before and after the deposition. One sample consisting of both SLG and BLG regions is prepared. Ti layer with a thickness of 5 nm is coated onto the sample through electron beam evaporation. Effects of depositing a thin Ti film on both SLG and BLG are examined by the Raman spectroscopy. The Raman spectra collected are plotted in Figure 3.5c and 3.5d. No D peaks were detectable for both SLG and BLG after Ti thin film

depositing. These results indicate that coating of titanium adhesion layer is almost impossible to induce defects to the lattice of graphene sample. The phenomenon might be understood that the kinetic energy of evaporated Ti atom is too low to break the carbon-carbon bonds in graphene [69, 70]. What's more, the frequency of G' peak shifts about 10 cm^{-1} toward lower wavenumber after the Ti layer deposition for the monolayer graphene.

Figure 3.5e shows the electrical characterization of the graphene transistor which was prepared to study the influence of the deposition of Ti layer. From the transport data, it is slightly p-type doped and the neutral point is at 3 V for the SLG device before Ti deposition. However, the neutral point (NP) is at -25.6 V with Ti coating. This NP shifting means that n-doping in graphene is induced after the Ti deposition. Raman spectra from the graphene device were also collected. We found that D peak is absent and G' peak red-shifts after the deposition of Ti layer. The Raman results also indicate n-doping of the sample after Ti deposition. Thus, findings from both Raman and transport measurements are consistent. And these conclusions agree well with previous reports [17, 53].

What's more, Figure 3.5f presents the transport curves of bilayer graphene transistor that were also conducted for the study on Ti deposition effect. The extracted NP of BLG changed from 14.6V (p-doping) to -16V (n-doping) after Ti coating. From this NP shifting result, Ti also introduces n-type doping in BLG. The n-type doping can be explained by the charge transfer between Ti and graphene [71, 72]. Electrons

from Ti are expected to be transferred to graphene because that the work function of monolayer graphene ($\phi_{\text{graphene}} \sim 4.5$ eV) is a bit larger than that of Ti ($\phi_{\text{Ti}} \sim 4.3$ eV) [73-77].

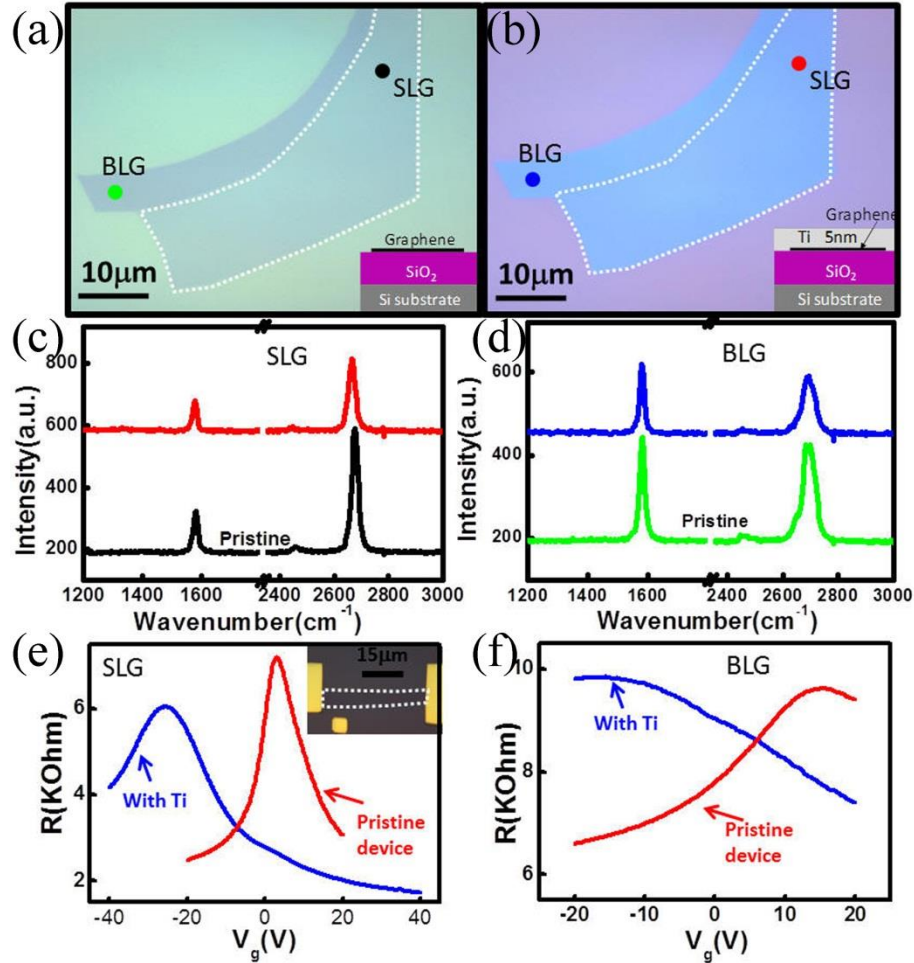


Figure 3.5 Ti deposition effects on monolayer and bilayer graphene samples. (a) Optical image of pristine graphene sample consisting of both SLG and BLG regions. (b) Optical image of the graphene sample with a 5 nm Ti thin film. The insets in (a) and (b) show the schematic structures of the samples. (c) Raman spectra of SLG

before and after Ti deposition. (d) Raman spectra of BLG before and after Ti coating. (e) Resistance as a function of back gate voltage for SLG device before and after Ti deposition. (f) Resistance as a function of back gate voltage for BLG device before and after Ti deposition.

Au layer were deposited onto the graphene surface by electron beam evaporation. A hard mask (TEM Grid with the bar width of 10 μm) was used to reduce the damage [78]. Electrodes which are made of Ti/Au (5 nm/60 nm in thickness) are evaporated onto graphene. There would be some spacing between mask and the substrate because that some adhesive residues would be possibly sitting in between the mask and substrates. The spacing could be about several micrometres. Due to the existence of this spacing, those metal atoms would typically invade the spacing below the shadow mask by about tens of micrometres. The impact of deposition of Au electrodes on graphene was investigated by taking advantage of this atom invading effect. Properties of the graphene samples after Au deposition were characterized by Raman spectroscopy.

Figure 3.6a shows three different positions which are gradually away from the contact metal in the optical image. The Raman spectra collected from corresponding positions can be seen in Figure 3.6b. It is observed that the D peaks of SLG sheets came out when they are close to the electrode. The intensity of D peak is larger when

monolayer sheet is closer to the electrode. Results from BLG can be seen in Figure 3.6d and Figure 3.6e. Similar conclusions can be obtained in the case of BLG. The emergence of D peak is certainly ascribed to the deposition process of Au thin film onto graphene because the deposition process of Ti adhesion layer does not introduce detectable disorders to the lattice of graphene. Observation of Raman D peak after direct gold depositing onto graphene has been mentioned in earlier reports [79, 80]. Au atoms should have higher kinetic energy than Ti atoms when they are evaporated into the vacuum chamber of the evaporator.

The carrier mobility could be efficiently estimated through Raman measurements. The integrated intensity ratio of D and G peak (I_D/I_G), which indicates the intervalley scattering rate of distributed disorder, is calculated for the analysis of the D band observed after the electrode deposition. The average distance between the scatters in graphene can be estimated based on the empirical formula. The crystallite size L_a of nanographene can be extracted by the result from Raman spectroscopy [58, 81] :

$$L_a = (2.4 \times 10^{-10}) \lambda_L^4 (I_D/I_G)^{-1} \quad (3.1)$$

where $\lambda_L = 532$ nm stands for the wavelength of the excitation laser. We found that $L_a = 22.3$ nm when $I_D/I_G = 0.867$ (data of green spot in Figure 3.6a). Information about the average scattering distance in the disordered graphene can be known from the value of L_a . It can be expected that L_a equals to the transport mean free path l when carriers are in the large-angle scattering case, although Raman spectroscopy at $\lambda_L =$

532 nm detects the scattering rates at the energy one order of magnitude larger than the typical Fermi level in transport experiments [28]. For Dirac fermions in graphene, carrier mobility can be written as [28]:

$$\mu = \frac{l \cdot e v_F}{E_F} = (2.4 \times 10^{-10}) \frac{e v_F}{E_F} \lambda_L^4 \left(\frac{I_D}{I_G} \right)^{-1} \quad (3.2)$$

where $v_F \approx 10^6 \text{ ms}^{-1}$ is the Fermi velocity and $e \approx 1.6 \times 10^{-19} \text{ C}$ is the elementary charge. Suppose that the energies of the electrons and holes based on the energy of excitation laser at $\lambda_L = 532 \text{ nm}$, and both locate at the absolute value of $E_F = 1.17 \text{ eV}$ when $l \approx L_\alpha = 22.3 \text{ nm}$. The value of carrier mobility can be acquired: $\mu \approx 191 \text{ cm}^2 \text{V}^{-1} \text{s}^{-1}$. The observation implies that the deposition of Au thin film may greatly reduce the quality of graphene.

Figure 3.6c presents the resistance of the pristine SLG device as a function of back gate voltage before and after Au deposition. The value of NP for the SLG device shifted from its pristine 10 V to a value which should be larger than 30 V when the device was coated with gold. This result implies that gold deposition can introduce hole (or *p*-type) doping in SLG. Holes are transferred into the graphene due to the fact that Au possesses a relative larger work function compared to graphene ($\phi_{\text{graphene}} \sim 4.5 \text{ eV}$ and $\phi_{\text{Au}} \sim 5.1 \text{ eV}$) [75-77]. Carrier mobility of the graphene device can be obtained according to below formula [82]:

$$R_{\text{Total}} = R_{\text{contact}} + \frac{L}{W e \mu \sqrt{n_0^2 + n^2}}, \quad n = \frac{C |V_g - V_{\text{Dirac}}|}{e} \quad (3.3)$$

Where R_{Total} is the total resistance. L and W stand for the length and width of the device, respectively. n represents the carrier density and n_0 means the residual carrier concentration in the device. μ is the mobility of the device. $C = 1.15 \times 10^{-4} F/m$ is the capacitance of the insulation layer (300 nm SiO₂). The extracted carrier (hole) mobility of the pristine SLG device is about $4200 \text{ cm}^2\text{V}^{-1}\text{s}^{-1}$ and the value decreases to $568 \text{ cm}^2\text{V}^{-1}\text{s}^{-1}$ when the device is coated with gold thin film. From Raman result, obvious Raman D peak was observed in the SLG device after Au deposition. The carrier mobility can be obtained based on the integrated intensity ratio of D and G peak of the graphene device [28]. $I_D/I_G = 0.282$ corresponds to $\mu \approx 582 \text{ cm}^2\text{V}^{-1}\text{s}^{-1}$. Interestingly, the carrier mobility extracted from Raman measurement agrees well with the one obtained from transport measurement in the same sample. Transport characterization for a BLG device is shown in Figure 3.4f. By analysing the result, the hole mobility of the BLG device changed from $2426 \text{ cm}^2\text{V}^{-1}\text{s}^{-1}$ to $616 \text{ cm}^2\text{V}^{-1}\text{s}^{-1}$ when the device is coated with one Au thin film.

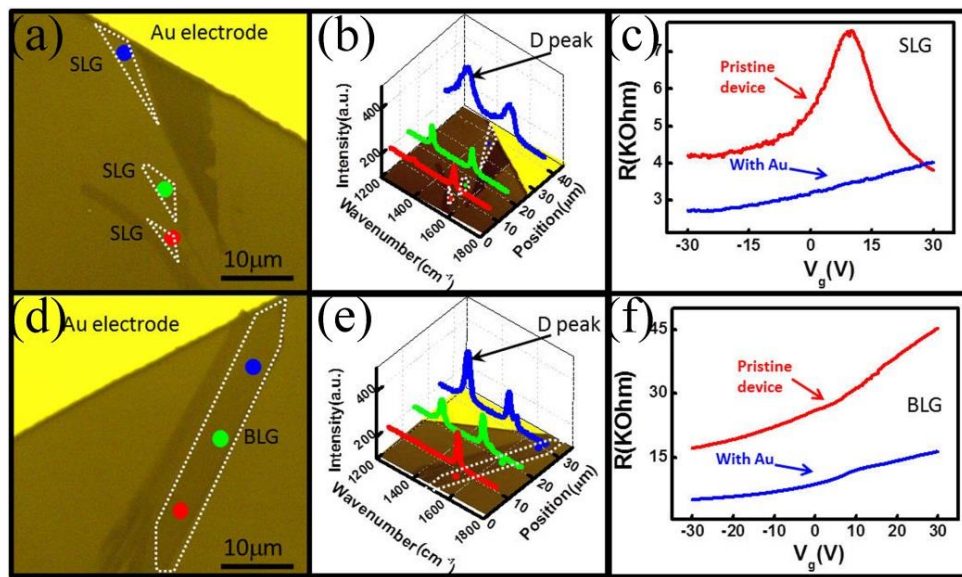


Figure 3.6. Direct evaporation of Au can introduce defects to SLG and BLG. (a) Optical picture of one graphene sample coated with Ti / Au electrode. (b) Raman spectra of three locations of the SLG samples in (a). (d) Optical picture of the bilayer graphene sample coated with Ti / Au electrodes. (e) Raman spectra of three locations of the BLG samples in (c). The SLG and BLG areas are indicated by the dash-line frames. (c) Resistance as a function of back gate voltage in SLG device before and after Au deposition. (f) Resistance as a function of back gate voltage in BLG device before and after Au deposition.

Figure 3.7c and Figure 3.7d show atomic force microscope (AFM) measurements on both SLG and BLG samples (see Figure 3.7a and Figure 3.7b). Figure 3.7e shows an AFM height image on an area which is away from the metal electrode. However, it contains two regions (R1 and R2, R2 is closer to electrode than R1) which show difference in surface roughness. Mean root squared roughness of R2 and R1 are 0.237 nm and 0.113 nm, respectively. The roughness difference in two regions can be ascribes to the existence of metal atoms (Ti and Au atoms). Region 2 has a small surface roughness and can be considered to be the substrate without metal atoms. It is also observed that graphene surface roughness increases with the distance to the metal electrode decreasing. AFM measurement results help to confirm the existence of the metal atoms on the graphene surface after metal deposition by using a hard mark.

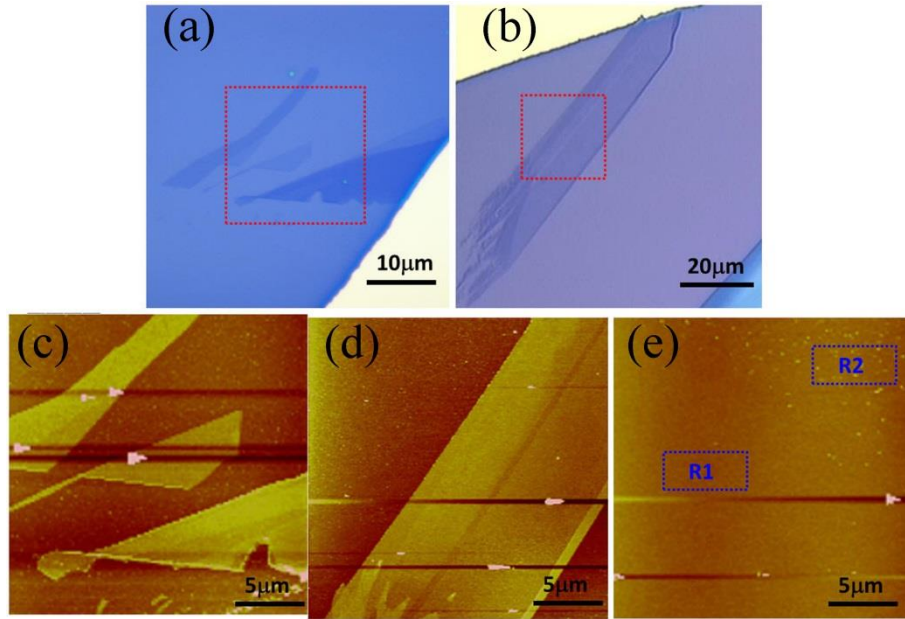


Figure.3.7 (a-b) Optical images of the SLG and BLG samples. Red dashed squares indicate the areas where AFM measurements were carried out. (c-d) AFM height images of SLG and BLG samples, respectively. (e) AFM height image on an area which is away from the electrodes. Region 1(R1) and Region2 (R2) show difference in roughness.

3.3 Conclusions

We have carried out studies on the effects of electron beam irradiation and metal deposition on graphene lattice during actual device fabrication processes. Both of these two processes could introduce defects to graphene lattice. Severe electron beam irradiation could induce the amorphous carbon deposition, which is often ignored in previous works. In real EBL processing, the electron beam with high energy could

directly destroy the lattice structure of graphene by knocking off carbons or enabling the reaction between graphene and substrate. Bilayer graphene presents higher stability under e-beam irradiation than monolayer graphene does. In the formation of metallic contact, Ti could not introduce defects in graphene while Au remarkably damage graphene lattice. These experimental findings reveal the influence of the fabrication techniques on graphene lattice and could benefit for the optimization of processes.

Chapter 4 Magneto-Raman scattering of monolayer graphene on graphite

4.1 Introduction

Graphene which consists of only one atomic layer of carbon atoms exhibits lots of fascinating fundamental physical properties because its charge carriers behaves like massless Dirac fermions [13]. Graphene sample with ultra-high quality is important for many experimental studies based on fundamental physics in graphene. Particularly, the high quality of graphene samples can be revealed by the long lifetime of the Dirac fermions according to the narrow spectral widths of the Landau levels [37].

Width of the LL in graphene can be useful information to evaluate properties like the degree of defects and sample quality. Quantized energy levels, which can be named as Landau levels with Landau index n , will form when the graphene is under a strong magnetic field perpendicular to its crystal lattice. Different measurement techniques are developed to probe the LL width of graphene, such as magneto Raman spectroscopy [37, 38], infrared spectroscopy [83, 84], scanning tunnelling spectroscopy (STS) [40, 85, 86] and cyclotron resonance [87]. During those previous works, different samples were used like pure graphene sheet which was found to be decoupled from the graphite substrate due to the twist angle between the layers [88] or

become physically detached from the Bernal-stacked layers underneath [89, 90] (hereafter we call this structure “graphene on graphite”) [37, 38, 40], or epitaxial few layer graphene grown on SiC [84, 86]. For example, using infrared spectroscopy, the LL spectral width of mechanically exfoliated graphene on a Si/SiO₂ substrate is about 40 meV [83] and of the non-Bernal-stacked ~ 100 layers of epitaxial graphene on SiC is between 4 meV (at $B = 60$ mT) and 10 meV (at $B = 4$ T) [84]. However, using STS, the LL widths of the decoupled graphene on graphite and in epitaxial graphene were found to be ~ 10 meV [40] and ~ 1.5 meV [86], respectively.

Raman spectroscopy is a non-destructive technique and can be used in different environments. At ambient pressure, it has been widely applied to characterize nanocarbon materials [21, 91-93]. It is also developed to probe materials under different environments or modifications like that the samples are exposed to an external magnetic field [94-98]. The rich physics of graphene in the presence of magnetic fields can be studied by the magneto Raman scattering [33, 34, 36-38]. Particularly, magnetophonon resonance will happen when the energy of the electronic excitation for inter-LL transition (or named as magnetoexcitons) equals to the energy of the G peak phonon (~ 196 meV) [99]. In monolayer graphene, the MPR effect has been predicted to happen and show anti-crossing behaviour for the Raman G mode [33, 34].

Recently, several experimental works have confirmed the existence of MPR effect in several kinds of graphene samples [36-38]. Through magento-Raman scattering measurements, the collected Raman G peaks can be fitted into two peaks under various magnetic fields in multilayer epitaxial graphene. One peak is magnetic independent and the other shows obvious oscillations for both energy and width [36]. Based on Ando's model, parameters can be extracted from simulation work. The spectral width of LL in this particular sample is 90 cm^{-1} ($\sim 10 \text{ meV}$). Jun Yan *et al.* distinguished a region on the surface of exfoliated graphite which shows properties similar as a monolayer graphene by MPR effect. However, the spot size of their laser beam is $\sim 80 \text{ }\mu\text{m}$ [37]. From their results, pronounced anti-crossing behaviour of two coupled modes as predicted was observed when the magnetic fields were close to 5 T. The strong interaction of the LL transitions and G band phonons in that sample give rise to the anti-crossing behaviour. This width of LL level transition at 5 T for this MPR is about 26 cm^{-1} ($\sim 3 \text{ meV}$). Later on, Faugeras *et al.* developed a Magneto-Raman system which is capable to have a laser spot as small as $\sim 1 \text{ }\mu\text{m}$ while the magnetic field can be as high as 32 T. They did detailed investigation on graphene-like domains on natural graphite and the LL width is found to be 25 cm^{-1} ($\sim 3 \text{ meV}$) for 2.8 T [38]. However, the interactions between LL transitions and G-band spectral phonons would be enhanced when the LL width is very close to the intrinsic spectral width of the G-peak ($\sim 10 \text{ cm}^{-1} = 1 \text{ meV}$). Thus, graphene samples which possess higher quality compared to those reported ones in previous works are needed.

In this chapter, our experimental set up enables us to do a Magneto-Raman mapping on the surface of natural graphite with a laser spot as small as $\sim 1 \mu\text{m}$. At 5 T, graphene-like regions which decouples from the graphite substrate can be quickly identified through Raman mappings before detailed MPR study. Specifically, a domain performs like decoupled graphene was found after the mechanical exfoliation process. Detailed information about the interaction of the magnetoexcitons and the G peak phonons from this domain were revealed by a high resolution magneto-Raman measurement. The LL spectral width from this domain is as narrow as 10.6 cm^{-1} ($\sim 1.3 \text{ meV}$). Eight traces of LL transitions crossing the G mode can be clearly distinguished from the experimental observation. Those LL transitions can be assigned to be both symmetric and asymmetric based on their energies under magnetic fields. Those asymmetric LL transitions show strong MPR and anti-crossing behaviour as expected. Particularly, for the LL transition from $n = -2$ to 1, the Raman G peak unambiguous shows to be three peaks (G_- , G_i and G_+) over a certain range of magnetic fields around $B \sim 4.65 \text{ T}$. This phenomenon has been expected to exist [37], but had not been resolved in earlier reports due to the large values of those observed LL spectral widths. Detailed evolutions of the three resolved peaks in a range of magnetic fields were shown by our observation. By doing simulation according to existing theoretical models, we can quantitatively study the interaction of the LL transitions and G band phonons. What's more, a new feature is found to be magnetic field dependent. This is proposed to be understood by the coupling between

magnetoexciton-phonons of graphene and the graphite phonons. Simulation work is derived by using a driven harmonic oscillator model. The obtained results display a new understanding of a phonon-phonon coupling between the decoupled graphene layer and the graphite substrate mediated by magnetoexcitons. Therefore, this magneto-Raman technique can be an important way leading to many body effects for graphene or other 2D materials by studying their LL spectra.

4.2 Experimental results

4.2.1 Experimental details

Graphite samples (typically $\sim 100\ \mu\text{m}$ in lateral size) were mechanically exfoliated from natural bulk graphite onto a silicon substrate capping with a layer of 300 nm SiO_2 by scotch tape method. A customer designed Magneto-Raman system was set up [see Figure 2.5 in chapter 2] for the observation of the MPR effect on decoupled graphene samples on graphite substrate at low temperature ($\sim 5\ \text{K}$) and in high magnetic fields.

The wavelength of the laser is 532 nm (Nd: YAG, solid state laser). Power of the laser was kept below 5 mW to avoid too much heat on the sample. Core diameter of the single mode fiber to introduce the incident laser is $5\ \mu\text{m}$. The focused spot size of the laser can be as small as about $1\ \mu\text{m}$ in diameter after optimizing the optical path for the Raman system. The multimode optical fiber which was used to collect scattered light has a diameter of $50\ \mu\text{m}$ in core. The collected light signals went into a

spectrometer which possessing a grating of 1800 grooves/mm. The CCD detector is thermoelectrically cooled down. The excitation laser beam and the Raman signal were linear polarized while not circularly polarized in our experiments, therefore signals including both of the two circular configurations (co-circular and cross-circular) could be simultaneously collected.

The tube which holds the sample is pumped to a high vacuum (about 1×10^{-5} mBar) before cooling down. Little amount of helium gas was then filled into the tube (final pressure was about 20 mBar) as media for heat transfer. Sample can be cooled down to 4.2 K in the liquid helium bathed cryostat. A magnetic field which is perpendicular to the surface of graphene up to 9 T can be generated by a superconducting magnet. Coarse movements in X-Y-Z directions are capable. Fine Raman mapping in a range within $30 \times 30 \mu\text{m}^2$ is available in the system with the help of a nonmagnetic piezo stage. All the magneto-Raman scattering data were collected when the temperature is about 5 K.

For the identification of the decoupled monolayer graphene on top of the graphite, a commercial atomic force microscope was used. The environment of the AFM was controlled to reduce the noise information which may be caused by the water in the atmosphere. A saturated salt solution of lithium chloride was placed into the AFM chamber which was sealed during the measurements. Thus, a low relative humidity (RH) level of about 11% ($\pm 1\%$) was provided and maintained in order to

enhance the detection sensitivity. The samples were characterized by using MikroMasch DPE14 probes which normally have a resonance frequency of 160 kHz and a force constant of 5.7 N/m in the acoustic alternating current (AC) mode.

4.2.2 High quality sample and triple splitting of G mode

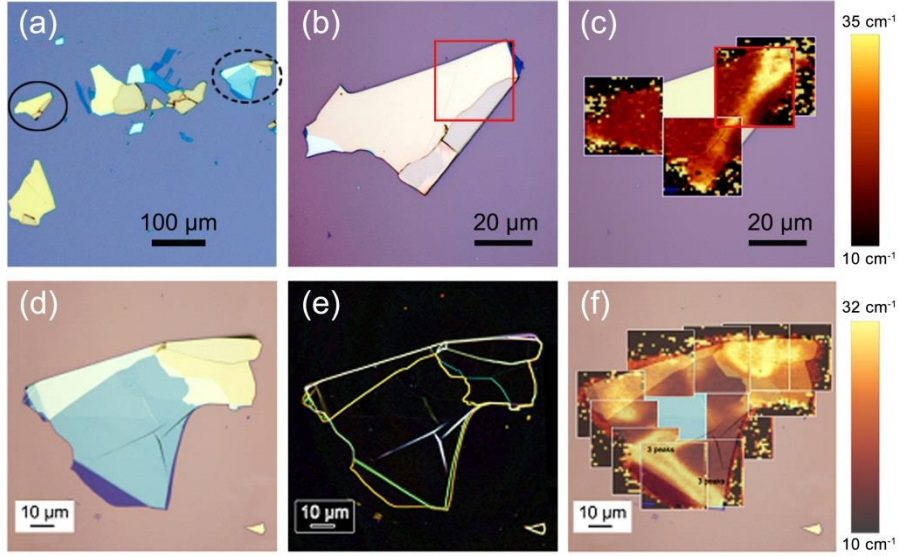


Figure 4.1 (a) Optical image of several as exfoliated graphite samples on a SiO_2/Si substrate. After examining these samples, two of these flakes show prominent MPR phenomenon, which are marked by solid/dashed black ellipses. (b) Optical image of the graphite sample which is inside the solid ellipse in (a). The MPR results shown in this chapter is measured from the red square region on this sample. (c) Raman mapping images of the G band width at $B = 4.8 \text{ T}$ are combined with the optical image. The colour scale showing the spectral width of the G band is on the right side. Original (d) and “glowing edge” filter applied (e) optical images of the graphite sample which is inside the dashed ellipse in (a). (f) Raman mapping images of the G

band width at $B = 4.8$ T are merged together with optical image of the graphite flake shown in (d).

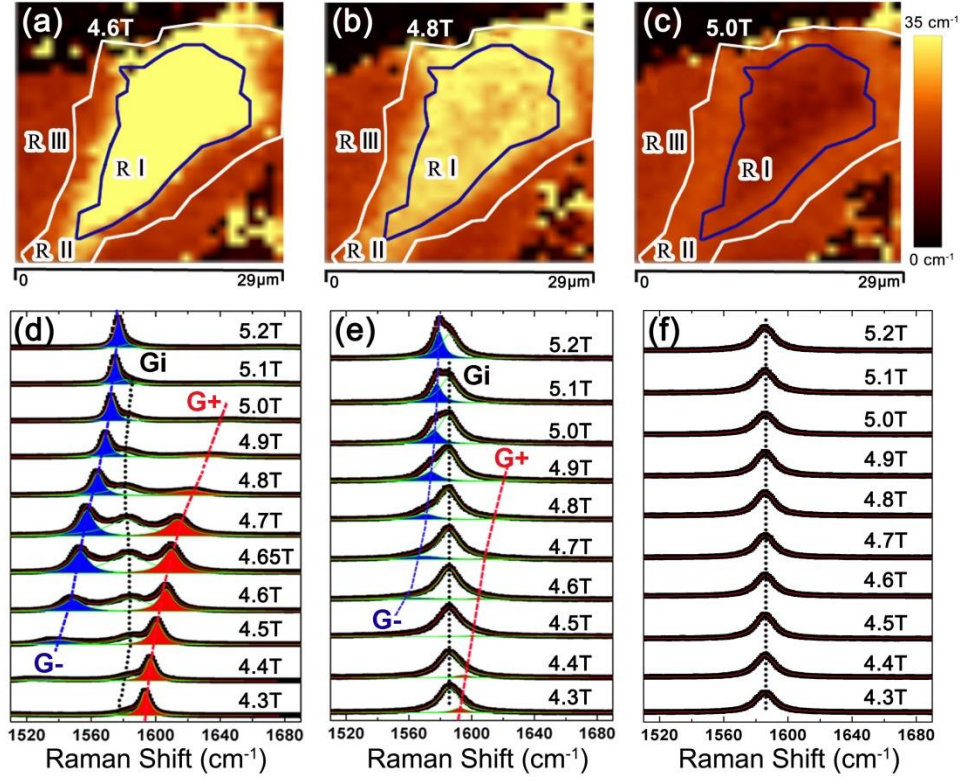


Figure 4.2. (a-c) Raman mapping images of the G band spectral width at $B = 4.6$, 4.8 and 5.0 T, respectively. The scanned sample area can be separated into three different regions (marked by “R I”, “R II” and “R III”) where the evolutions of the G peak with magnetic field are different by blue and white lines. (d-f) Typical evolutions of the Raman spectra in the range from 4.3 T to 5.2 T in regions of R I (d), R II (e) and R III (f). Dashed lines in (d-f) are guides to the eyes.

Figure 4.1 shows several exfoliated graphite samples which have been measured for the magnetic field dependence of the G phonon mode. Graphite samples were

quickly examined for MPR by Raman mapping at $B = 4.8$ T. In this chapter, the sample locates inside the solid ellipse in Figure 4.1a is regarded as a representative sample for MPR study. Note that obtained experimental results can be well reproduced in other samples. Figure 4.2(a-c) shows Raman mapping images of the G band spectral width from the surface of this selected graphite at $B = 4.6, 4.8$ and 5.0 T, respectively. According to the colour contrast, we distinguished this area into three regions where three kinds of distinctive behaviours in the G band were found. Boundaries of these regions are drawn by blue and white lines.

Figure 4.2(d-f) presents Raman spectra as a function of magnetic field in the range from 4.3 T to 5.2 T in R I, R II and R III. The evolution of the Raman spectra in this range can be explained by the interaction between G phonons and Landau level transitions (from $n = -2$ to 1 or from $n = -1$ to 2 , denoted by $L_{-2,1}^{-1,2}$). As shown in Figure 4.2d, the Raman spectrum at 4.65 T can be clearly fitted by three Lorentzian peaks. Raman spectra are analysed and three peaks are labelled with G_- , G_i and G_+ . The relative weak energy peak (G_- mode) locates at about 1520 cm^{-1} at 4.3 T evolves like a satellite and gradually blue shifts and increases its intensity when it is close to the resonant magnetic field of 4.65 T. When the magnetic field is larger than 4.65 T, the G_+ mode begins to move away from the G_i mode and exhibits a rapid decrease in intensity. In another region outside the black line and inside the white line ("R II", Figure 4.2e), the G_+ mode is weak in intensity and shows like a shoulder-like subpeak with a big spectral width while the G_- mode is strong in intensity and has

clear mixing with the G_i mode when the magnetic field is larger than 4.8 T. On the other hand, in R III (Figure 4.2f), the G peak does not present obvious changes within 0 T to 9 T which is consistent with the earlier report [37]. The degrees of MPR can be evaluated by the different maximum G band widths at 4.6 T: $\sim 85 \text{ cm}^{-1}$ for R I, $\sim 70 \text{ cm}^{-1}$ for R II, and $\sim 14 \text{ cm}^{-1}$ for R III.

4.2.3 Assignment of Raman active LL transitions under magnetic field

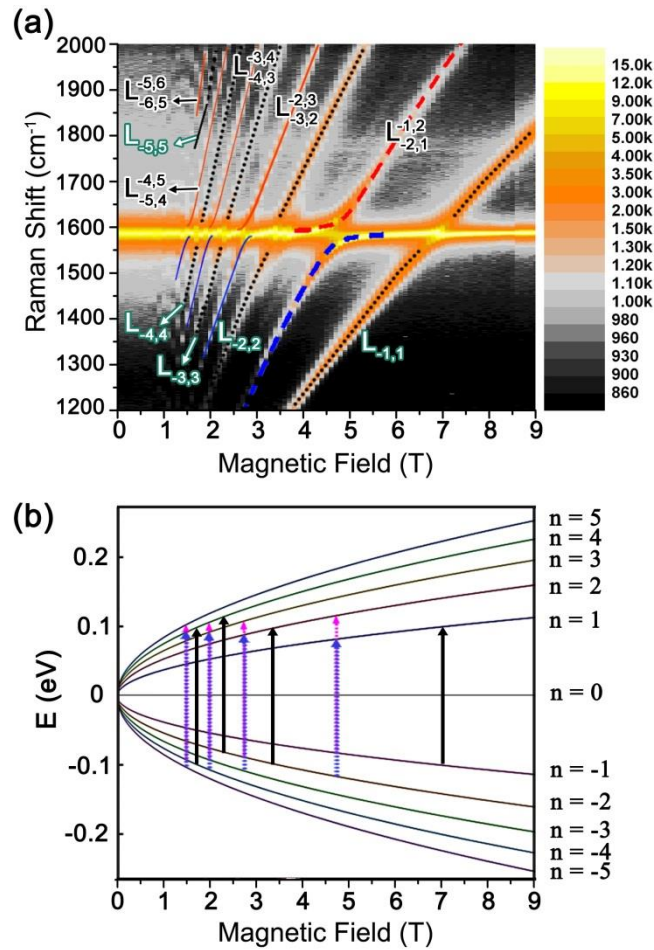


Figure 4.3. (a) Colour scale map of the Raman shift intensities as a function of magnetic field measured from sample region R I. In (a): black dotted lines represent

the symmetric LL excitations $L_{-n,n}$ (from $-n$ to n); Red and blue lines stand for the asymmetric LL transitions $L_{-(n+1),n}^{-n,n+1}$. The red and blue dashed lines around 4.7 T are simulation results as discussed below. (b) The schematic diagram of the discrete Landau energies as a function of magnetic field for monolayer graphene. Vertical lines indicate pairs of LL transitions that can resonant with the G-band phonon possessing the energy of 0.196 eV. The $L_{-(n+1),n}^{-n,n+1}$ transitions include red dashed and blue dashed lines represent the transitions from $-n$ to $n+1$ (corresponding to the cross-circular polarization configuration σ^+/σ^-) and from $-(n+1)$ to n (corresponding to the cross-circular polarization configuration σ^-/σ^+), respectively. And the black lines stand for the $L_{-n,n}$ transitions (corresponding to the co-circular polarization configurations σ^-/σ^- and σ^+/σ^+).

In Figure 4.3a, the magneto-Raman spectra intensities as a function of magnetic field are plotted for the results measured from region R I. In the false colour image, a clear horizontal line (yellow colour) locates around 1580 cm^{-1} stands for the G band phonon. Eight traces which cross the horizontal line can be assigned to different LL transitions in monolayer graphene.

First of all, we consider the origin of those magnetic field dependent traces shown in Figure 4.3a. Following the understanding in Ref. [35], these crossing traces are assigned as the inter-LL transitions of Dirac fermions and including two different kinds of series (Figure 4.3b). One of the series is the $L_{-n,n}$ series (dotted black lines

in Figure 4.3a) are attributed to the symmetric inter-LL transitions from $-n$ to n . According to the Raman selection rule, they can be measured by using the co-circular polarization configurations (σ^-/σ^- and σ^+/σ^+) as excitation/detection light. These purely electronic excitations are anticipated to be the most pronounced Raman active inter-LL features [35]. On the other hand, the other $L_{-(n+1),n}^{-n,n+1}$ series (red and blue lines in Figure 4.3a) are originating from the asymmetric transitions corresponding to cross-circular polarization configurations (σ^-/σ^+ and σ^+/σ^-), which contribute to the obvious MPR effect emphasized in this chapter. The observed most pronounced MPR, caused by the $L_{-2,1}^{-1,2}$ transition about 4.65 T, will be discussed in detail later in this chapter, and the simulated curves according to theory are plotted as the blue and red dashed lines for the G_- and G_+ modes, respectively. What's more, two traces which cross the G phonon band at magnetic fields as low as 1.5 and 1.7 T have been observed here and assigned to be the LL transitions $L_{-5,4}^{-4,5}$ and $L_{-4,4}$, respectively. For this assignment, by comparing the calculated resonant magnetic fields and observed results (Table 1), traces of different LL transitions cross the G line can be well assigned. When observed crossing magnetic fields B_r agree with the calculated resonant magnetic field values, the Fermi velocity v_F in this sample can be extracted to be $(1.04 \pm 0.01) \times 10^6$ m/s.

In Table 1, all the resonant magnetic fields B for the 8 different transitions calculated in this chapter are in excellent agreement with the observed values for the resonant magnetic field for this graphitic flake. These LL crossings at resonance fields are the main subject of this chapter. The resonance field values for all of the eight LL crossings shown in Figure 4.3 can be extracted. The detailed derivation processes of the resonance magnetic fields for these 8 crossings are shown below.

Table 1. The extracted resonance fields B_r compared with the calculated values

No.	1	2	3	4	5	6	7	8
Observed	1.50 T	1.70 T	2.00 T	2.30 T	2.70 T	3.40 T	4.65 T	7.00 T
Calculated	1.51 T	1.70 T	1.95 T	2.26 T	2.74 T	3.40 T	4.65 T	6.79 T
LL	-5→4		-4→3		-3→2		-2→1	
		-4→4		-3→3		-2→2		-1→1
Transitions	-4→5		-3→4		-2→3		-1→2	

Charged particles would move in cyclotron orbitals when they are in magnetic fields. Thus, those charged particles can only occupy orbits with discrete energy levels which are called Landau levels for two dimensional electron systems [4, 14, 24]. For massless Dirac-like electrons in monolayer graphene, the energy of LL (see

Figure 4.3b and Figure 1.8a) depends is proportional with magnetic field as \sqrt{B} , and the square root of Landau index “ n ” as:

$$E_n = \text{sign}(n) \sqrt{2n} \frac{\hbar v_F}{l_B} \quad (4.1)$$

where v_F is the Fermi velocity for the sample, and $l_B = \left(\frac{\hbar c}{B|e|} \right)^{1/2} = \frac{25.66}{\sqrt{B}} \text{ nm}$ is the magnetic length.

The electron-phonon coupling under magnetic fields results in a series of discrete Raman features, which relate to the resonances we observed. When the energy of an optically active inter-LL transition (magnetoexciton) is tuned to be equal with the E_{2g} optical phonon energy at a certain magnetic field, the resonant coupling will be strongly enhanced. This resonant coupling is named as magnetophonon resonance. Therefore, the resonant magnetic fields need to satisfy the MPR condition that the energy of properly selected LL transitions of Dirac fermions is the same as the energy of the G phonon (about 196 meV in our sample).

Concerning the selection rule which should satisfy the momentum conservation, two series of magnetoexcitations are able to be detected by Raman spectroscopy: $L_{-(n+1),n}^{-n,n+1}$ with $\Delta|n| = \pm 1$ (optical-like magnetoexcitations, corresponding to right and left hand circular polarization) and $L_{-n,n}$ with $\Delta|n| = 0$. At resonance, we have:

$$\text{For } L_{-(n+1),n}^{-n,n+1}, \Delta E_n = (\sqrt{n} + \sqrt{n+1}) \sqrt{2} \hbar v_F \left(\frac{\sqrt{B}}{25.66} \text{ nm} \right) = 196 \text{ meV}, \quad (4.2)$$

$$\text{For } L_{-n,n}, \Delta E_n = (2\sqrt{n})\sqrt{2}\hbar v_F \left(\frac{\sqrt{B}}{25.66} nm \right) = 196 meV. \quad (4.3)$$

where, B is a dimensionless value and the value of B is using the units of Tesla (T). For a given n, the resonant magnetic field can be extracted according to Equations. (4.1) and (4.2). It also determines the Fermi velocity v_F to be $(1.04 \pm 0.01) \times 10^6$ m/s by the simulation work based on the observed B_r values.

4.2.4 Two coupled mode fitting for the MPR

There will be strong coupling between phonon and electronic excitations when MPR happens. Thus, it is necessary to adopt a coupled mode theory to analyze the phonon and electronic excitations. Broadening parameters for phonon and electronic excitations are introduced in this model. We will quantitatively analyse the G_+ and G_- modes based on the two coupled mode model which is proposed by Goerbig *et al.* [34] and Yan *et al.* [37]. In the two coupled mode, the G_+ and G_- features are proposed to be due to the interaction between the G mode phonon and the LL transition and can be described by following formula [37]:

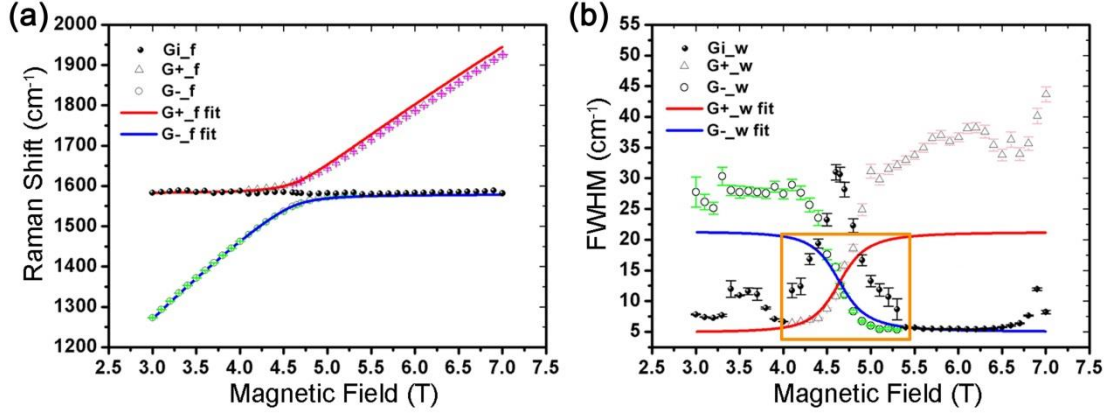


Figure 4.4. The theoretical fittings for (a) the frequency and (b) the full-width-at-half-maximum (FWHM) measured based on the two coupled mode model by using constant γ_Ω [Equation (4.9) shown below]. The red branch represents the G_+ mode and the blue branch corresponds to the G_- mode. The experimental data points of the G_i mode are also shown as black dots here. When the magnetic field is in the MPR region and for the coupled modes with strong intensities, the simulated curves match well with the experimental data points.

$$\tilde{\omega}_\pm(B) = \frac{\omega_G + \Omega(B)}{2} + i \frac{\gamma_G + \gamma_\Omega}{2} \pm \sqrt{\left(\frac{\omega_G - \Omega(B) + i(\gamma_G - \gamma_\Omega)}{2} \right)^2 + g(B)^2}, \quad (4.4)$$

Where, the real and the imaginary parts of $\tilde{\omega}_\pm$ denote the energy and the half width at half maximum intensity of these two modes, respectively. ω_G and $\Omega(B)$ stand for the energies of the G mode phonon and the LL transition. Here, γ_G and γ_Ω represent the broadening parameters for the half widths of the G phonon and the LL

transition, respectively. And $g(B)$ is the magnetic field dependent coupling strength, which is proportional to \sqrt{B} , we can write that $g(B) = c\sqrt{B}$.

We can obtain all the parameters at $B = B_r$, determined by the measured experimental data (see details in later discussion). The derived values for this studied sample are: the G phonon width $\gamma_G = 2.5 \text{ cm}^{-1}$, the LL transition width $\gamma_\Omega(B_r) = 10.6 \text{ cm}^{-1}$ ($\sim 1.3 \text{ meV}$), a constant coefficient $c = 13.27 \text{ cm}^{-1}/\text{T}^{1/2}$, and the coupling strength $g(B_r) = 28.6 \text{ cm}^{-1}$.

Table 2 lists these extracted parameters like the Fermi velocity v_F obtained from previous research works. The value obtained here for γ_Ω is much smaller than previous values (26 cm^{-1}) [36, 37], which is also discussed in the introduction. The characteristic scattering time $\tau = \hbar / \gamma_\Omega$ given by uncertainty relationship yields $\tau = 0.46 \text{ ps}$. This scattering time is comparable to and larger than the value obtained in earlier report (0.4 ps) measured by STS measurements [86]. Because the LL broadening γ_Ω is related to the disorder, the narrow spectral width derived here implies that a high quality graphene on graphite sample was used in our measurements.

Table 2. Parameters derived by us compared with previous reported works

Technique & Ref.	Sample type	v_F (10^6 m/s)	Coupling strength	γ_G (cm^{-1})	γ_Ω	τ (fs)
---------------------	-------------	---------------------------------	----------------------	------------------------------------	-----------------	----------------

*Major part of this chapter is adapted from Qiu, C. * ; Shen, X. * et al., Phys. Rev. B 2013, 88, 165407.*

		/s)	g	(cm^{-1})	(cm^{-1})	
B-Raman, this work	Graphene on graphite	1.04	28.6	2.5	10.6 @4.65T	460
B-Raman, Yan <i>et al.</i> (Ref. 37)	Graphene on graphite	1.03	37	2	26 @4.7T	200
B-Raman, Faugeras <i>et al.</i> (Ref. 36)	Epitaxial graphene (~70 layers)	1.02	26	2	90 Constant	54
B-Infrared, P. Kim <i>et al.</i> (Ref. 82)	Monolayer graphene	1.18	N.A.	N.A.	161 @6.3T	30
B-Infrared, Faugeras <i>et al.</i> (Ref. 83)	Epitaxial graphene (~100 layers)	1.02	N.A.	N.A.	80 @4T	60
B-STs, Li <i>et al.</i> (Ref. 40)	Graphene on graphite	0.79	N.A.	N.A.	32.3 @4T	150
B-STs, Miller <i>et al.</i> (Ref. 85)	Epitaxial graphene (~10 layers)	1.13	N.A.	N.A.	12.1 @5T	400

Figure 4.4a and Figure 4.4b show that good agreement between the simulated results and the experimental measured values can be achieved for both the phonon energy and the FWHM for these two coupled modes with strong intensities when the magnetic field is in the MPR region. Here we can acquire $\tilde{\omega}_{\pm}$ as a function of B when using a constant value of $\gamma_{\Omega}(B_r)$ [see Equation (4.9) in later discussion] by substituting all the determined parameters into Equation (4.4). However, it is noted that the model does not fit the data well when the magnetic field is away from resonance. This indicates that the two coupled mode model is only reasonable at the resonance region, and gets to be a worse and worse approximation away from resonance. This disagreement away from resonance could be due to other resonances which will give a significant contribution to the electron–phonon coupling.

Now let's see the detailed derivations for the parameters from the two coupled mode model. When it is at the resonance magnetic field B_r , where it satisfies that $\omega_G = \Omega(B_r)$, Equation (4.4) is simplified as:

$$\tilde{\omega}_{\pm}(B_r) = \omega_G + i \frac{\gamma_G + \gamma_{\Omega}}{2} \pm \sqrt{g(B_r)^2 - \left(\frac{\gamma_G - \gamma_{\Omega}}{2} \right)^2}. \quad (4.5)$$

From this equation indicates, at $B = B_r$, we can know that $\tilde{\omega}_{+}$ and $\tilde{\omega}_{-}$ should have an equal-weighted superposition of the phonon and the magnetoexciton. Thus, the G_{+} and G_{-} coupled modes could have the same “full width at half maximum”

$\gamma_G + \gamma_\Omega$, and the frequency difference between G_+ and G_- modes is

$$2\sqrt{g(B_r)^2 - \left(\frac{\gamma_G - \gamma_\Omega}{2}\right)^2}.$$

Table 3 shows the extracted parameters from experimental measured Raman spectra. Since that the resonant B field is around 4.65 T, we can calculate the energy splitting and the width of the two coupled modes at resonance by averaging the measured parameters at 4.6, 4.65 and 4.7 T.

Table 3. Parameters of the Raman spectra measured at $B = 4.6, 4.65$ and 4.7 T in region R I. Frequencies and FWHMs are expressed in units of cm^{-1} .

Magnetic Field		ω_+	ω_-	$\omega_+ - \omega_-$
4.6 T	Peak Position (cm^{-1})	1606.35	1548.82	57.53
	FWHM (cm^{-1})	10.78	15.55	
4.65 T	Peak Position (cm^{-1})	1609.68	1553.30	56.38
	FWHM (cm^{-1})	12.84	12.50	
4.7 T	Peak Position (cm^{-1})	1613.43	1557.39	56.04
	FWHM (cm^{-1})	15.79	11.00	

By averaging all the FWHM values, we get: $\gamma_G + \gamma_\Omega = 13.08 \text{ cm}^{-1}$.

By averaging all the frequency difference at 4.6, 4.65 and 4.7 T, we can get:

$$2\sqrt{g(B_r)^2 - \left(\frac{\gamma_G - \gamma_\Omega}{2}\right)^2} = 56.65 \text{ cm}^{-1}. \quad (4.6)$$

By averaging all the G mode frequencies for G_+ , G_- , we get $\omega_G = 1581.50 \text{ cm}^{-1}$.

The LLs are discrete when the graphene is under large magnetic field. The G mode line width is anticipated to become small because of the much reduced electron and phonon coupling under large magnetic field. The smallest value of G band width is $\sim 4.95 \text{ cm}^{-1}$ at 9 T in the experiment in Figure 4.6b, which corresponds to $2\gamma_G$. Hence, $\gamma_G = 4.95 \text{ cm}^{-1}/2 = 2.47 \text{ cm}^{-1}$. Therefore, the LL transition half width at resonance: $\gamma_\Omega(B_r) = 10.61 \text{ cm}^{-1}$. According to these two values and Equation (4.6), we can know that, at resonance, $g(B_r) = 28.62 \text{ cm}^{-1} = c * \sqrt{4.65T}$, $c = 13.27 \text{ cm}^{-1}/\text{T}^{1/2}$. So,

$$g(B) = 13.27 * \sqrt{B}. \quad (4.7)$$

And for the energy of the LL transition $L_{-2,1}^{-1,2}$, which is described by “ $\Omega_{-2,1}^{-1,2}$ ”, we get the expression:

$$\Omega_{-2,1}^{-1,2} = (\sqrt{1} + \sqrt{2})\sqrt{2}\hbar v_F \left(\frac{\sqrt{B}}{25.66} \text{ nm}\right) = (733.92\sqrt{B}) \text{ cm}^{-1}. \quad (v_F = 1.04 \times 10^6 \text{ m/s}) \quad (4.8)$$

Substituting the determined values and the Equations (4.7) and (4.8) written above into Equation (4.4), then we can be able to fit the frequency/widths at various magnetic fields by using the real/imaginary part of:

$$\omega_{\pm} = \frac{1581.50 + 733.92\sqrt{B}}{2} + \frac{10.61 + 2.47i}{2} \pm \sqrt{\left[\frac{(733.92\sqrt{B} - 1581.50) + (10.61 - 2.47)i}{2}\right]^2 + (13.27\sqrt{B})^2} \text{ cm}^{-1}. \quad (4.9)$$

What's more, similar theoretical simulation work is done to calculate the related parameters in R II. The value of FWHM of the LL transition is extracted to be 21.3 cm^{-1} (about 2.6 meV) and the coupling strength is 21.2 cm^{-1} . Hence, it is speculated that the weak MPR effect in R II should be due to the small coupling strength and especially the broad LL width.

4.2.5 Two coupled mode fitting with magnetic field dependent LL width

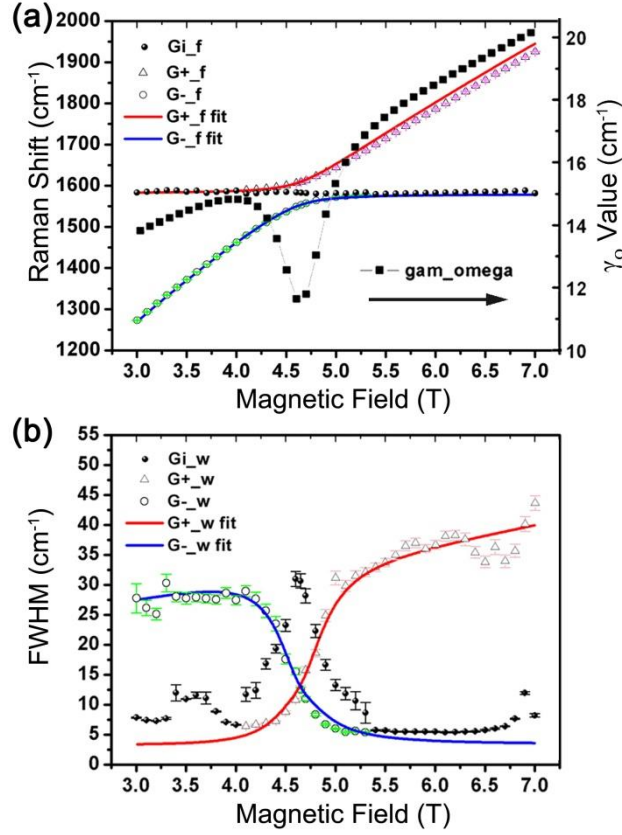


Figure 4.5. The theoretical simulations by the two coupled mode model using a B -dependent γ_G for (a) the frequency $\tilde{\omega}_\pm$ in Equation (4.4) and (b) the FWHM of the G_+ and G_- modes. γ_G values under various B used to fit the model for our measured results are presented in (a). The red curve represents the G_+ mode while the blue curve corresponds to the G_- mode. The error bars for the G_+ mode are in pink colour and for the G_- mode they are in green colour. Values for the G_i mode are indicated by black dots.

In previous infrared transmission experiments, it is reported that the LL spectral width in graphene indeed varies with the magnetic field [84]. To improve the

simulation for the off-resonance region and to offer an empirical set of parameters which works over a wide magnetic field range, the γ_G as a function of magnetic field B is adjusted based on an ad-hoc functional form:

$$\gamma_{\Omega}(B) = G_o(1 + \frac{1}{A(B - B_r)^2 + A_1})^{-1} + A_2(B - B_r). \quad (4.10)$$

The first term of Equation (4.10) based on the fact that the sum of the line widths for $\tilde{\omega}_+$ and $\tilde{\omega}_-$ is at minimum when $B = B_r = 4.65$ T in the experiment. The second term of the B dependence of γ_{Ω} shown in Equation (4.10) is another magnetic field dependence of the line width of the intrinsic LL transition, which would drop off at $B = B_r$. Substituting the expression for $\gamma_{\Omega}(B)$ shown in Equation (4.10), and defining γ_G to be a constant, the real/imaginary parts of $\tilde{\omega}_{\pm}(B)$ thus have those fitting parameters: G_o , A , A_1 , A_2 and γ_G .

Figure 4.5a and 5b show that, both the band frequencies and FWHMs, respectively, the G_+ and G_- modes over the larger magnetic field range from 3 to 7 T can be simulated very well by using Equation (4.10). The used parameters for the experimental results are: $G_o = 16.5 \text{ cm}^{-1}$, $A = 50.0$, $A_1 = 2.3$, $A_2 = 1.6$ and $\gamma_G = 1.6 \text{ cm}^{-1}$. $\gamma_{\Omega}(B)$ (solid squares) is at a minimum γ_{Ω} value when $B = B_r$ using the right side scale. According to this specified model, the G-mode phonon half spectral width γ_G is obtained to be 1.6 cm^{-1} (means that FWHM is 3.2 cm^{-1}) and the half width of LL transition at resonance is found to be 11.5 cm^{-1} (about 1.4 meV). It should be pointed out that the extracted γ_G does not mean the line width of the G

mode for the off-resonance region when B is about 3 T or 7 T in Figure 4.5b where the FWHM value is about $(7.8 \pm 0.5) \text{ cm}^{-1}$. The reason for this difference may be due to the fact that other LL transitions are also crossing the G phonon band when B is about 3 T or 7 T (see Figure 4.3a), which makes the line width of the G phonon broad.

In fact, the imaginary part (spectral width) of the self-energy for the G-band phonon becomes a maximum at $B = B_r$ in T. Ando's calculation [33]. Although the behaviour of $\tilde{\omega}_+$ and $\tilde{\omega}_-$ is able to be explained based on the self-energy simulation [33], both $\tilde{\omega}_+$ and $\tilde{\omega}_-$ appear in the resonance region around $B = B_r$ which for a given B cannot be interpreted. Therefore, the two coupled mode model is adopted and modified γ_Ω to describe the measured results in a broader B region is applied in the model. In this two coupled mode model, two peaks come out when $B = B_r$ and the line width of those $\tilde{\omega}_+$ or $\tilde{\omega}_-$ are defined. If it is needed to compare the line width of the two coupled modes model with that of the self-energy, the width of the whole peak profile of the G phonon should be measured, or alternatively read the frequency splitting between G_+ and G_- by $\tilde{\omega}_+ - \tilde{\omega}_-$ as the line width of the G phonon, which shows a maximum value at $B = B_r$, thus demonstrating mutual agreement between the two theoretical models.

It is also found that γ_Ω exhibits a minimum value when $B = B_r$. This is somehow unexpected because that we believe that the lifetime of the magnetoexciton would be shorter at $B = B_r$ as it is for the G mode phonon. To study the physical nature of

Equation (4.10), further investigations are needed, which should be a problem to be considered in future. Nevertheless, this field-dependent γ_Ω indicates that other effects may need to be taken into account in the “two coupled mode model” and such efforts should stimulate new fundamental physics regarding the understanding of the phonon-magnetoexcitons interaction.

4.2.6 Summary of rich Raman features of graphene under magnetic field

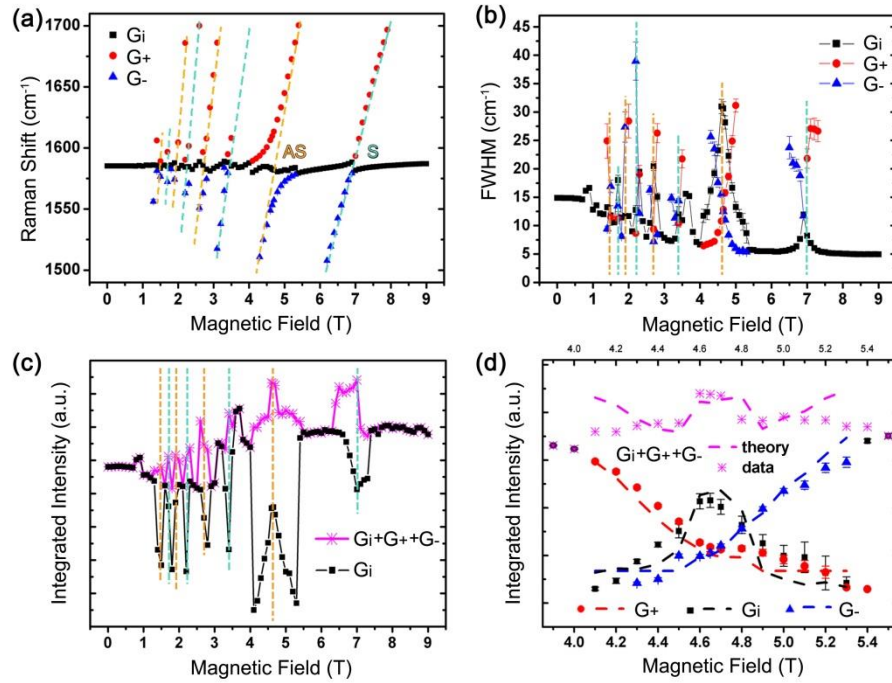


Figure 4.6 The detailed evolutions of the measured (a) frequency and (b) FWHM of the G band phonon as a function of the B field, including the middle G_i mode (black squares) and those two coupled G_+ (red dots) and G_- (blue triangles) modes. Labels S and AS define symmetric $L_{-n,n}$ (cyan dash lines) and asymmetric $L_{-(n+1),n}^{-n,n+1}$ LL transitions (orange dash lines), respectively. (c) The sum of the intensities (indicated by pink stars) of the three G bands, and the individual intensity variation of

the G_i mode (black squares) as a function of magnetic field. Dashed lines are guides to the eyes. (d) The enlarged view of the sum and intensity evolution of the three G modes around the certain MPR magnetic field range. The dashed lines are theoretical simulation results which are shown in Equation (4.13), as presented below.

Let's now briefly discuss the overall spectral features of the Raman spectrum from R I in the close vicinity of the G mode phonon energy (1580 cm^{-1}), and the focus is mainly on the phenomenon at each $B = B_r$. First of all, the energy values of the three G modes (G_- , G_i , G_+) shown in Figure 4.6 display a series of anti-crossing phenomena between G_+ and G_- where the MPR happens. Not only in the main MPR region close to $B_r = 4.65 \text{ T}$, the coexistence of the three split modes can also be found at each MPR region for those asymmetric LL transitions in a magnetic field range from 1.5 T to 4.65 T. Furthermore, the interaction of the G phonon with the $L_{-n,n}$ (symmetric, S) LL transitions is weaker compared to the $L_{-(n+1),n}^{-n,n+1}$ (asymmetric, AS) LL transitions, presenting a less distinct avoided crossing near the resonant magnetic field B value. This can be understood that the $L_{-(n+1),n}^{-n,n+1}$ transitions have the symmetry of the representation E_2 , and the $L_{-n,n}$ transitions have the symmetry of the representation A_2 , allowing the former to interact with the E_{2g} optical G mode phonon stronger and thus resulting in a more effective magneto-phonon resonance coupling [35]. Secondly, at certain resonant magnetic field, those coupled modes G_+ and G_- all have the same full width at half maximum (Figure 4.6 b), which is reasonable according to two coupled mode model [37]. Thirdly, the sum of the

integrated intensities of the three G modes presented in Figure 4.6c achieves a maximum when $B = B_r$. Both the phonon generation and the LL transitions (electronic excitations) contribute to the Raman intensity when $B = B_r$. Thus, the sum of Raman intensities reaches a maximum, because that the energy denominator for the time dependent perturbation for the two processes show a minimum at resonance, although the contribution of G_+ or G_- to the sum of intensities does not display a maximum at $B = B_r$.

Attention has been paid to the variation of the G_i mode, which shows a set of quite pronounced maxima in their spectral widths at $B = B_r$ as displayed in Figure 4.6b. When the G_+ or G_- modes are close to each resonant magnetic field, the intensity of the G_i mode would drop down (Figure 4.6c). However, when we zoom into the particular evolution of the three modes near the main MPR magnetic field region, a local maximum intensity of the G_i mode just at $B = B_r$ can be found (Figure 4.6d). Considering the G_i mode energy, a slight oscillatory behaviour as a function of B is observed here.

4.2.7 Magnetic field dependent behaviour of G_i mode

The magnetic field dependent behaviour of G_i mode observed here would be considered to be unsettled issue. Thus, we would like to consider several simple questions: (1) what is the origin of G_i and (2) why is the G_i intensity increased when $B = B_r$? The oscillation of the G_i mode energy was also noticed and

interpreted in an earlier work [37], due to the co-existence of the areas in magnetic field when illuminating a large size laser spot around 80 μm in diameter, and two distinct lifetimes were probably found in that work. The G_i mode was previously explained to originate from graphene areas in which the lifetime of electron is relatively short. That understanding apparently shows not to be appropriate for our results, since the spot size of our incident laser is only 1 μm . Hence, we would like to reconsider the understanding of the G_i mode by inspecting the magnetic field dependent oscillatory behaviour of the G_i mode in a further step.

Figure 4.7 displays the variations of the G_i mode in the three different locations (R I, II and III) of graphite. In this figure, we can observe that the stronger is the magneto-phonon resonance in a given location of the sample, the larger is the amplitude of the fluctuations of G_i in both the energy and the corresponding FWHM. Particularly, in R III, the G peak of graphite exhibits almost no change under a magnetic field from 0 T to 9 T. Therefore, the relative large fluctuation of the G_i mode in Figure 4.7 is relevant to the decoupled graphene regions, where a strong MPR happens.

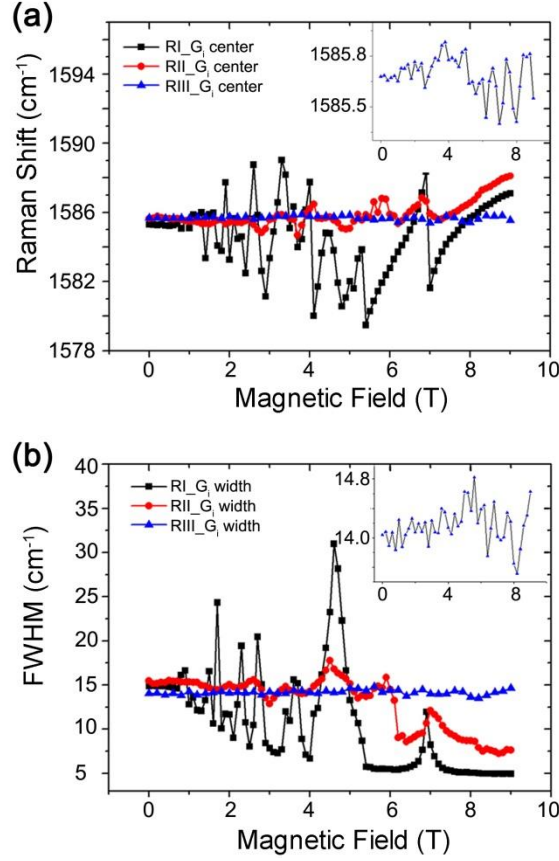


Figure 4.7. (a) G_i mode energy as a function of B field in the three representative locations on the graphite substrate. (b) Measured FWHM of the G_i modes in these three regions as a function of magnetic field. The inset is a zoom-in view of the curve measured from R III.

4.2.8 Newly proposed model for G_i mode behaviour

Here, a theoretical model is proposed by us to understand the variation of the intensity and width of the G_i mode, which can be distinguished with the G peak coming from the graphite substrate. In this model, we consider that the G phonon of graphite could be excited by many G-mode phonons from graphene by a resonance effect between the phonon of graphite and the phonon of graphene. The interaction

between G_i and those two coupled modes (G_+ and G_- of graphene) results in a fluctuation in the overall Raman intensity of the G_i mode through a driven harmonic oscillator. The Schrodinger equation for the harmonic oscillator can describe atomic vibrations which could be probe by Raman in materials. Thus, harmonic oscillator is widely adopted in Raman related research works. The fluctuation of the intensities of the G_+ and G_- modes behaves like externally applied forces with spectral functions A_ω and B_ω , respectively, in Equation (4.11), which can efficiently influence the variation behaviour of the overall G band and thus affect the amplitude and energy of the G_i phonon mode. Thus, we then express the amplitude “q” of the G band vibration using the equation as follows:

$$\ddot{q} + \gamma_{Gi} \dot{q} + \omega_0^2 q = \int a A_\omega e^{-i\omega} d\omega + \int b B_\omega e^{-i\omega} d\omega \quad (4.11)$$

where, A_ω and B_ω are, the amplitudes of the G_+ and G_- modes respectively. The parameters “a” and “b” are, respectively, induced into Equation (4.11) to describing the coupling constant between G_i and the G_+ and G_- coupled modes. And ω_0 and γ_{Gi} are, the parameters of the energy and the line width of the G_i peak respectively. Because that A_ω and B_ω are expected to have the dimensions of an amplitude, they thus can be taken into account, respectively, to be equal to the square root of the mode intensities of $I(\omega_+)$ and $I(\omega_-)$ for the G_+ and G_- modes as a function of magnetic field, by adopting the experimental mode intensities:

$$A_\omega = \sqrt{I(\omega_+)}; \quad B_\omega = \sqrt{I(\omega_-)}.$$

To solve the differential Equation (4.11) with the Fourier transform $Q = \int_{-\infty}^{+\infty} qe^{i\omega t} dt$,

we can get the equation for the amplitude of the overall G mode:

$$Q = \frac{2\pi(aA_{\omega} + bB_{\omega})}{(\omega_0^2 - \omega^2) + i\omega\gamma_{G_i}}. \quad (4.12)$$

Later, the total band intensity can be calculated by:

$$I(\omega) = |Q|^2 = \frac{4\pi^2(aA_{\omega} + bB_{\omega})^2}{(\omega_0^2 - \omega^2)^2 + \omega^2\gamma_{G_i}^2}. \quad (4.13)$$

4.2.9 Simulation results based on the proposed model

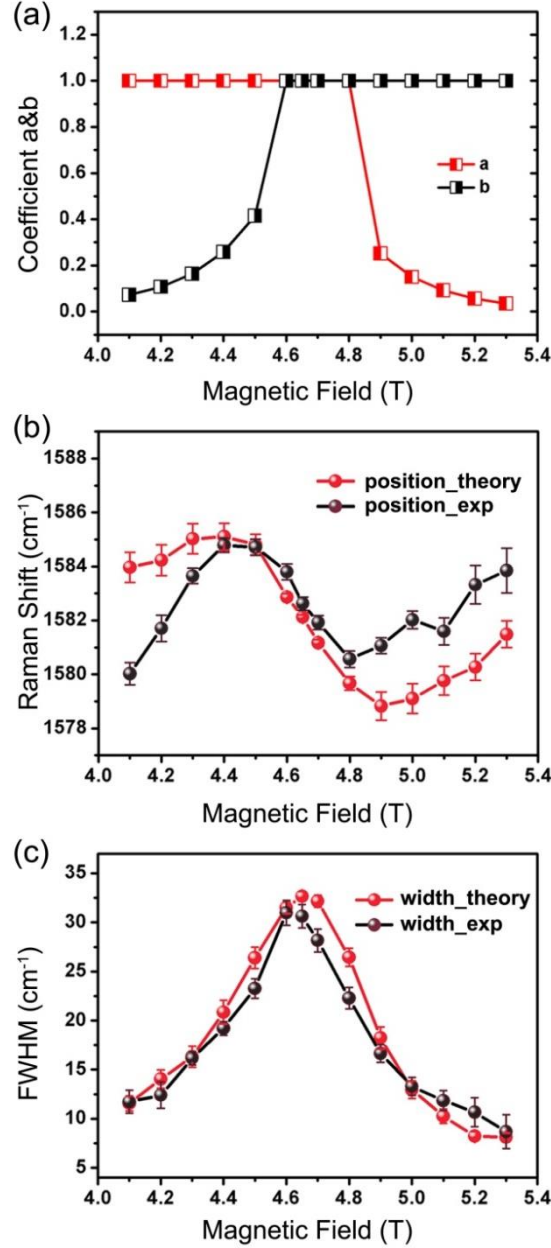


Figure 4.8. (a) The parameters a and b in Equation (4.13) used for the simulation of $I(\omega)$ as a function of magnetic field. (b) The measured Raman energy and (c) the measured FWHM of the middle Lorentzian component of the simulated $I(\omega)$ curve by

Equation (4.13) (red spheres) and the corresponding values of the measured G_i (black spheres) as a function of the magnetic B field.

Let us fit the parameters a , b , ω_0 and γ_{Gi} according to experimental results in the pronounced MPR region near $B_r = 4.65$ T. In Figure 4.5a, we can find that: near the MPR region, when the magnetic field is away from B_r , the absolute value of the energy difference between the G_+ mode (ω_+) and the averaged G_i mode ($\bar{\omega}_i \approx 1582 \text{ cm}^{-1}$) is inversely proportional to the absolute value of the energy difference between the G_- mode (ω_-) and $\bar{\omega}_i$. On the contrary, for magnetic fields around the resonance point, the energy differences between these modes are almost the same. We suppose that the driving forces exerted by the G_+/G_- modes are in association with the energy difference from the average frequency of the G_i mode. Hence, for the magnetic fields in the range $B = 4.6\text{-}4.8$ T which are near the MPR, because that $|\omega_+ - \bar{\omega}_i| = |\omega_- - \bar{\omega}_i|$, we make $a = b = 1$. When it is away from the MPR point, for smaller values of the magnetic field $B < 4.6$ T, we let $a = 1$, $b = \frac{|\omega_+ - \bar{\omega}_i|}{|\omega_- - \bar{\omega}_i|}$. On the contrary, for larger magnetic fields $B > 4.8$ T, $a = \frac{|\omega_- - \bar{\omega}_i|}{|\omega_+ - \bar{\omega}_i|}$, $b = 1$.

Figure 4.8a presents the resulting variation of a and b as a function of magnetic field. Therefore, at $B_r = 4.65$ T, $a = b = 1$. Based on this formulation, the optimized simulation of $I(\omega)$ to the measured spectrum at 4.65 T follows Equation (4.13). So, ω_0 and γ_{Gi} are finally extracted to be: $\omega_0 = 1582.0 \text{ cm}^{-1}$, $\gamma_{Gi} = 28.5 \text{ cm}^{-1}$, which

are appropriate extraction for these coefficients, also used to further verification for consistency as discussed later. At the same time, a scale parameter of $s = 6 \times 10^7$ is adopted to make $I(\omega)$ into the same order of magnitude as the measured spectrum.

In Figure 4.8b and 4.8c, simulated band energy and band line width of the measured G_i mode are compared to the experimental results. These mode spectral features of the G_i mode are able to be well regenerated by this theoretical model. In addition, we extracted the mode intensities for the simulated $I(\omega)$ curves and compared them to the measured results, including the splitting of $I(\omega)$ into three modes (G_+ , G_- and G_i) and the sum of those intensities of G_+ , G_- , G_i to the measured results, as displayed in Figure 4.6d. The main variation of these intensities is in good agreement with that acquired from the experimental Raman spectra. The appropriate simulation of the experimental results and the theory verifies the validity of this model. And the coefficients of the model thus can be obtained.

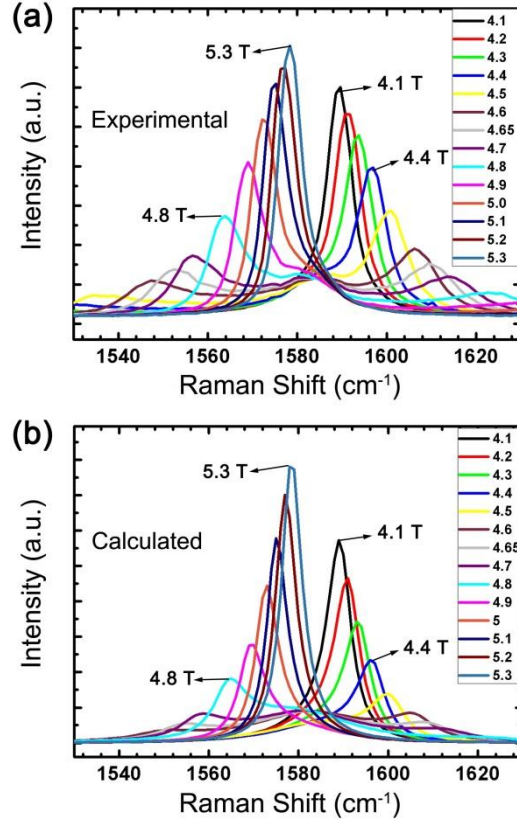


Figure 4.9. (a) Measured Raman spectra as a function of B field ranging from 4.1 to 5.3 T. (b) Simulated $I(\omega)$ curves as a function of B field in the same range as in (a). The intensities of the $I(\omega)$ curves are scaled. So, the intensity of the simulated curve at 5.3 T is the same as that of the measured Raman spectrum at 5.3 T.

Figure 4.9b presents the simulated Raman spectral $I(\omega)$ curves for various B field values from 4.1 to 5.3 T based on the coefficients fixed above. Every curve was fitted by three Lorentzian components in the fitting of the experimental Raman spectra. It is significant to notice that the highest intensities for G_+ ($B = 4.1$ T) and G_- ($B = 5.3$ T) modes are not at resonance field ($B = B_r = 4.65$ T), and this experimental observation could be explained by this current model. The overall

variation with magnetic field matches fairly well between the calculated results and the experimental findings.

The magnetoexciton mediated coupling between phonons in graphene and graphite is an original idea proposed by our work and it could be a specified observation shown only in this “graphene on graphite” system. We expect some particular optical processes to be possible between the phonons, the magnetoexcitons in graphene and the metallic energy band in graphite. And these processes could be the topic of further theoretical work, which can enrich the knowledge of the Raman mechanism in terms of the coupling among photons, phonons and electrons.

4.2.10 Surface morphology of the graphene on graphite characterized by AFM

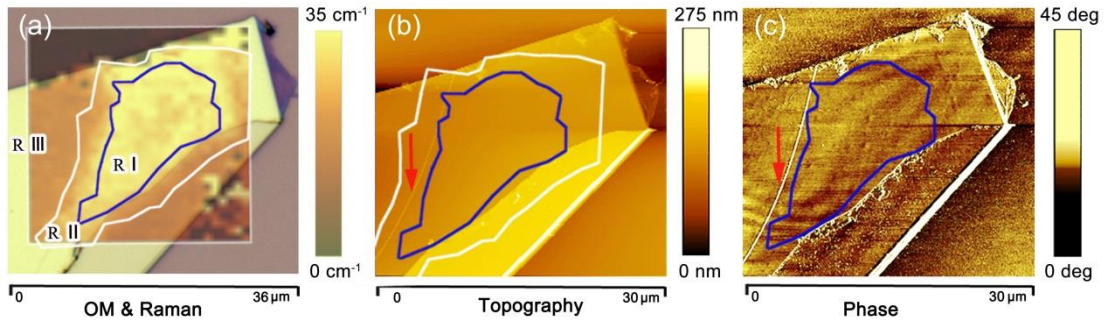


Figure 4.10. (a) Integrating the Raman image of the G band line width at $B = 4.8$ T, marking the three regions as in Figure 4.2b, with the optical microscope (OM) picture. (b) AFM topographic image and (c) AFM phase image of the measured graphite sample. A ridge like structure on the surface near the MPR region can be clearly found and instructed by the red arrows in (b) and (c). Clear contrast is shown

in (c) with a tilted pattern which is resolved in the region indicated by the blue circle in (c).

Figure 4.10b presents the AFM height image which shows clear ridge-like structures on the surface of the graphite sample close to region R I (indicated by red arrow). The successful discussion on these MPR features in terms of the massless Dirac fermion model and the two coupled mode model suggests that there is a decoupled monolayer graphene on the surface of graphite substrate. The existence of such features indicating the possible formation of so called “graphene on graphite” structures [40, 100, 101]. In epitaxial few layer graphene grown on SiC, an obvious ridge-like network of features formed from the out-of-plane distortions in the hexagonal arranged graphene lattice was found, which lead to the existence of Moiré patterns which can be clearly proved by atomically resolved scanning tunnelling microscopy [100, 101]. For natural graphite, its surface is often not homogeneous and shows all kinds of defects too. Based on low-temperature STS measurements, in the region which is separated by a macroscopic ridge-like feature, monolayer graphene pieces decoupled from the surface of highly oriented pyrolytic graphite (HOPG) have been observed. The case could be similar in our natural graphite sample or the Kish graphite reported by others [37].

Figure 4.10c presents the simultaneously obtained phase information of MPR regions on this graphite substrate, where a ridge-like feature close to region R I is also

clearly distinguished (red arrow). It has been confirmed and demonstrated by lots of earlier works that phase contrast imaging in the AC AFM mode is quite sensitive to the change of relative properties relate to the averaged value, like the mechanical (stiffness, friction) or adhesive properties [102]. For this reason, the phase imaging displayed in Fig. 4.10c could be seen as another experimental method for us to find out those decoupled graphene regions from the normal graphite parts of the sample. What's more, though certain surface contamination, stripe contrasts are acquired on the graphite sample. A stripe pattern which is tilted from the stripe pattern on graphite (R III) is clearly distinguished in the region R I indicated by the blue outline in Figure 4.10c. Both the region and orientation of the phase pattern are agreeing well with the distinguished strong MPR location R I in the corresponding Raman mapping present in Figure 4.10a. As a consequence, we believe that the changed MPR strength [Figure 4.2(d-e)] in R I and R II is related to the degree of decoupling in the graphene layers. This interpretation is appropriated considering that R II is close to both R I and R III.

4.3 Conclusions

In this chapter, we demonstrate low temperature (~ 5 K) magneto-Raman experiments on bulk graphite samples with a magnetic field (B) up to 9 T. A few “graphene on graphite” locations were identified by Raman mapping and further verified by the AFM technique. We have observed rich MPR phenomena, which are ascribed to the interaction of the G phonon and the electronic excitations between

Dirac fermion LLs. The appearance of eight obvious features is identified as electronic excitations between LLs, including one occurring at a magnetic field as low as 1.5 T. The two coupled mode model together with our newly proposed fitting model successfully interpret the main features obtained in the splitting of the G phonon into G_+ , G_- and G_i modes. The measured variation of the middle frequency mode (G_i) is regenerated by a physical model that the G-band of the graphite substrate is coupling with the G_+ and G_- modes. The narrow LL width of 10.6 cm^{-1} (about 1.3 meV) in the magnetophonon resonance offers evidence for the high quality of the decoupled graphene. The specifically high quality of the graphene layer obtained here also implies the critical effect of the substrate on the quality of the graphene samples, which could stimulate future efforts for achieving high quality graphene layers and also other 2D materials for both fundamental and application studies.

Chapter 5 Electrical field tuning of magneto-phonon resonance in monolayer graphene

5.1 Introduction and motivation

MPR effect has been investigated in a variety of two-dimensional systems [29-32, 103-107] and predicted to exist in graphene related systems. For example, the G phonon in monolayer graphene would show magnetic field dependent variation due to the coupling to the electronic magnetoexcitations [33, 34]. Especially, the inter-Landau-Level electronic transitions $LL_{-2,1}^{-1,2}$ and $LL_{-1,0}^{0,1}$ were expected to have strong coupling with the G phonons at about 5 T and 30 T [34], respectively. Here, $LL_{-n-1,n}^{-n,n+1}$ stands for the inter-LL transitions both from L_{-n-1} to L_n and from L_{-n} to L_{n+1} (L_n represents the LL with an index of n , n is integer and $n = 0, 1, 2, \dots$).

Raman spectroscopy is a widely employed technique to study various properties of graphene [17, 18, 21, 91, 96, 108-111]. Recently, the MPR effect in graphene related systems was observed through magneto-Raman (Raman spectroscopy technique in a magnetic field) by several groups [37, 38, 44, 112, 113], where the G phonons exhibit a clear magnetic dependent variation.

The Fermi level or filling factor was anticipated and observed to greatly affect the MPR effect in monolayer graphene [33, 105-107]. Potemski's work observed the magneto-phonon effect due to the coupling between the G phonons and LL_{-1}^0 in

mechanical exfoliated monolayer graphene [105]. From their results, the sample was identified to be *p*-type doped and the filling factor value is between 2 and 6 at about 25 T. However, this work only studied accidentally doped graphene samples with carrier concentrations typical for graphene deposited on Si/SiO₂ substrates. *Kim et al.* studied the MPR in adsorption doped CVD-grown monolayer graphene samples [106]. The different doping levels were obtained by adjusting annealing parameters and by the exposure to ambient pressure N₂ gas or air, which is not well tunable compared to electrically gated graphene in the sense of uniformity or controlling. Very recently, there is a comprehensive study of the electrical tuning of the fundamental MPR induced by $LL_{0,1}^{-1,0}$ excitations in CVD grown graphene [107]. Their measurements were conducted at extremely high constant magnetic fields around 25 T while sweeping the gate voltage. However, the effect of relatively high doping level on MPR under a relatively low magnetic field is still missing and needs to be investigated.

In this chapter, our work study on the MPR effect involving $LL_{-2,1}^{-1,2}$ in an electrically tuned monolayer graphene by magneto-Raman experiments. The carrier concentration in the sample was tuned by a back gate, so that the filling factor of LL under a magnetic field was altered accordingly. Consequently, responses of the G phonons of monolayer graphene to the magnetic field with different gate voltages reflect the filling factor effect on MPR. By tuning the Fermi level to reach zero/large filling factors, we clearly show that the MPR effect can be switched on/off in the magnetic fields around 4 T. Suspended exfoliated monolayer graphene which is newly

studied presents obvious MPR effect. In addition, asymmetric line-shape of the Raman G band is observed in electrically neutral graphene at low temperature and interpreted by Fano resonance.

5.2 Experimental results

5.2.1 Experimental details

Graphene samples were prepared by mechanical exfoliation from natural graphite crystals and transferred onto a 300 nm SiO₂/Si substrate [23]. Monolayer graphene flakes were identified by using both optical contrast spectroscopy and Raman spectroscopy [15, 16]. Electron beam lithography was utilized to define the geometry of electrodes, then Ti (5 nm)/Au (60 nm) were deposited to form contact electrodes [114].

The low-temperature magneto-Raman measurements were performed in a cryostat with a custom designed confocal micro-Raman spectroscopy\image system (see Figure 5.2a). A linearly polarized incident laser (Nd:YAG, 532 nm) illuminated on the sample with a ~ 1 μm beam size and a power less than 5 mW. Diameters of optical fibers for delivering laser and collecting signal are 5 μm and 50 μm , respectively. Similar to our previous experimental setup [44], both co-circular and cross-circular polarized signals can be simultaneously collected. Perpendicular magnetic field up to 9 T was generated by a superconductor magnet mounted inside the cryostat. Keithley 4200 semiconductor characterization system was used to

measure the electrical response of the graphene device and to provide a fixed gate voltage.

5.2.2 Tunable doping levels in graphene transistor under electrical field

Raman spectra of the monolayer graphene device were shown in Figure 5.1b. The Raman D peak which locates around 1350 cm^{-1} is undetectable, indicating the high quality of the sample. To tune the doping level, it is necessary to know the charge neutral point (or named Dirac point) of the graphene sample [115]. We prefer gated Raman measurement rather than the electric transport measurement to examine the NP value since Raman can reflect the local property. Gated-Raman measurements were performed (at $\sim 5\text{ K}$) by sweeping gate voltage from -40 V to 40 V and selected spectra are shown in Figure 5.1c. The frequencies and full width at half maximum of the G bands as a function of gate voltages are extracted by fitting each peak into a single Lorentz peak and plotted in Figure 5.1d. Softened G phonon can be observed at the charge neutral Dirac point due to Kohn anomaly [18, 21] and hence the NP of the sample can be determined to be at -6 V .

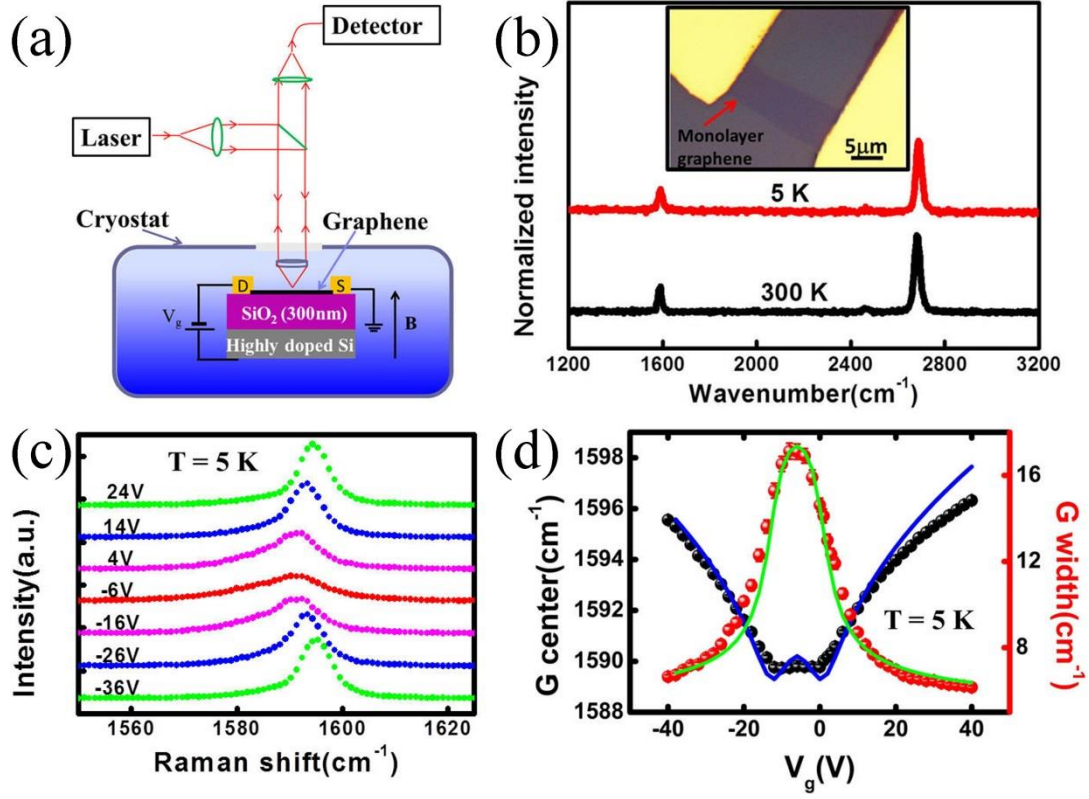


Figure 5.1. (a) A schematic for the experimental setup for the magneto-Raman measurements. (b) Raman spectra on monolayer graphene at room temperature (~ 300 K, black curve) and low temperature (~ 5 K, red curve). Inset is optical image of the graphene device. (c) Raman spectra of graphene device under various gate voltages at 5 K. The red curve ($V_g = -6$ V) corresponds to the one when the Fermi level is brought to be near Dirac point. (d) Positions (black spheres) and widths (red spheres) of the G peak as a function of the gate voltages. Simulation results are shown in blue and green lines.

Figure 5.2 shows the transport data measured from the studied device (see optical image in Figure 5.1b). Mobility of the monolayer graphene device can be extracted by the following formula [114]:

$$R_{Total} = R_{contact} + \frac{L}{We\mu\sqrt{n_0^2 + n^2}}, \quad n = \frac{C|V_g - V_{Driac}|}{e} \quad (5.1)$$

Where R_{Total} is the total resistance. L and W represent the length and width of the device, respectively. n means the carrier density and n_0 is the residual carrier concentration (from residual impurities) in the device. μ is the mobility of the device. $C = 1.15 \times 10^{-4} \text{ Fm}^{-2}$ is the capacitance for 300 nm SiO_2 . Here, the electron (or hole) mobility can be fitted to be about 9490 (or 8050) $\text{cm}^2\text{V}^{-1}\text{s}^{-1}$.

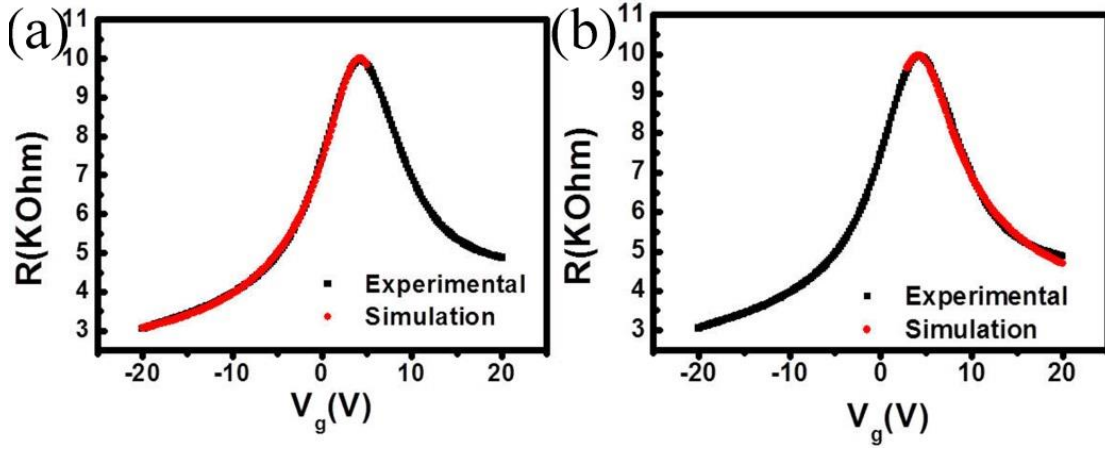


Figure 5.2. Simulation works to extract the values of mobility for electron (a) and hole (b), respectively.

5.2.3 Fano Resonance in graphene under magnetic field and electric field

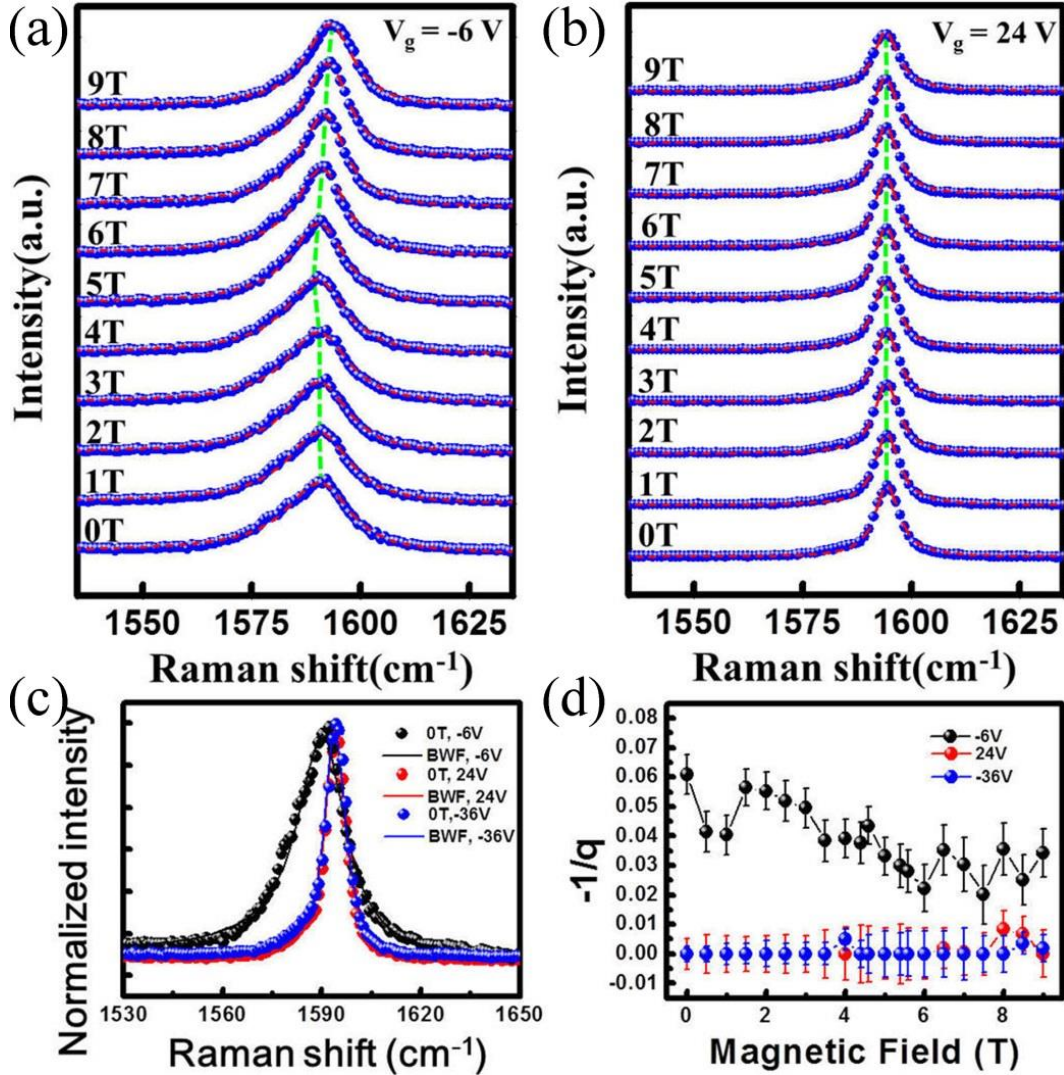


Figure 5.3. (a-b) Raman spectra of monolayer graphene at different magnetic fields measured at low temperature ($\sim 5 \text{ K}$) with back gate voltage (a) $V_g = -6 \text{ V}$ and (b) $V_g = 24 \text{ V}$ applied. Blue spheres represent raw data and red dashed lines stand for the fitting curves. Green dashed lines are guide to the eyes. (c) Comparison of the G peak line shapes for graphene sample in the cases of neutral point ($V_g = -6 \text{ V}$) and electrically doped ($V_g = 24 \text{ V}$; $V_g = -36 \text{ V}$). The solid lines are obtained by fitting the

data points to the BWF line shape using Equation (1). (d) The summarized asymmetry factor $-1/q$ for the Raman spectra taken under these three gate voltages.

Figure 5.3a and Figure 5.3b shows magneto-Raman spectra of the monolayer graphene at $V_g = -6$ V and 24 V, respectively. In all these measured spectra, the G bands show single peak profile with no obvious G peak split. However, when V_g is -6 V, asymmetric broadening at the lower-frequency side of the G band can be observed (see Figure 5.3c). Previously, G peak asymmetry/splitting was also observed and attributed to the circular dichroism effect happening only under a high magnetic field [105, 116]. However, our measured Raman G peak shows maximum asymmetry at a zero magnetic field. Thus, the asymmetric line shape presented here is most probably due to other reasons. Fano resonance between the renormalized phonon excitation and a continuum of excitonic many-body states, therefore, could be responsible and fitted by the Breit-Wigner-Fano (BWF) line shape [117, 118]:

$$I(\omega) = I_0 \frac{[1 + 2(\omega - \omega_0) / (q\Gamma)]^2}{[1 + 4(\omega - \omega_0)^2 / \Gamma^2]}, \quad (5.2)$$

where $1/|q|$ is the asymmetry factor or coupling coefficient, I_0 , ω_0 , and Γ are the intensity, uncoupled BWF peak frequency and broadening parameter, respectively. In the limit $q \rightarrow \infty$, the line shape is symmetric and shows the standard Lorentzian profile, indicating a weak interference or coupling.

Figure 5.4 presents the extracted values for $-1/q$ as a function of Fermi energy which are comparable to previous work by Yoon *et al.* [117]. Both sets of $-1/q$ data are within the range of 0.08 to 0, and vanish when the Fermi energy is large enough

(~0.2 eV for both our sample and Yoon's sample). When the graphene is either electron or hole doped to a certain extent, the values of $-1/q$ are around 0. The absence of Fano resonance in doped graphene is consistent with previous report [117] and is attributed to the suppressed excitonic processes. The fitted $-1/q$ values as a function of magnetic field under three different gate voltages are summarized in Figure 5.3d. When the Fermi level of graphene is tuned to be near Dirac point, the $-1/q$ values are all non-zero and show a maximum value at 0 T. The presence of magnetic field splits the continuum band structure of graphene into discrete Landau levels, thereby weakening Fano resonance as the magnetic field increases. Similar modification of Fano resonance by magnetic fields was reported in quantum wells [119, 120]. Note that the Fano resonance is not considered to be an important factor to affect the MPR effect in this work.

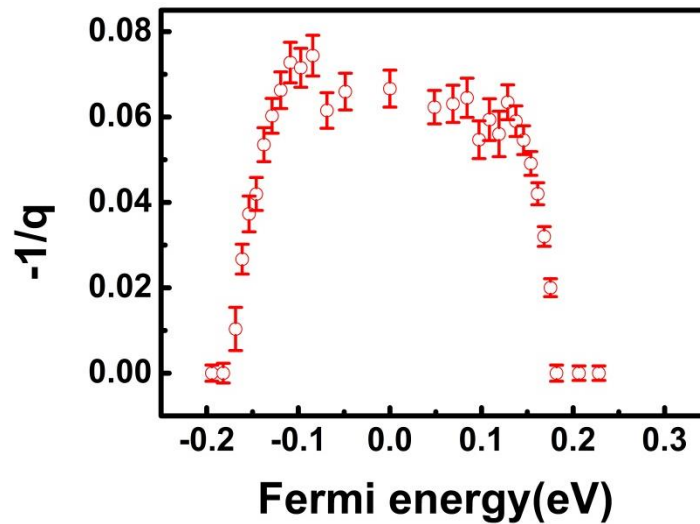


Figure 5.4. Asymmetry factor $-1/q$ as a function of Fermi energy for the graphene device (see in Figure 5.1b).

5.2.4 Tunable Raman G mode under magnetic field and electric field

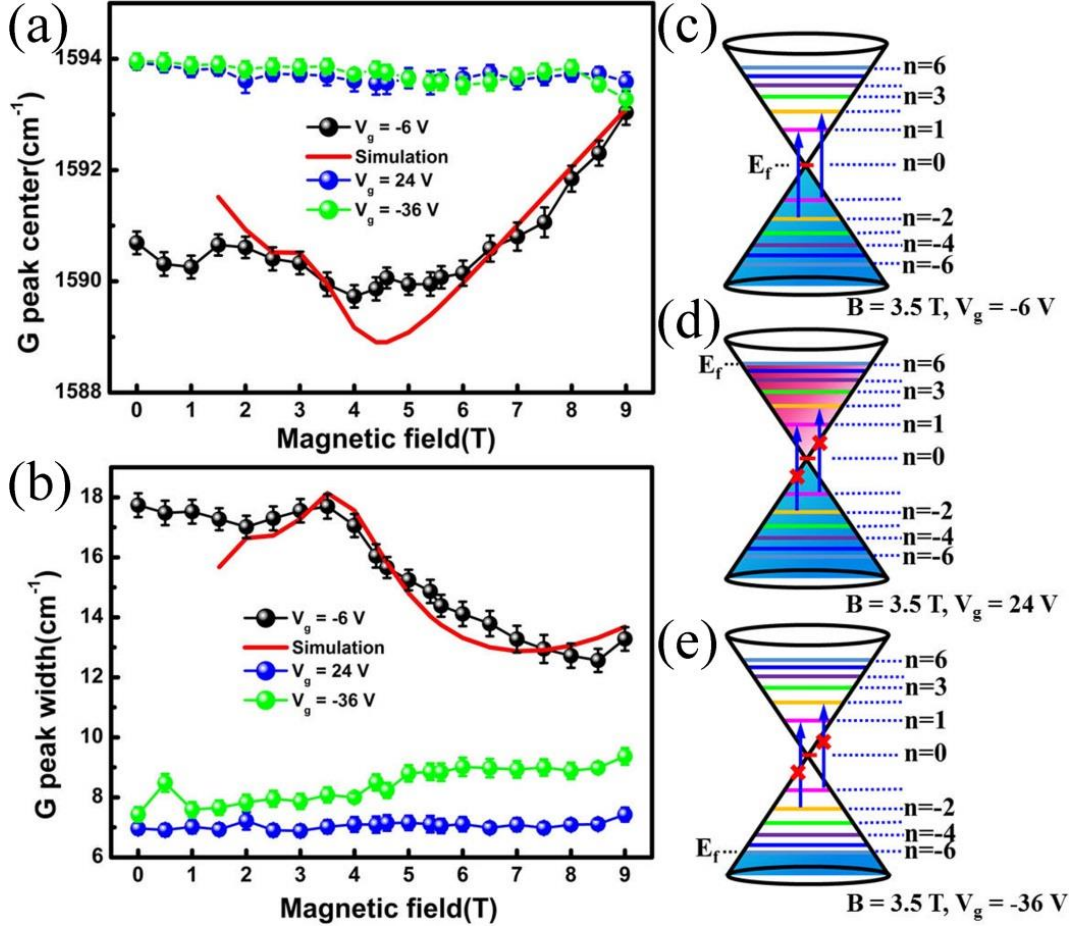


Figure 5.5. The evolutions of (a) the BWF peak frequency and (b) the width of the G peak for the monolayer graphene with magnetic field under different gate voltages. V_g values are -6 V, 24 V and -36 V for black, blue and green curves, respectively. Simulation results are also shown. (c-e) Schematic images for different doping situations in monolayer graphene when different back gate voltages are applied at $B = 3.5$ T. Discrete Landau levels are labeled with corresponding LL indexes. Fermi levels in these cases are also indicated. Vertical blue lines indicate the inter-LL transitions. (c) $V_g = -6$ V. Indicated inter-LL transitions are possible to happen in this

case. (d) $V_g = 24$ V. Indicated inter-LL transitions are suppressed in this case. (e) $V_g = -36$ V. Indicated inter-LL transitions are suppressed in this case.

Figure 5.5a and Figure 5.5b show the evolutions of the frequency and the FWHM of the G peak for the monolayer graphene with magnetic field at three different gate voltages, respectively. As shown in Figure 5.5a, it is clear that the frequency of G phonons shows a magnetic field dependent variation when V_g is -6 V. In detail, The G band frequency goes down with fluctuations before reaching its minimum value of about 1589.5 cm^{-1} at about 4 T. After this point, it keeps rising to its maximum value of about 1593.0 cm^{-1} at 9 T. For the FWHM values shown in Figure 5.5b, the maximum locates at about 3.5 T and then the FWHM value decreases with the magnetic field increases. In contrast, both the frequency and the FWHM of the G peak show weak magnetic dependence when the sample is highly *n*-type or *p*-type doped.

5.2.5 Discussions for observed experimental results

The observed results shown in Figure 5.5 could be well interpreted by the MPR theory. Discrete *LLs* appear when the graphene is subjected to a magnetic field. The energy of the *LL* with an index of *n* (E_n) is proportional to the square root of the index *n* and the magnetic field strength *B* [83, 121]: $E_n = \text{sgn}(n)\sqrt{2e\hbar V_F^2 B |n|}$. Where, V_F is the Fermi velocity. $n > 0$ and $n < 0$ represent electrons and holes, respectively. The energy of the inter-*LL* electronic excitations for $LL_{-n-1,n}^{-n,n+1}$ (which is denoted by $E_{-n-1,n}^{-n,n+1}$ here) is:

$$E_{-n-1,n}^{-n,n+1} = (\sqrt{n+1} + \sqrt{n})\sqrt{2e\hbar V_F B}. \quad (5.3)$$

MPR occurs when the energy of the inter-LL transitions is equal to the E_{2g} phonon energy at certain B field (*i.e.* the resonant magnetic field), which leads to magnetic oscillation of the G-band phonon. According to T. Ando's calculation, the spectral width would become a maximum and the frequency would be at a fast changing point at the resonant B field [33]. We therefore deduce that MPR happens at about 3.5 T and is associated with $LL_{-2,1}^{-1,2}$ transition according to our experimental data. Considering the MPR condition of $E_{-2,1}^{-1,2} = 196.8$ meV (G phonon energy is ~ 196.8 meV at 5 K without magnetic field), the Fermi velocity v_F of the sample can be calculated to be about 1.21×10^6 m/s. This v_F value is reasonable [122, 123] and agrees well with the values obtained by other reports for monolayer graphene [4, 36, 83, 121].

We have carried out the simulation work based on the prediction by Ando [33]. An equation (equation 5.4) was developed by Potemski's work [36] to analysis the magneto-phonon resonance in graphene. The same model was used here to extract the parameters.

$$\varepsilon^2 - \varepsilon_0^2 = 2\varepsilon_0\eta E_1^2 \sum_{k=0}^{\infty} \left\{ \frac{T_k}{(\tilde{\varepsilon} + i\delta)^2 - T_k^2} + \frac{1}{T_k} \right\}, \quad (5.4)$$

$$\varepsilon = \varepsilon - i\Gamma, \quad (5.5)$$

$$T_k = (\sqrt{k} + \sqrt{k+1})E_1, E_1 = \sqrt{2e\hbar V_F^2 B}, (k = 0, 1, 2, \dots), \quad (5.6)$$

where, ε_0 stands for the phonon energy at $B = 0$ T. While ε and Γ stand for the energy and width of the G phonon under magnetic field. η is the interaction strength between the G phonon and magnetoexcitations. δ stands for the broadening of the magnetoexcitations. T_k means the energy for the magnetoexcitations. V_F represents for the Fermi velocity.

By using the same model as in Potemski's work [36], we extract the following parameters: the interaction parameter $\eta = 5 \times 10^{-3}$, the broadening factor $\delta = 400 \text{ cm}^{-1} = 49.6 \text{ meV}$, the phonon energy at zero magnetic field $\varepsilon_0 = 1586.6 \text{ cm}^{-1}$, and Fermi velocity $v_F = 1.21 \times 10^6 \text{ m}^2 / \text{s}$. These values are comparable to earlier reports [36, 105, 113, 116]. Though the detailed field-dependent features such as the oscillations of both G peak center and FWHM present in the theoretical curves are not clearly reflected in the experimental data, the dominant feature near $B = 3.5$ T corresponding to the strongest MPR due to the $LL_{-2,1}^{-1,2}$ transition can be seen. The deviation between the theoretical and experimental data could be due to the relatively poor quality of the sample and/or the uniformly distributed nonintentional doping from the substrate.

Furthermore, we substituted these values extracted from MPR into the model for the phonon anomaly phenomenon at $B = 0$ T [116]. Following Remi's work, we use equation 5.7 to analyze the phonon anomaly phenomenon [116]. The shift and broadening of the phonon can be given by the real and imaginary part of the self-energy ($\Pi(\varepsilon_0)$).

$$\Pi(\varepsilon_0) = \eta \varepsilon_F - \frac{\eta}{4} (\varepsilon_0 + i\delta) \left(\ln \left(\frac{\varepsilon_0 + 2\varepsilon_F + i\delta}{\varepsilon_0 - 2\varepsilon_F + i\delta} \right) + i\pi \right), \quad (5.7)$$

$$\varepsilon_F = \hbar v_F \sqrt{\pi n}, \quad (5.8)$$

$$n = \frac{C |V_g - V_{Driac}|}{e} = 7.18 \times 10^{10} \frac{cm^{-2}}{V} |V_g - V_{Driac}|, \quad (5.9)$$

where, ε_0 stands for the phonon energy at $B = 0$ T. η is the interaction strength. δ stands for the broadening factor. v_F represents for the Fermi velocity. n means carrier concentration and ε_F is the Fermi level.

Substituting for values obtained from the MPR fitting (Figure 5.5) into equation (5.7) [the interaction strength $\eta = 5 \times 10^{-3}$, the broadening factor $\delta = 49.6 meV = 400 cm^{-1}$, the phonon energy at zero magnetic field $\varepsilon_0 = 1587.6 cm^{-1}$, and the Fermi velocity $v_F = 1.21 \times 10^6 m^2 / s$], the phonon energies and the FWHMs for different back gates can be calculated. As shown in the Figure 5.2d, good agreement between the simulated curves and the experimental data points is achieved.

Then we will focus on the doping effect on MPR in the monolayer graphene sample. When the sample was applied with a V_g of -6 V, its filling factor ν is around 0. In this case, only the central LL ($n = 0$) is half filled. Thus, inter- LL electronic excitations $LL_{-2,1}^{-1,2}$ are allowed and can couple to the G phonon. Both high level p -type and n -type doping, which yield big filling factor, can block the inter- LL electronic excitations thus suppress MPR effect in graphene. Note that phonon lifetime which can be reflected by the FWHM of G band phonon (see Fig. 5.5b)

increased when the LL transition is switched off. Filling factor in monolayer graphene can be calculated [4, 14, 124]:

$$\nu = \frac{n_s}{eB/h}, \quad n_s = C_g |V_g - V_{Dirac}| / e, \quad \nu = g_s (n + 1/2) \quad (5.10)$$

where ν is the filling factor and n_s is the carrier density. $g_s = 4$, accounting for the spin degeneracy and sublattice degeneracy. C_g stands for the gate capacitance and is $\sim 115 \text{ aF}\mu\text{m}^{-2}$. Based on equation (3), the filling factor in our sample is $\nu = \pm 26$ under $B = 3.5 \text{ T}$ when $V_g = 24 \text{ V}/-36 \text{ V}$, which means that the electrons will fill to the LL with index $n = \pm 6$. Schematic images for these three different doping situations ($B = 3.5 \text{ T}$) in monolayer graphene are shown in Figure 5.5(c-e). $LL_{-2,1}^{-1,2}$ transition is Pauli blocked in Fig. 5.5d (or Fig. 5.5e) because both initial and final transition states are filled (or empty). Consequently, the inter-LL excitations $LL_{-2,1}^{-1,2}$ become inactive in both cases resulting in the suppression of their hybridizations with the G phonon.

5.2.6 MPR in as prepared supported and suspended graphene

Figure 5.6a shows optical image of one representative graphene sample and monolayer region is indicated by the red arrow. Exfoliated samples were prepared on top of the commonly used SiO_2 (300 nm)/Si substrate. Magnetic field dependent evolutions of the G peak center and the FWHM for the monolayer graphene were shown in Figure 5.6b. This result is similar to the gated graphene when V_g is -6 V (as shown in Figure 5.5). The possible reason for this result is that this as-exfoliated

sample is nearly intrinsic or not highly doped at low temperature in the vacuum environment.

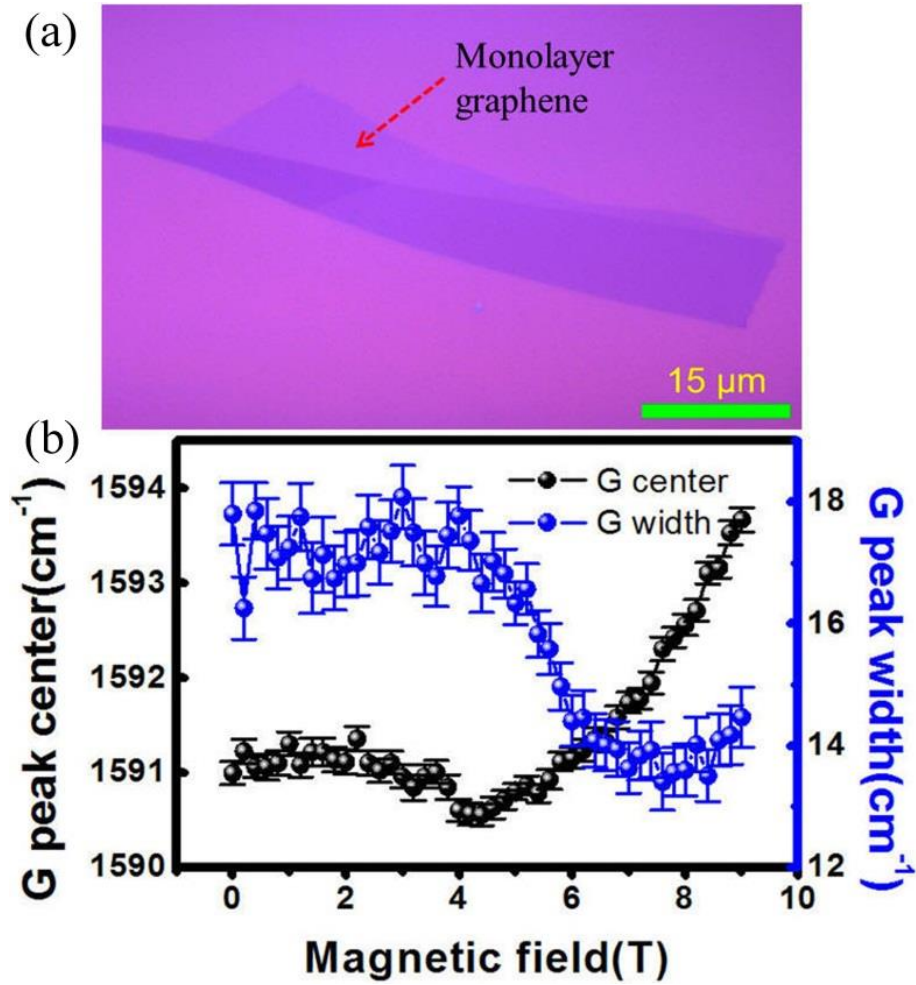


Figure 5.6. Magneto-Raman scattering in supported monolayer graphene. (a) Optical image of the as-exfoliated sample which contains monolayer graphene (indicated by the red arrow). (b) Evolutions of the G peak center and the FWHM under magnetic fields for the monolayer graphene.

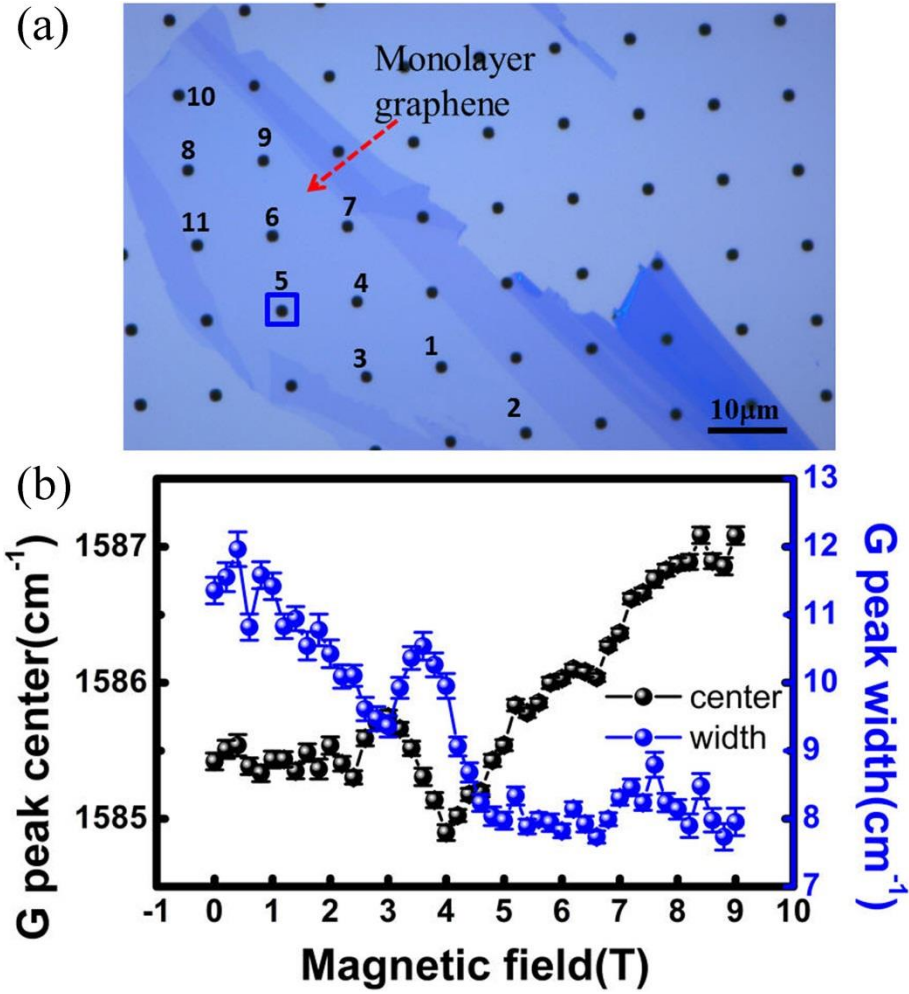


Figure 5.7. (a) Optical image of the as exfoliated sample on a substrate with patterned holes. More than 10 holes on the substrate were covered by this monolayer graphene (indicated by the red arrow, holes are numbered to state different suspended graphene areas). The diameter of a hole is about 3 μm while the laser spot size is about 1 μm . (b) G peak center (black spheres) and width (blue spheres) as a function of magnetic fields for the suspended monolayer graphene region numbered 5 (indicated by the blue square).

Figure 5.7 shows the magneto-Raman results of the G mode for a suspended monolayer graphene. There are more than ten suspended regions in this graphene sample (Figure 5.7a) and distinct magnetic field dependent variations of the frequency and the FWHM of the G peak can be observed from all randomly measured regions. The results shown in figure 5.7b are obtained from region numbered 5 and the resonant field is about 3.6 T.

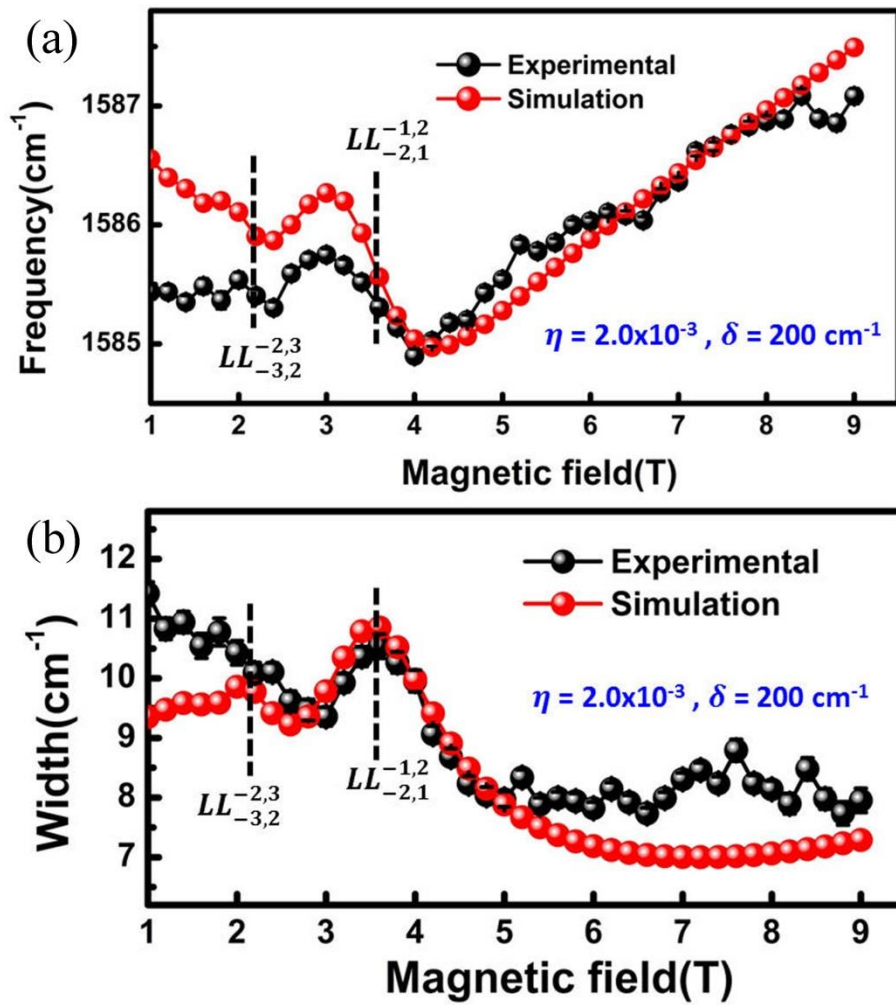


Figure 5.8. (a-b) Simulation results compared with experimental data of G peak center and the FWHM as a function of magnetic field for the exfoliated suspended monolayer graphene shown in Figure 5.7. The parameters η and δ used for the simulation are specified in figures.

Figure 5.8 presents simulation results for the suspended monolayer graphene. Extracted values are: the interaction strength $\eta = 2 \times 10^{-3}$, the broadening factor $\delta = 200 \text{ cm}^{-1} = 24.8 \text{ meV}$, the phonon energy at zero magnetic field $\varepsilon_0 = 1585 \text{ cm}^{-1}$, Fermi velocity $v_F = 1.21 \times 10^6 \text{ m}^2 / \text{s}$. Not only the main feature but also another small oscillation is presented, which corresponds to the MPR caused by another transition between LLs as illustrated.

Notice that the oscillation in the suspended sample is most obvious among studied graphene samples in this chapter. Comparing the widths of their G bands (Figure 5.5b, Figure 5.6b and Figure 5.7b), we can see that the suspended graphene sample also possesses a narrowest G band, suggesting a longest phonon lifetime. We suspect that a longer phonon lifetime in the sample represents a higher quality, which is an important factor affecting the MPR in graphene [99]. Due to the elimination of both the substrate effect and the influence of impurities caused by device fabrication, the suspended graphene can have the longest lifetime among these samples. This assumption can be further confirmed by the fact that the graphene-like region on the graphite substrate with much narrower G peak width of $\sim 4 \text{ cm}^{-1}$ shows more prominent MPR effect than other graphene samples [37, 44].

5.3 Conclusions

We have studied magneto-Raman scattering by sweeping relative low magnetic fields in mechanically exfoliated monolayer graphene under different situations: (1) transistor which is electrically tuned to fixed doping levels; (2) supported on SiO₂/Si substrate; (3) suspended from the substrate. The MPR effect involving $LL_{-2,1}^{-1,2}$ transitions appears when the filling factor is near zero while disappears when the sample is highly doped due to Pauli blocking. Filling factor effect on MPR in monolayer graphene is thus experimentally present to match well with the theoretical prediction. The suspended sample which is newly reported for MPR study shows the clearest oscillation among the studied samples in this chapter, indicating the importance of sample quality. Besides, Fano resonance is proposed to explain the observed asymmetric line shape of the Raman G band in electrically neutral graphene. Furthermore, magnetic field effect on the Fano resonance is demonstrated in our work. These findings extend our knowledge of MPR in graphene and may trigger pertinent theoretical studies in graphene and other 2D systems.

Chapter 6 Conclusions and future work

6.1 Conclusions

This thesis mainly has three parts. Firstly, electron beam writing and metal deposition effects on lattice and electronic structure of graphene have been studied. Secondly, the magneto-Raman scattering measurements on the monolayer graphene on graphite have been conducted. Thirdly, electric field tuned magneto-phonon resonance have been experimentally presented.

Part 1. Both electron beam irradiation and metal deposition effects on graphene lattice and electronic structure have been studied. The mention of defect mechanism due to the amorphous carbon deposition induced by severe electron beam irradiation is something new. The electron beam could penetrate the resist and interact with the graphene and substrate during real EBL process and thus destroy the lattice structure of graphene by knocking off carbons or enabling the reaction between graphene and substrate. After metal deposition on graphene, Ti could not introduce defects in graphene while Au remarkably damage graphene lattice. Ti could induce n-type doping while Au makes the graphene to be p-type doped. These experimental findings reveal the influence of the fabrication techniques on lattice and electronic structure of graphene.

Part 2. Ultra high quality of graphene on graphite samples have been founded through magneto-Raman mapping method. Rich magnetic field dependent Raman active features have been presented. Raman active LL transitions have been successfully assigned. MPR which is due to the interaction of the G phonon and the electronic excitations between Dirac fermion LLs has been observed. The revised two coupled mode model successfully interpret the measured main features (G_+ , G_- modes) in a range from 3 T to 7 T. The magnetic field dependent middle frequency mode (G_i) is explained by a newly proposed model. The G_i mode may come from the G-band of the graphite substrate which is coupling with the G_+ and G_- modes. These obtained results show our new understanding of a phonon-phonon coupling between the decoupled graphene layer and the graphite substrate. The extracted narrow LL width of 10.6 cm^{-1} (about 1.3 meV) verifies the high quality of the graphene on graphite sample. The specifically high quality of the graphene layer obtained implies the critical effect of the substrate on the quality of the graphene samples. Findings in this part could stimulate future efforts to achieve high quality sample for graphene and other 2D materials.

Part 3. The MPR in graphene transistor has been presented to be switched on/off by tuning the electric field. The MPR effect involving $LL_{-2,1}^{-1,2}$ transitions appears when the filling factor is near zero while disappears when the sample is highly doped due to Pauli blocking. Thus, the experimental results verify the predicted MPR phenomenon in graphene. The suspended sample which possesses a longer lifetime

shows a more obvious MPR oscillation than the graphene device, indicating the importance of sample quality. Furthermore, magnetic field effect on the Fano resonance is demonstrated. Detailed understandings for the magnetic field modification on Fano Resonance in graphene and other 2D materials could be promising future works. These findings enrich our knowledge of MPR in graphene and may trigger more research works related to both the fundamental physics and potential applications of graphene and other 2D systems.

6.2 Future work

(1) Magneto-phonon resonance in trilayer graphene

Trilayer graphene (TLG) is one of the hottest research topics because of its novel electronic properties [125-131]. TLG is experimentally observed to appear as two crystal structures of Bernal (ABA) and rhombohedral (ABC) stacking orders when the carbon atoms are arranged differently. The different relative positions of carbon atoms in each layer and subsequently the hopping energies among the interlayer atoms lead to the variety of electronic band structures of these two types of TLG, especially at low energy region. Electronic band structures of ABA and ABC stacked TLG samples have been unveiled by several techniques such as integer quantum Hall effect (IQHE) measurements [131], infrared (IR) absorption spectroscopy [132], scanning tunnelling microscopy [133], and Raman spectroscopy [91, 134].

There is no systematic experimental report of MPR in TLG yet. How photons, electrons and phonons interact with each other in TLG under a magnetic field? Will the stacking sequences affect such MPR? Thus, the MPR study in trilayer graphene could be a very meaningful future work. Experiments have been carried out on trilayer graphene by us. However, more experimental and theoretical investigations are needed. This work could pay the way for the optical probing of magneto-excitations in low dimensional materials.

(2) Optical properties of two-dimensional transitional metal dichalcogenide

Two-dimensional monolayer transitional metal dichalcogenide (*e.g.* MoS₂) shows to be direct band gap semiconductors and attracts lots of interests [24, 135-137]. From the transport measurements, we can see that they possess large on/off ratio as a field effect transistor [138-142]. The observation of trions in them due to quantum confinement extended the knowledge on trions in two dimensional materials [143-148]. Their light emission properties enable their promising applications as light emission diode [149-152]. Understanding the fundamental properties of these two-dimensional transitional metal dichalcogenide would be great help for their future potential applications.

Investigation on their photoluminescence properties under magnetic field and electric field would be promising since we can prepare both chemical vapour deposition and mechanical exfoliated monolayer tungsten disulphide [142, 153].

Tuning of the carrier concentration through back gate would expect to induce trions into the sample at low temperature similar like the cases in MoS_2 , MoSe_2 and WSe_2 [143, 145, 154]. Strong laser power can induce light induced doping in the graphene sample [155, 156]. However, the laser power effect on WS_2 needs further investigations [144]. The carrier concentration and laser power effects on the light emission properties of WS_2 are still not well understood and can be promising projects. Some preliminary works have been done in our group on this topic and further works are still needed. These studies may pave the way for the applications of two-dimensional transitional metal dichalcogenide.

References:

- [1] Geim, A. K.; Novoselov, K. S. The rise of graphene. *Nature Materials* **2007**, *6*, 183-191.
- [2] Du, X.; Skachko, I.; Barker, A.; Andrei, E. Y. Approaching ballistic transport in suspended graphene. *Nat Nano* **2008**, *3*, 491-495.
- [3] Novoselov, K. S.; Jiang, Z.; Zhang, Y.; Morozov, S. V.; Stormer, H. L.; Zeitler, U.; Maan, J. C.; Boebinger, G. S.; Kim, P.; Geim, A. K. Room-temperature quantum hall effect in graphene. *Science* **2007**, *315*, 1379-1379.
- [4] Zhang, Y. B.; Tan, Y. W.; Stormer, H. L.; Kim, P. Experimental observation of the quantum Hall effect and Berry's phase in graphene. *Nature* **2005**, *438*, 201-204.
- [5] Lee, C.; Wei, X.; Kysar, J. W.; Hone, J. Measurement of the elastic properties and intrinsic strength of monolayer graphene. *Science* **2008**, *321*, 385-388.
- [6] Nair, R. R.; Blake, P.; Grigorenko, A. N.; Novoselov, K. S.; Booth, T. J.; Stauber, T.; Peres, N. M.; Geim, A. K. Fine structure constant defines visual transparency of graphene. *Science* **2008**, *320*, 1308.
- [7] Seol, J. H.; Jo, I.; Moore, A. L.; Lindsay, L.; Aitken, Z. H.; Pettes, M. T.; Li, X.; Yao, Z.; Huang, R.; Broido, D.; Mingo, N.; Ruoff, R. S.; Shi, L. Two-dimensional phonon transport in supported graphene. *Science* **2010**, *328*, 213-216.
- [8] Bae, S.; Kim, H.; Lee, Y.; Xu, X. F.; Park, J. S.; Zheng, Y.; Balakrishnan, J.; Lei, T.; Kim, H. R.; Song, Y. I.; Kim, Y. J.; Kim, K. S.; Ozyilmaz, B.; Ahn, J. H.; Hong, B. H.; Iijima, S. Roll-to-roll production of 30-inch graphene films for transparent electrodes. *Nat Nanotechnol* **2010**, *5*, 574-578.
- [9] Li, X. S.; Zhu, Y. W.; Cai, W. W.; Borysiak, M.; Han, B. Y.; Chen, D.; Piner, R. D.; Colombo, L.; Ruoff, R. S. Transfer of Large-Area Graphene Films for High-Performance Transparent Conductive Electrodes. *Nano Lett.* **2009**, *9*, 4359-4363.
- [10] Schedin, F.; Geim, A. K.; Morozov, S. V.; Hill, E. W.; Blake, P.; Katsnelson, M. I.; Novoselov, K. S. Detection of individual gas molecules adsorbed on graphene. *Nature Materials* **2007**, *6*, 652-655.
- [11] Wu, Y.; Lin, Y. M.; Bol, A. A.; Jenkins, K. A.; Xia, F.; Farmer, D. B.; Zhu, Y.; Avouris, P. High-frequency, scaled graphene transistors on diamond-like carbon. *Nature* **2011**, *472*, 74-78.
- [12] Lin, Y. M.; Dimitrakopoulos, C.; Jenkins, K. A.; Farmer, D. B.; Chiu, H. Y.; Grill, A.; Avouris, P. 100-GHz Transistors from Wafer-Scale Epitaxial Graphene. *Science* **2010**, *327*, 662-662.
- [13] Castro Neto, A. H.; Peres, N. M. R.; Novoselov, K. S.; Geim, A. K. The electronic properties of graphene. *Rev. Mod. Phys.* **2009**, *81*, 109-162.

-
- [14] Novoselov, K. S.; Geim, A. K.; Morozov, S. V.; Jiang, D.; Katsnelson, M. I.; Grigorieva, I. V.; Dubonos, S. V.; Firsov, A. A. Two-dimensional gas of massless Dirac fermions in graphene. *Nature* **2005**, *438*, 197-200.
 - [15] Ferrari, A. C.; Meyer, J. C.; Scardaci, V.; Casiraghi, C.; Lazzeri, M.; Mauri, F.; Piscanec, S.; Jiang, D.; Novoselov, K. S.; Roth, S.; Geim, A. K. Raman Spectrum of Graphene and Graphene Layers. *Phys. Rev. Lett.* **2006**, *97*, 187401.
 - [16] Ni, Z. H.; Wang, H. M.; Kasim, J.; Fan, H. M.; Yu, T.; Wu, Y. H.; Feng, Y. P.; Shen, Z. X. Graphene Thickness Determination Using Reflection and Contrast Spectroscopy. *Nano Lett.* **2007**, *7*, 2758-2763.
 - [17] Das, A.; Pisana, S.; Chakraborty, B.; Piscanec, S.; Saha, S. K.; Waghmare, U. V.; Novoselov, K. S.; Krishnamurthy, H. R.; Geim, A. K.; Ferrari, A. C.; Sood, A. K. Monitoring dopants by Raman scattering in an electrochemically top-gated graphene transistor. *Nature nanotechnology* **2008**, *3*, 210-215.
 - [18] Yan, J.; Zhang, Y.; Kim, P.; Pinczuk, A. Electric Field Effect Tuning of Electron-Phonon Coupling in Graphene. *Phys. Rev. Lett.* **2007**, *98*, 166802.
 - [19] Dresselhaus, M. S.; Jorio, A.; Saito, R. Characterizing Graphene, Graphite, and Carbon Nanotubes by Raman Spectroscopy. *Annual Review of Condensed Matter Physics* **2010**, *1*, 89-108.
 - [20] Ni, Z.; Wang, Y.; Yu, T.; Shen, Z. Raman spectroscopy and imaging of graphene. *Nano Res.* **2010**, *1*, 273-291.
 - [21] Malard, L. M.; Pimenta, M. A.; Dresselhaus, G.; Dresselhaus, M. S. Raman spectroscopy in graphene. *Physics Reports* **2009**, *473*, 51-87.
 - [22] Lazzeri, M.; Attacalite, C.; Wirtz, L.; Mauri, F. Impact of the electron-electron correlation on phonon dispersion: Failure of LDA and GGA DFT functionals in graphene and graphite. *Phys. Rev. B* **2008**, *78*, 081406.
 - [23] Novoselov, K. S.; Geim, A. K.; Morozov, S. V.; Jiang, D.; Zhang, Y.; Dubonos, S. V.; Grigorieva, I. V.; Firsov, A. A. Electric field effect in atomically thin carbon films. *Science* **2004**, *306*, 666-669.
 - [24] Novoselov, K. S.; Jiang, D.; Schedin, F.; Booth, T. J.; Khotkevich, V. V.; Morozov, S. V.; Geim, A. K. Two-dimensional atomic crystals. *Proc. Natl. Acad. Sci. U. S. A.* **2005**, *102*, 10451-10453.
 - [25] Thomsen, C.; Reich, S. Doable resonant Raman scattering in graphite. *Phys. Rev. Lett.* **2000**, *85*, 5214-5217.
 - [26] Hashimoto, A.; Suenaga, K.; Gloter, A.; Urita, K.; Iijima, S. Direct evidence for atomic defects in graphene layers. *Nature* **2004**, *430*, 870-873.
 - [27] Teweldebrhan, D.; Balandin, A. A. Modification of graphene properties due to electron-beam irradiation. *Appl. Phys. Lett.* **2009**, *94*, 013101.
 - [28] Ni, Z. H.; Ponomarenko, L. A.; Nair, R. R.; Yang, R.; Anissimova, S.; Grigorieva, I. V.; Schedin, F.; Blake, P.; Shen, Z. X.; Hill, E. H.; Novoselov, K. S.; Geim, A. K. On Resonant Scatterers As a Factor Limiting Carrier Mobility in Graphene. *Nano Letters* **2010**, *10*, 3868-3872.
 - [29] Firsov, Y.; Gurevich, V.; Parfeniev, R.; Shalyt, S. Investigation of a New Type of Oscillations in the Magnetoresistance. *Phys. Rev. Lett.* **1964**, *12*, 660-662.
-

-
- [30] Nicholas, R. J. The magnetophonon effect. *Progress in Quantum Electronics* **1985**, *10*, 1-75.
 - [31] Tsui, D.;Englert, T.;Cho, A.; Gossard, A. Observation of Magnetophonon Resonances in a Two-Dimensional Electronic System. *Phys. Rev. Lett.* **1980**, *44*, 341-344.
 - [32] Stradling, R. A.; Wood, R. A. The magnetophonon effect in III-V semiconducting compounds. *Journal of Physics C: Solid State Physics* **1968**, *1*, 1711.
 - [33] Ando, T. Magnetic Oscillation of Optical Phonon in Graphene. *J. Phys. Soc. Jpn.* **2007**, *76*, 024712.
 - [34] Goerbig, M. O.;Fuchs, J. N.;Kchedzhi, K.; Fal'ko, V. I. Filling-Factor-Dependent Magnetophonon Resonance in Graphene. *Phys. Rev. Lett.* **2007**, *99*, 087402.
 - [35] Kashuba, O.; Fal'ko, V. I. Signature of electronic excitations in the Raman spectrum of graphene. *Phys. Rev. B* **2009**, *80*, 241404.
 - [36] Faugeras, C.;Amado, M.;Kossacki, P.;Orlita, M.;Sprinkle, M.;Berger, C.;de Heer, W.; Potemski, M. Tuning the Electron-Phonon Coupling in Multilayer Graphene with Magnetic Fields. *Phys. Rev. Lett.* **2009**, *103*, 186803.
 - [37] Yan, J.;Goler, S.;Rhône, T.;Han, M.;He, R.;Kim, P.;Pellegrini, V.; Pinczuk, A. Observation of Magnetophonon Resonance of Dirac Fermions in Graphite. *Phys. Rev. Lett.* **2010**, *105*, 227401.
 - [38] Faugeras, C.;Amado, M.;Kossacki, P.;Orlita, M.;Kühne, M.;Nicolet, A.;Latyshev, Y.; Potemski, M. Magneto-Raman Scattering of Graphene on Graphite: Electronic and Phonon Excitations. *Phys. Rev. Lett.* **2011**, *107*, 036807.
 - [39] Kossacki, P.;Faugeras, C.;Kühne, M.;Orlita, M.;Nicolet, A.;Schneider, J.;Basko, D.;Latyshev, Y.; Potemski, M. Electronic excitations and electron-phonon coupling in bulk graphite through Raman scattering in high magnetic fields. *Phys. Rev. B* **2011**, *84*, 235138.
 - [40] Li, G. H.;Luican, A.; Andrei, E. Y. Scanning Tunneling Spectroscopy of Graphene on Graphite. *Phys. Rev. Lett.* **2009**, *102*, 176804.
 - [41] Kim, Y.;Ma, Y.;Imambekov, A.;Kalugin, N.;Lombardo, A.;Ferrari, A.;Kono, J.; Smirnov, D. Magnetophonon resonance in graphite: High-field Raman measurements and electron-phonon coupling contributions. *Phys. Rev. B* **2012**, *85*, 121403.
 - [42] Huang, P. Y.;Ruiz-Vargas, C. S.;van der Zande, A. M.;Whitney, W. S.;Levendorf, M. P.;Kevek, J. W.;Garg, S.;Alden, J. S.;Hustedt, C. J.;Zhu, Y.;Park, J.;McEuen, P. L.; Muller, D. A. Grains and grain boundaries in single-layer graphene atomic patchwork quilts. *Nature* **2011**, *469*, 389-392.
 - [43] Blake, P.;Hill, E. W.;Castro Neto, A. H.;Novoselov, K. S.;Jiang, D.;Yang, R.;Booth, T. J.; Geim, A. K. Making graphene visible. *Appl. Phys. Lett.* **2007**, *91*, 063124.
 - [44] Qiu, C.;Shen, X.;Cao, B.;Cong, C.;Saito, R.;Yu, J.;Dresselhaus, M. S.; Yu, T. Strong magnetophonon resonance induced triple G-mode splitting in graphene on graphite probed by micromagneto Raman spectroscopy. *Phys. Rev. B* **2013**, *88*, 165407.
 - [45] Wu, Y. H.;Yu, T.; Shen, Z. X. Two-dimensional carbon nanostructures: Fundamental properties, synthesis, characterization, and potential applications. *Journal of Applied Physics* **2010**, *108*, 071301.
-

-
- [46] Childres, I.;Jauregui, L. A.;Foxe, M.;Tian, J.;Jalilian, R.;Jovanovic, I.; Chen, Y. P. Effect of electron-beam irradiation on graphene field effect devices. *Appl. Phys. Lett.* **2010**, 97, 173109.
 - [47] Teweldebrhan, D.; Balandin, A. A. Response to "Comment on 'Modification of graphene properties due to electron-beam irradiation' " *Appl. Phys. Lett.* 95, 246101(2009). *Appl. Phys. Lett.* **2009**, 95, 246102.
 - [48] He, Y. H.;Wang, L.;Chen, X. L.;Wu, Z. F.;Li, W.;Cai, Y.; Wang, N. Modifying electronic transport properties of graphene by electron beam irradiation. *Appl. Phys. Lett.* **2011**, 99, 033109.
 - [49] Kim, K.-j.;Choi, J.;Lee, H.;Lee, H.-K.;Kang, T.-H.;Han, Y.-H.;Lee, B.-C.;Kim, S.; Kim, B. Effects of 1 MeV Electron Beam Irradiation on Multilayer Graphene Grown on 6H-SiC(0001). *The Journal of Physical Chemistry C* **2008**, 112, 13062-13064.
 - [50] Xu, M. S.;Fujita, D.; Hanagata, N. Monitoring electron-beam irradiation effects on graphenes by temporal Auger electron spectroscopy. *Nanotechnology* **2010**, 21, 265705.
 - [51] Jones, J. D.;Mahajan, K. K.;Williams, W. H.;Ecton, P. A.;Mo, Y.; Perez, J. M. Formation of graphane and partially hydrogenated graphene by electron irradiation of adsorbates on graphene. *Carbon* **2010**, 48, 2335-2340.
 - [52] Chen, J. H.;Cullen, W. G.;Jang, C.;Fuhrer, M. S.; Williams, E. D. Defect Scattering in Graphene. *Physical Review Letters* **2009**, 102, 236805.
 - [53] Pi, K.;McCreary, K. M.;Bao, W.;Han, W.;Chiang, Y. F.;Li, Y.;Tsai, S. W.;Lau, C. N.; Kawakami, R. K. Electronic doping and scattering by transition metals on graphene. *Physical Review B* **2009**, 80, 075406.
 - [54] McCreary, K. M.;Pi, K.;Swartz, A. G.;Han, W.;Bao, W.;Lau, C. N.;Guinea, F.;Katsnelson, M. I.; Kawakami, R. K. Effect of cluster formation on graphene mobility. *Physical Review B* **2010**, 81, 115453.
 - [55] Meyer, J. C.;Kisielowski, C.;Erni, R.;Rossell, M. D.;Crommie, M. F.; Zettl, A. Direct Imaging of Lattice Atoms and Topological Defects in Graphene Membranes. *Nano Letters* **2008**, 8, 3582-3586.
 - [56] Li, L.;Reich, S.; Robertson, J. Defect energies of graphite: Density-functional calculations. *Physical Review B* **2005**, 72, 184109
 - [57] Liu, G. X.;Teweldebrhan, D.; Balandin, A. A. Tuning of Graphene Properties via Controlled Exposure to Electron Beams. *Ieee Transactions on Nanotechnology* **2011**, 10, 865-870.
 - [58] Ferrari, A. C.; Robertson, J. Interpretation of Raman spectra of disordered and amorphous carbon. *Physical Review B* **2000**, 61, 14095-14107.
 - [59] Meyer, J. C.;Girit, C. O.;Crommie, M. F.; Zettl, A. Hydrocarbon lithography on graphene membranes. *Appl. Phys. Lett.* **2008**, 92, 123110.
 - [60] H.W.Conru; P.C.Laberge Oil contamination with the SEM operated in the spot scanning mode. *J.Phys.E: Sci.Instrum* **1975**, 8, 136-138.
 - [61] Elias, D. C.;Nair, R. R.;Mohiuddin, T. M. G.;Morozov, S. V.;Blake, P.;Halsall, M. P.;Ferrari, A. C.;Boukhvalov, D. W.;Katsnelson, M. I.;Geim, A. K.; Novoselov, K. S.
-

- Control of Graphene's Properties by Reversible Hydrogenation: Evidence for Graphane. *Science* **2009**, *323*, 610-613.
- [62] Luo, Z. Q.; Yu, T.; Ni, Z. H.; Lim, S. H.; Hu, H. L.; Shang, J. Z.; Liu, L.; Shen, Z. X.; Lin, J. Y. Electronic Structures and Structural Evolution of Hydrogenated Graphene Probed by Raman Spectroscopy. *Journal of Physical Chemistry C* **2011**, *115*, 1422-1427.
- [63] Lanzillotto, A. M.; Madey, T. E.; Baragiola, R. A. Negative-ion desorption from insulators by electron excitation of core levels. *Physical Review Letters* **1991**, *67*, 232-235.
- [64] Lehtinen, O.; Kotakoski, J.; Krasheninnikov, A. V.; Tolvanen, A.; Nordlund, K.; Keinonen, J. Effects of ion bombardment on a two-dimensional target: Atomistic simulations of graphene irradiation. *Physical Review B* **2010**, *81*, 153401.
- [65] Fan, J. Y.; Michalik, J. M.; Casado, L.; Roddaro, S.; Ibarra, M. R.; De Teresa, J. M. Investigation of the influence on graphene by using electron-beam and photo-lithography. *Solid State Communications* **2011**, *151*, 1574-1578.
- [66] Ulman, K.; Narasimhan, S. Point defects in twisted bilayer graphene: A density functional theory study. *Phys. Rev. B* **2014**, *89*, 245429.
- [67] Hawryluk, R. J.; Hawryluk, A. M.; Smith, H. I. Energy dissipation in a thin polymer film by electron beam scattering. *Journal of Applied Physics* **1974**, *45*, 2551-2566.
- [68] Hawryluk, R. J.; Smith, H. I.; Soares, A.; Hawryluk, A. M. Energy dissipation in a thin polymer film by electron beam scattering: Experiment. *Journal of Applied Physics* **1975**, *46*, 2528-2537.
- [69] Asano, T.; Uetake, N.; Suzuki, K. Mean Atomic Velocities of Uranium, Titanium and Copper during Electron Beam Evaporation. *Journal of Nuclear Science and Technology* **1992**, *29*, 1194-1200.
- [70] Reichelt, K.; Jiang, X. The preparation of thin films by physical vapour deposition methods. *Thin Solid Films* **1990**, *191*, 91-126.
- [71] Giovannetti, G.; Khomyakov, P. A.; Brocks, G.; Karpan, V. M.; van den Brink, J.; Kelly, P. J. Doping graphene with metal contacts. *Physical Review Letters* **2008**, *101*, 026803.
- [72] Peimyoo, N.; Yu, T.; Shang, J.; Cong, C.; Yang, H. Thickness-dependent azobenzene doping in mono- and few-layer graphene. *Carbon* **2012**, *50*, 201-208.
- [73] Khomyakov, P. A.; Giovannetti, G.; Rusu, P. C.; Brocks, G.; van den Brink, J.; Kelly, P. J. First-principles study of the interaction and charge transfer between graphene and metals. *Physical Review B* **2009**, *79*, 195425.
- [74] Peimyoo, N.; Li, J.; Shang, J.; Shen, X.; Qiu, C.; Xie, L.; Huang, W.; Yu, T. Photocontrolled Molecular Structural Transition and Doping in Graphene. *ACS Nano* **2012**, *6*, 8878-8886.
- [75] Ooi, N.; Rairkar, A.; Adams, J. B. Density functional study of graphite bulk and surface properties. *Carbon* **2006**, *44*, 231-242.
- [76] Sque, S. J.; Jones, R.; Briddon, P. R. The transfer doping of graphite and graphene. *Physica Status Solidi a-Applications and Materials Science* **2007**, *204*, 3078-3084.
- [77] B. Michaelson, H. The work function of the elements and its periodicity *Journal of Applied Physics* **1977**, *48*, 4729-4733.

-
- [78] Cong, C. X.; Yu, T.; Ni, Z. H.; Liu, L.; Shen, Z. X.; Huang, W. Fabrication of Graphene Nanodisk Arrays Using Nanosphere Lithography. *Journal of Physical Chemistry C* **2009**, *113*, 6529-6532.
- [79] Wang, Y. Y.; Ni, Z. H.; Hu, H. L.; Hao, Y. F.; Wong, C. P.; Yu, T.; Thong, J. T. L.; Shen, Z. X. Gold on graphene as a substrate for surface enhanced Raman scattering study. *Appl. Phys. Lett.* **2010**, *97*, 163111.
- [80] Zhou, H. Q.; Qiu, C. Y.; Liu, Z.; Yang, H. C.; Hu, L. J.; Liu, J.; Yang, H. F.; Gu, C. Z.; Sun, L. F. Thickness-Dependent Morphologies of Gold on N-Layer Graphenes. *Journal of the American Chemical Society* **2010**, *132*, 944-946.
- [81] Cancado, L. G.; Takai, K.; Enoki, T.; Endo, M.; Kim, Y. A.; Mizusaki, H.; Jorio, A.; Coelho, L. N.; Magalhaes-Paniago, R.; Pimenta, M. A. General equation for the determination of the crystallite size L_a of nanographite by Raman spectroscopy. *Appl. Phys. Lett.* **2006**, *88*, 163106.
- [82] Huang, B. C.; Zhang, M.; Wang, Y. J.; Woo, J. Contact resistance in top-gated graphene field-effect transistors. *Appl. Phys. Lett.* **2011**, *99*, 032107.
- [83] Jiang, Z.; Henriksen, E. A.; Tung, L. C.; Wang, Y. J.; Schwartz, M. E.; Han, M. Y.; Kim, P.; Stormer, H. L. Infrared Spectroscopy of Landau Levels of Graphene. *Phys. Rev. Lett.* **2007**, *98*, 197403.
- [84] Orlita, M.; Faugeras, C.; Plochocka, P.; Neugebauer, P.; Martinez, G.; Maude, D. K.; Barra, A. L.; Sprinkle, M.; Berger, C.; de Heer, W. A.; Potemski, M. Approaching the Dirac Point in High-Mobility Multilayer Epitaxial Graphene. *Phys. Rev. Lett.* **2008**, *101*, 267601.
- [85] Andrei, E. Y.; Li, G. H.; Du, X. Electronic properties of graphene: a perspective from scanning tunneling microscopy and magnetotransport. *Rep. Prog. Phys.* **2012**, *75*, 056501.
- [86] Miller, D. L.; Kubista, K. D.; Rutter, G. M.; Ruan, M.; de Heer, W. A.; First, P. N.; Strosio, J. A. Observing the Quantization of Zero Mass Carriers in Graphene. *Science* **2009**, *324*, 924-927.
- [87] Neugebauer, P.; Orlita, M.; Faugeras, C.; Barra, A. L.; Potemski, M. How Perfect Can Graphene Be? *Phys. Rev. Lett.* **2009**, *103*, 136403.
- [88] Sato, K.; Saito, R.; Cong, C.; Yu, T.; Dresselhaus, M. S. Zone folding effect in Raman G-band intensity of twisted bilayer graphene. *Phys. Rev. B* **2012**, *86*, 125414.
- [89] Charlier, J. C.; Michenaud, J. P.; Lambin, P. Tight-binding density of electronic states of pregraphitic carbon. *Phys. Rev. B* **1992**, *46*, 4540-4543.
- [90] Lopes dos Santos, J. M. B.; Peres, N. M. R.; Castro Neto, A. H. Graphene Bilayer with a Twist: Electronic Structure. *Phys. Rev. Lett.* **2007**, *99*, 256802.
- [91] Cong, C.; Yu, T.; Sato, K.; Shang, J.; Saito, R.; Dresselhaus, G. F.; Dresselhaus, M. S. Raman Characterization of ABA- and ABC-Stacked Trilayer Graphene. *ACS Nano* **2011**, *5*, 8760-8768.
- [92] Saito, R.; Hofmann, M.; Dresselhaus, G.; Jorio, A.; Dresselhaus, M. S. Raman spectroscopy of graphene and carbon nanotubes. *Advances in Physics* **2011**, *60*, 413-550.
-

-
- [93] Dresselhaus, M. S.;Jorio, A.;Hofmann, M.;Dresselhaus, G.; Saito, R. Perspectives on Carbon Nanotubes and Graphene Raman Spectroscopy. *Nano Lett.* **2010**, *10*, 751-758.
- [94] Yu, T.;Shen, Z. X.;Shi, Y.; Ding, J. Cation migration and magnetic-ordering in spinel CoFe₂O₄ powder: micro-Raman scattering study. *J. Phys.-Condes. Matter* **2002**, *14*, L613-L618.
- [95] Dong, X.;Fu, D.;Fang, W.;Shi, Y.;Chen, P.; Li, L.-J. Doping Single-Layer Graphene with Aromatic Molecules. *Small* **2009**, *5*, 1422-1426.
- [96] Luo, Z.;Yu, T.;Ni, Z.;Lim, S.;Hu, H.;Shang, J.;Liu, L.;Shen, Z.; Lin, J. Electronic Structures and Structural Evolution of Hydrogenated Graphene Probed by Raman Spectroscopy. *The Journal of Physical Chemistry C* **2011**, *115*, 1422-1427.
- [97] Ni, Z. H.;Yu, T.;Lu, Y. H.;Wang, Y. Y.;Feng, Y. P.; Shen, Z. X. Uniaxial Strain on Graphene: Raman Spectroscopy Study and Band-Gap Opening. *ACS Nano* **2008**, *2*, 2301-2305.
- [98] Yoon, D.;Moon, H.;Son, Y.-W.;Choi, J. S.;Park, B. H.;Cha, Y. H.;Kim, Y. D.; Cheong, H. Interference effect on Raman spectrum of graphene on SiO₂/Si. *Phys. Rev. B* **2009**, *80*, 125422.
- [99] Goler, S.;Yan, J.;Pellegrini, V.; Pinczuk, A. Raman spectroscopy of magneto-phonon resonances in graphene and graphite. *Solid State Communications* **2012**, *152*, 1289-1293.
- [100] Biedermann, L. B.;Bolen, M. L.;Capano, M. A.;Zemlyanov, D.; Reifenberger, R. G. Insights into few-layer epitaxial graphene growth on 4H-SiC(0001) substrates from STM studies. *Phys. Rev. B* **2009**, *79*, 125411.
- [101] Harrison, S. E.;Capano, M. A.; Reifenberger, R. Scanning tunneling microscope study of striated carbon ridges in few-layer epitaxial graphene formed on 4H-silicon carbide (0001). *Appl. Phys. Lett.* **2010**, *96*, 081905.
- [102] Garcia, R.;Magerle, R.; Perez, R. Nanoscale compositional mapping with gentle forces. *Nat Mater* **2007**, *6*, 405-411.
- [103] Barnes, D. J.;Nicholas, R. J.;Peeters, F. M.;Wu, X. G.;Devreese, J. T.;Singleton, J.;Langerak, C. J. G. M.;Harris, J. J.; Foxon, C. T. Observation of optically detected magnetophonon resonance. *Phys. Rev. Lett.* **1991**, *66*, 794-797.
- [104] Vaughan, T. A.;Nicholas, R. J.;Langerak, C. J. G. M.;Murdin, B. N.;Pidgeon, C. R.;Mason, N. J.; Walker, P. J. Direct observation of magnetophonon resonances in Landau-level lifetimes of a semiconductor heterostructure. *Phys. Rev. B* **1996**, *53*, 16481-16484.
- [105] Kossacki, P.;Faugeras, C.;Kühne, M.;Orlita, M.;Mahmood, A.;Dujardin, E.;Nair, R. R.;Geim, A. K.; Potemski, M. Circular dichroism of magnetophonon resonance in doped graphene. *Phys. Rev. B* **2012**, *86*, 205431.
- [106] Kim, Y.;Poumirol, J. M.;Lombardo, A.;Kalugin, N. G.;Georgiou, T.;Kim, Y. J.;Novoselov, K. S.;Ferrari, A. C.;Kono, J.;Kashuba, O.;Fal'ko, V. I.; Smirnov, D. Measurement of Filling-Factor-Dependent Magnetophonon Resonances in Graphene Using Raman Spectroscopy. *Phys. Rev. Lett.* **2013**, *110*, 227402.
-

-
- [107] Leszczynski, P.; Han, Z.; Nicolet, A. A. L.; Piot, B. A.; Kossacki, P.; Orlita, M.; Bouchiat, V.; Basko, D. M.; Potemski, M.; Faugeras, C. Electrical Switch to the Resonant Magneto-Phonon Effect in Graphene. *Nano Lett.* **2014**, *14*, 1460-1466.
 - [108] Luo, Z.; Yu, T.; Kim, K.-j.; Ni, Z.; You, Y.; Lim, S.; Shen, Z.; Wang, S.; Lin, J. Thickness-Dependent Reversible Hydrogenation of Graphene Layers. *ACS Nano* **2009**, *3*, 1781-1788.
 - [109] Yu, T.; Ni, Z.; Du, C.; You, Y.; Wang, Y.; Shen, Z. Raman Mapping Investigation of Graphene on Transparent Flexible Substrate: The Strain Effect. *The Journal of Physical Chemistry C* **2008**, *112*, 12602-12605.
 - [110] Cong, C.; Yu, T.; Saito, R.; Dresselhaus, G. F.; Dresselhaus, M. S. Second-Order Overtone and Combination Raman Modes of Graphene Layers in the Range of 1690–2150 cm⁻¹. *ACS Nano* **2011**, *5*, 1600-1605.
 - [111] Cong, C.; Yu, T.; Wang, H. Raman Study on the G Mode of Graphene for Determination of Edge Orientation. *ACS Nano* **2010**, *4*, 3175-3180.
 - [112] Kuhne, M.; Faugeras, C.; Kossacki, P.; Nicolet, A. A. L.; Orlita, M.; Latyshev, Y. I.; Potemski, M. Polarization-resolved magneto-Raman scattering of graphenelike domains on natural graphite. *Phys. Rev. B* **2012**, *85*, 195406.
 - [113] Faugeras, C.; Kossacki, P.; Nicolet, A. A. L.; Orlita, M.; Potemski, M.; Mahmood, A.; Basko, D. M. Probing the band structure of quadri-layer graphene with magneto-phonon resonance. *New J. Phys.* **2012**, *14*, 095007.
 - [114] Shen, X.; Wang, H.; Yu, T. How do the electron beam writing and metal deposition affect the properties of graphene during device fabrication? *Nanoscale* **2013**, *5*, 3352-3358.
 - [115] Das Sarma, S.; Adam, S.; Hwang, E.; Rossi, E. Electronic transport in two-dimensional graphene. *Rev. Mod. Phys.* **2011**, *83*, 407-470.
 - [116] Rémi, S.; Goldberg, B. B.; Swan, A. K. Charge Tuning of Nonresonant Magnetoexciton Phonon Interactions in Graphene. *Phys. Rev. Lett.* **2014**, *112*, 056803.
 - [117] Yoon, D.; Jeong, D.; Lee, H.-J.; Saito, R.; Son, Y.-W.; Lee, H. C.; Cheong, H. Fano resonance in Raman scattering of graphene. *Carbon* **2013**, *61*, 373-378.
 - [118] Tan, P. H.; Han, W. P.; Zhao, W. J.; Wu, Z. H.; Chang, K.; Wang, H.; Wang, Y. F.; Bonini, N.; Marzari, N.; Pugno, N.; Savini, G.; Lombardo, A.; Ferrari, A. C. The shear mode of multilayer graphene. *Nat Mater* **2012**, *11*, 294-300.
 - [119] Oberli, D. Y.; Böhm, G.; Weimann, G.; Brum, J. A. Fano resonances in the excitation spectra of semiconductor quantum wells. *Phys. Rev. B* **1994**, *49*, 5757-5760.
 - [120] Bellani, V.; Pérez, E.; Zimmermann, S.; Viña, L.; Hey, R.; Ploog, K. Evolution of Fano resonances in two- and three-dimensional semiconductors with a magnetic field. *Solid State Communications* **1996**, *97*, 459-464.
 - [121] Jung, S.; Rutter, G. M.; Klimov, N. N.; Newell, D. B.; Calizo, I.; Hight-Walker, A. R.; Zhitenev, N. B.; Strosio, J. A. Evolution of microscopic localization in graphene in a magnetic field from scattering resonances to quantum dots. *Nat Phys* **2011**, *7*, 245-251.
 - [122] Elias, D. C.; Gorbachev, R. V.; Mayorov, A. S.; Morozov, S. V.; Zhukov, A. A.; Blake, P.; Ponomarenko, L. A.; Grigorieva, I. V.; Novoselov, K. S.; Guinea, F.; Geim, A. K. Dirac
-

- cones reshaped by interaction effects in suspended graphene. *Nat Phys* **2011**, *7*, 701-704.
- [123] Hwang, C.;Siegel, D. A.;Mo, S.-K.;Regan, W.;Ismach, A.;Zhang, Y.;Zettl, A.; Lanzara, A. Fermi velocity engineering in graphene by substrate modification. *Sci. Rep.* **2012**, *2*, 590.
- [124] von Klitzing, K. The quantized Hall effect. *Rev. Mod. Phys.* **1986**, *58*, 519-531.
- [125] Craciun, M. F.;RussoS;YamamotoM;Oostinga, J. B.;Morpurgo, A. F.; TaruchaS Trilayer graphene is a semimetal with a gate-tunable band overlap. *Nat Nano* **2009**, *4*, 383-388.
- [126] Bao, W.;Jing, L.;Velasco, J.;Lee, Y.;Liu, G.;Tran, D.;Standley, B.;Aykol, M.;Cronin, S. B.;Smirnov, D.;Koshino, M.;McCann, E.;Bockrath, M.; Lau, C. N. Stacking-dependent band gap and quantum transport in trilayer graphene. *Nat Phys* **2011**, *7*, 948-952.
- [127] Zhang, L.;Zhang, Y.;Camacho, J.;Khodas, M.; Zaliznyak, I. The experimental observation of quantum Hall effect of $l=3$ chiral quasiparticles in trilayer graphene. *Nat Phys* **2011**, *7*, 953-957.
- [128] Avetisyan, A. A.;Partoens, B.; Peeters, F. M. Stacking order dependent electric field tuning of the band gap in graphene multilayers. *Phys. Rev. B* **2010**, *81*, 115432.
- [129] Koshino, M.; McCann, E. Gate-induced interlayer asymmetry in ABA-stacked trilayer graphene. *Phys. Rev. B* **2009**, *79*, 125443.
- [130] Zhang, F.;Sahu, B.;Min, H.; MacDonald, A. H. Band structure of ABC-stacked graphene trilayers. *Phys. Rev. B* **2010**, *82*, 035409.
- [131] Kumar, A.;Escoffier, W.;Poumirol, J. M.;Faugeras, C.;Arovas, D. P.;Fogler, M. M.;Guinea, F.;Roche, S.;Goiran, M.; Raquet, B. Integer Quantum Hall Effect in Trilayer Graphene. *Phys. Rev. Lett.* **2011**, *107*, 126806.
- [132] Lui, C. H.;Li, Z.;Mak, K. F.;Cappelluti, E.; Heinz, T. F. Observation of an electrically tunable band gap in trilayer graphene. *Nat Phys* **2011**, *7*, 944-947.
- [133] Hattendorf, S.;Georgi, A.;Liebmann, M.; Morgenstern, M. Networks of ABA and ABC stacked graphene on mica observed by scanning tunneling microscopy. *Surface Science* **2013**, *610*, 53-58.
- [134] Lui, C. H.;Li, Z.;Chen, Z.;Klimov, P. V.;Brus, L. E.; Heinz, T. F. Imaging Stacking Order in Few-Layer Graphene. *Nano Lett.* **2010**, *11*, 164-169.
- [135] Wang, Q. H.;Kalantar-Zadeh, K.;Kis, A.;Coleman, J. N.; Strano, M. S. Electronics and optoelectronics of two-dimensional transition metal dichalcogenides. *Nat Nano* **2012**, *7*, 699-712.
- [136] Mak, K. F.;Lee, C.;Hone, J.;Shan, J.; Heinz, T. F. Atomically Thin MoS_2 : A New Direct-Gap Semiconductor. *Physical Review Letters* **2010**, *105*, 136805.
- [137] Splendiani, A.;Sun, L.;Zhang, Y.;Li, T.;Kim, J.;Chim, C.-Y.;Galli, G.; Wang, F. Emerging Photoluminescence in Monolayer MoS_2 . *Nano Lett* **2010**, *10*, 1271-1275.
- [138] Neal, A. T.;Liu, H.;Gu, J.; Ye, P. D. Magneto-transport in MoS_2 : Phase Coherence, Spin–Orbit Scattering, and the Hall Factor. *ACS Nano* **2013**, *7*, 7077-7082.
- [139] Radisavljevic, B.; Kis, A. Mobility engineering and a metal–insulator transition in monolayer MoS_2 . *Nat Mater* **2013**, *12*, 815-820.

-
- [140] RadisavljevicB;RadenovicA;BrivioJ;GiacomettiV; KisA Single-layer MoS₂ transistors. *Nat Nano* **2011**, 6, 147-150.
 - [141] Braga, D.;Gutiérrez Lezama, I.;Berger, H.; Morpurgo, A. F. Quantitative Determination of the Band Gap of WS₂ with Ambipolar Ionic Liquid-Gated Transistors. *Nano Lett* **2012**, 12, 5218-5223.
 - [142] Peimyoo, N.;Shang, J.;Cong, C.;Shen, X.;Wu, X.;Yeow, E. K. L.; Yu, T. Nonblinking, Intense Two-Dimensional Light Emitter: Monolayer WS₂ Triangles. *ACS Nano* **2013**, 7, 10985-10994.
 - [143] Mak, K. F.;He, K.;Lee, C.;Lee, G. H.;Hone, J.;Heinz, T. F.; Shan, J. Tightly bound trions in monolayer MoS₂. *Nat Mater* **2013**, 12, 207-211.
 - [144] Mitioğlu, A. A.;Plochocka, P.;Jadczak, J. N.;Escoffier, W.;Rikken, G. L. J. A.;Kulyuk, L.; Maude, D. K. Optical manipulation of the exciton charge state in single-layer tungsten disulfide. *Physical Review B* **2013**, 88, 245403.
 - [145] Ross, J. S.;Wu, S.;Yu, H.;Ghimire, N. J.;Jones, A. M.;Aivazian, G.;Yan, J.;Mandrus, D. G.;Xiao, D.;Yao, W.; Xu, X. Electrical control of neutral and charged excitons in a monolayer semiconductor. *Nat Commun* **2013**, 4, 1474.
 - [146] Mak, K. F.;He, K.;Shan, J.; Heinz, T. F. Control of valley polarization in monolayer MoS₂ by optical helicity. *Nat Nano* **2012**, 7, 494-498.
 - [147] Wu, S.;Ross, J. S.;Liu, G.-B.;Aivazian, G.;Jones, A.;Fei, Z.;Zhu, W.;Xiao, D.;Yao, W.;Cobden, D.; Xu, X. Electrical tuning of valley magnetic moment through symmetry control in bilayer MoS₂. *Nat Phys* **2013**, 9, 149-153.
 - [148] Zeng, H.;Dai, J.;Yao, W.;Xiao, D.; Cui, X. Valley polarization in MoS₂ monolayers by optical pumping. *Nat Nano* **2012**, 7, 490-493.
 - [149] Baugher, B. W. H.;Churchill, H. O. H.;Yang, Y.; Jarillo-Herrero, P. Optoelectronic devices based on electrically tunable p-n diodes in a monolayer dichalcogenide. *Nat Nano* **2014**, 9, 262-267.
 - [150] Bratschitsch, R. Optoelectronic devices: Monolayer diodes light up. *Nat Nano* **2014**, 9, 247-248.
 - [151] Pospischil, A.;Furchi, M. M.; Mueller, T. Solar-energy conversion and light emission in an atomic monolayer p-n diode. *Nat Nano* **2014**, 9, 257-261.
 - [152] Ross, J. S.;Klement, P.;Jones, A. M.;Ghimire, N. J.;Yan, J.;Mandrus, D. G.;Taniguchi, T.;Watanabe, K.;Kitamura, K.;Yao, W.;Cobden, D. H.; Xu, X. Electrically tunable excitonic light-emitting diodes based on monolayer WSe₂ p-n junctions. *Nat Nano* **2014**, 9, 268-272.
 - [153] Cong, C.;Shang, J.;Wu, X.;Cao, B.;Peimyoo, N.;Qiu, C.;Sun, L.; Yu, T. Synthesis and Optical Properties of Large-Area Single-Crystalline 2D Semiconductor WS₂ Monolayer from Chemical Vapor Deposition. *Advanced Optical Materials* **2014**, 2, 131-136.
 - [154] Jones, A. M.;Yu, H.;Ghimire, N. J.;Wu, S.;Aivazian, G.;Ross, J. S.;Zhao, B.;Yan, J.;Mandrus, D. G.;Xiao, D.;Yao, W.; Xu, X. Optical generation of excitonic valley coherence in monolayer WSe₂. *Nat Nano* **2013**, 8, 634-638.
 - [155] JuL;Velasco Jr, J.;HuangE;KahnS;NosigliaC;Tsai, H.-Z.;YangW;TaniguchiT;WatanabeK;ZhangY;ZhangG;CrommieM;ZettlA; WangF
-

- Photoinduced doping in heterostructures of graphene and boron nitride. *Nat Nano* **2014**, 9, 348-352.
- [156] Kim, Y. D.; Bae, M.-H.; Seo, J.-T.; Kim, Y. S.; Kim, H.; Lee, J. H.; Ahn, J. R.; Lee, S. W.; Chun, S.-H.; Park, Y. D. Focused-Laser-Enabled p–n Junctions in Graphene Field-Effect Transistors. *ACS Nano* **2013**, 7, 5850-5857.